



HAL
open science

The brittle-to-viscous transition in polycrystalline quartz: An experimental study

Bettina Richter, Holger Stünitz, Renée Heilbronner

► To cite this version:

Bettina Richter, Holger Stünitz, Renée Heilbronner. The brittle-to-viscous transition in polycrystalline quartz: An experimental study. *Journal of Structural Geology*, 2018, 114, pp.1-21. 10.1016/j.jsg.2018.06.005 . insu-01817648

HAL Id: insu-01817648

<https://insu.hal.science/insu-01817648v1>

Submitted on 18 Jun 2018

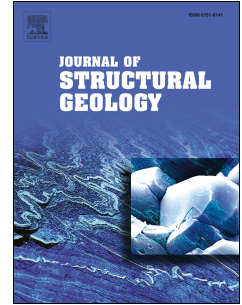
HAL is a multi-disciplinary open access archive for the deposit and dissemination of scientific research documents, whether they are published or not. The documents may come from teaching and research institutions in France or abroad, or from public or private research centers.

L'archive ouverte pluridisciplinaire **HAL**, est destinée au dépôt et à la diffusion de documents scientifiques de niveau recherche, publiés ou non, émanant des établissements d'enseignement et de recherche français ou étrangers, des laboratoires publics ou privés.

Accepted Manuscript

The brittle-to-viscous transition in polycrystalline quartz: An experimental study

Bettina Richter, Holger Stünitz, Renée Heilbronner



PII: S0191-8141(18)30275-X

DOI: [10.1016/j.jsg.2018.06.005](https://doi.org/10.1016/j.jsg.2018.06.005)

Reference: SG 3676

To appear in: *Journal of Structural Geology*

Received Date: 29 September 2017

Revised Date: 3 June 2018

Accepted Date: 3 June 2018

Please cite this article as: Richter, B., Stünitz, H., Heilbronner, René., The brittle-to-viscous transition in polycrystalline quartz: An experimental study, *Journal of Structural Geology* (2018), doi: 10.1016/j.jsg.2018.06.005.

This is a PDF file of an unedited manuscript that has been accepted for publication. As a service to our customers we are providing this early version of the manuscript. The manuscript will undergo copyediting, typesetting, and review of the resulting proof before it is published in its final form. Please note that during the production process errors may be discovered which could affect the content, and all legal disclaimers that apply to the journal pertain.

1 The brittle-to-viscous transition in polycrystalline quartz: an experimental study.

2 Bettina Richter¹, Holger Stünitz^{2,3}, Renée Heilbronner^{1,2}

3 ¹*Geological Institute, Basel University, Bernoullistrasse 32, 4055 Basel, Switzerland*

4 ²*Department of Geology, Tromsø University, Dramsveien 201, 9037 Tromsø, Norway*

5 ³*Institut des Sciences de la Terre d'Orléans (ISTO), Université d'Orléans, 45071*
6 *Orléans, France*

7 Corresponding author: Renée Heilbronner (renee.heilbronner@unibas.ch)

8

9

10 Keywords (4-6):

11 brittle-to-viscous transition, grain size distribution, dislocation creep, quartz rheology,

12 stress exponent

13

14 Abstract (<250 words)

15 Shear experiments on quartz gouge were performed at elevated confining pressures

16 (predominantly 1.5 GPa) and temperatures (500 °C - 1000 °C) at shear strain rates of

17 $3.5 \cdot 10^{-6} \text{ s}^{-1}$ to $2 \cdot 10^{-3} \text{ s}^{-1}$ to study the brittle-to-viscous transition. An unsystematic

18 temperature dependence of strength at low temperatures changes towards a clear

19 temperature weakening dependence above 650 °C. The transition from a pressure

20 strengthening to a pressure weakening relationship takes place continuously between

21 650 °C and 800 °C. Strain rate stepping experiments reveal power-law breakdown at

22 low temperatures (~650 °C). Between 800 °C and 1000 °C, a stress exponent of $n =$

23 1.9 ± 0.6 and an activation energy of $Q = 170 \pm 72 \text{ kJ/mol}$ indicate a combination of

24 diffusion and dislocation creep. The Goetze criterion is confirmed as the upper stress

25 limit for viscous deformation mechanisms. Localised deformation in the form of

26 semibrittle shear bands with Riedel geometry at low temperatures changes to
27 homogeneous deformation with a pervasive foliation accompanied by a continuous
28 texture evolution between 700 °C and 1000 °C. Fracturing dominates at low
29 temperatures accompanied by increasing amounts of dissolution and precipitation in
30 fine-grained zones with increasing temperature. Above 650 °C, dislocation and
31 diffusion creep are the dominating deformation processes, with dislocation creep
32 being favoured in larger grains while dissolution-precipitation is active in the fine-
33 grained fraction.

34

35 1. Introduction

36 The transition from fully brittle to fully viscous deformation in rocks (semi-
37 brittle field) occurs over a broad range of conditions in pressure, temperature, strain
38 rate, and H₂O-content with several changes in deformation mechanisms (e.g.,
39 *Kohlstedt et al.*, 1995; *Scholz*, 2007; *Hirth and Tullis*, 1994). Viscous denotes
40 temperature- and strain-rate dependent deformation here. In the lithosphere, the
41 transition commonly takes place within the middle crust (continents) (e.g., *Brace and*
42 *Kohlstedt*, 1980; *Handy*, 1989; *Sibson*, 1989) but it may extend into the upper mantle
43 for some rocks, e.g., below the oceanic crust (e.g., *Kohlstedt et al.*, 1995). The
44 transition region coincides with the greatest strength of rocks, and many large
45 earthquakes nucleate in this region (e.g., *Sibson*, 1989; *Scholz*, 2007).

46 Under conditions of brittle deformation (e.g., low temperatures, high strain
47 rates, typically shallow crustal levels), the strength of rocks primarily depends on
48 normal stress and pore pressure (*Byerlee*, 1978). Fracture strength and/or friction
49 control the rock deformation, leading to cataclastic processes (e.g., fracturing,
50 frictional sliding) with characteristic microstructures at greater strain. The intersection

51 of Byerlee's law (Byerlee, 1978) with the Mohr-Coulomb fracture criterion marks the
52 onset of semi-brittle deformation in most lithologies (e.g., Kohlstedt et al., 1995). This
53 intersection is termed “brittle-ductile transition” and is temperature independent.
54 Viscous deformation at higher temperature, typically at deeper crustal levels, depends
55 on strain rates and temperatures, and is caused by diffusion and/or dislocation creep
56 involving recovery processes like dynamic recrystallisation (e.g., Poirier and
57 Guillope, 1979; Tullis and Yund, 1977; Yund and Tullis, 1991; Hirth and Tullis, 1994;
58 Tullis, 2002). The transition from semibrittle to viscous deformation is marked by the
59 brittle-to-viscous-transition (Kohlstedt et al., 1995) (BVT). The Goetze criterion has
60 been introduced as an ad hoc approximation by Kohlstedt et al. (1995) to delineate
61 this transition. It is formulated as $\Delta\sigma = P_c$, i.e. the differential stress to drive viscous
62 flow is equal to the confining pressure.

63 In the transitional semi-brittle zone, stresses required to create new fractures
64 are lower than those for sliding on pre-existing faults (e.g., Byerlee, 1968; Kohlstedt et
65 al., 1995) causing pervasive fracturing and grain-size reduction (cataclasis).
66 Dislocations may be generated by cracking and healing processes (e.g., FitzGerald et
67 al., 1991; Tarantola et al., 2012; Trepmann and Stöckhert, 2013; Stünitz et al., 2017),
68 but whether these dislocations become important for crystal plasticity (dislocation
69 creep) depends on temperature and the efficiency of the recovery processes. At low
70 temperatures, tangling dislocations and high dislocation densities produce strain
71 hardening and greater stresses (e.g., Barber et al., 2010). Dominant crystal plasticity
72 is achieved at higher temperatures, where dislocation climb and recrystallisation are
73 rate controlling. For quartz, three types of dislocation creep regimes have been
74 identified dependent on the dominance of subgrain-rotation recrystallization or grain-
75 boundary migration (Hirth and Tullis, 1992).

76 Grain size reduction by cracking may play an important role for the onset of
77 viscous deformation by increasing the surface area and decreasing the transport
78 distances, leading to accelerated mass-transfer processes (e.g., *Pec et al.*, 2012;
79 *Trepmann and Stöckhert*, 2003; *Menegon et al.*, 2008; *Van Daalen et al.*, 1999). As a
80 result, deformation by diffusion creep may become the dominant mechanism should
81 such cracking occur (e.g., *Paterson*, 2013, p. 91-105, and references therein).

82 It emerges from this brief discussion that in the transition region of brittle-to-
83 viscous deformation, several processes are competing: cracking and frictional sliding,
84 crystal-plastic deformation, and diffusive mass transfer combined with friction-less
85 grain-boundary sliding. This study will try to address their relative importance for
86 deformation in quartz over a range of temperatures and confining pressures.

87 Quartz as one of the most abundant silicates in the Earth's crust is often used
88 to model and predict the mechanical behaviour of the upper lithosphere (e.g., *Brace*
89 *and Kohlstedt*, 1980). In addition, deformation mechanisms in quartz can be studied
90 independently of chemical effects because of its simple chemistry and very limited
91 compositional variation. Laboratory conditions (e.g., high strain rates: 10^{-3} - 10^{-7} s⁻¹,
92 high temperatures) have been extrapolated to natural conditions (e.g., low strain rates:
93 10^{-10} - 10^{-14} s⁻¹, low temperatures) via flow laws that are applicable for viscous
94 deformation (e.g., *Jaoul et al.*, 1984; *Kronenberg and Tullis*, 1984; *Paterson and*
95 *Luan*, 1990; *Luan and Paterson*, 1992; *Gleason and Tullis*, 1995; *Hirth et al.*, 2001;
96 *Rutter and Brody*, 2004a,b). However, few data exist to define the lower temperature
97 limit of the applicability of these flow laws. Furthermore, discrepancies exist for the
98 parameters of flow laws, so that the uncertainty for the users as to which data to use is
99 large, calling for a better characterisation of rheological properties of quartz.

100 We present a series of deformation experiments on quartz in a modified Griggs

101 apparatus to study the rheological transition from brittle-to-viscous deformation
102 mechanisms at elevated pressures and temperatures. The goal is to determine the part
103 of the pressure-temperature-strain rate-range of the transition accessible in the
104 laboratory and to extrapolate it to natural conditions. Some rheological parameters
105 determined for quartz fault-rock material in this study can be used in flow laws for
106 quartz. The extrapolation of the conditions of the brittle-to-viscous transition to
107 natural fault zones will be discussed, together with some applications of the newly
108 determined parameters for the flow law.

109

110 2. Methods

111

112 2.1 Experimental method

113 The experiments were carried out on a crushed quartz crystal from a
114 hydrothermally grown single crystal from an Alpine cleft (Aar Massif, Switzerland).
115 Pieces of the crystal were repeatedly crushed and sieved to obtain a grain-size fraction
116 below 100 μm , used for what will be considered the standard experiments (referred to
117 as ‘crushed’). One sample had a grain size range of 7-11 μm (referred to as ‘sieved’).
118 The single crystal contained several fluid inclusions (5-200 μm) (*Tarantola et al.*,
119 2010). The quartz material itself was dry with a water content close to the detection
120 limit of FTIR measurements (*Stünitz et al.*, 2017). Most inclusions, especially the
121 larger ones, cracked during the crushing procedure. The crushed material is used to
122 represent a fault gouge. However, during the time at experimental pressure and high
123 temperature, before deformation commenced, the crushed material was effectively hot
124 pressed to a dense coherent crystalline material better termed “cataclasite”.

125 **Insert Figure 1 here**

126 The crushed material (0.1 g) with 0.2 wt% water added was introduced
127 between alumina (Al_2O_3) forcing blocks (diameter 6.35 mm), cut at 45° (to achieve
128 maximum shear stress), resulting in a layer of ~ 1 mm thickness (Fig. 1). The assembly
129 was weld-sealed in a platinum jacket with a nickel foil insert. Sodium chloride was
130 used as confining medium in a Griggs-type solid-medium deformation apparatus (Fig.
131 1). The temperature was controlled by S-type (Pt/Pt-Rh) thermocouples at $T > 800^\circ\text{C}$
132 and by K-type (Cr-Al) thermocouples at $T \leq 800^\circ\text{C}$. More details on the sample
133 assembly can be found in *Pec* (2014). Samples were pressurised to confining pressure
134 while the temperature was increased in 100°C steps (at a rate of 20°C per minute) to
135 experimental conditions. The deformation experiments were started by applying a
136 directional compressive force on the sample, i.e., by moving the σ_1 piston (*Richter et*
137 *al.*, 2016). The σ_1 piston had to push through a lead piece (so-called run-in) before it
138 touched the alumina forcing block on top of the sample. At this point sample
139 deformation started. When the motor was stopped, the temperature was decreased to
140 200°C within 2-3 minutes with cooling rates between 150°C and 300°C per minute
141 to quench the microstructure. Five experiments included a hydrostatic hot-pressing
142 stage (at 1000°C ; 1.5-1.6 GPa confining pressure), where the sample was left for 20
143 hours before decreasing the temperature (2.5°C per minute) to deformation
144 conditions. These samples will be referred to as 'hot pressed'.

145 Two types of experiments were conducted. Experiments of type 1 were
146 conducted at constant displacement rates. The constant displacement rate of the σ_1
147 piston resulted in an approximately constant shear strain rate. Type 2 experiments are
148 strain-rate stepping experiments, where the displacement rate was decreased by about
149 one half or one order of magnitude after reaching peak strength. When steady state
150 was achieved for this reduced rate the displacement rate was decreased again. During

151 the last step, the displacement rate was set again to the initial value.

152

153 2.2 Mechanical data: acquisition and processing

154 During the experiment, the applied force on the σ_1 piston, the displacement of
155 the σ_1 piston, and the oil pressure of the confining pressure cylinder were recorded
156 with a frequency of 1 Hz. These signals were converted to maximum principal stress
157 (σ_1 in MPa), minimum principal stress (σ_3 in MPa), and axial displacement (d_a in
158 mm). Data processing and determination of differential stress ($\Delta\sigma$), shear stress (τ) and
159 shear strain (γ) were performed according to *Richter et al.* (2016), including a
160 correction for confining pressure build-up and piston overlap. The shear strain (γ) is
161 calculated as the sum of incremental shear strains between recorded data points. For
162 each data point, a reduced width of the shear zone is used by assuming a constant
163 linear thinning of the sample for a known initial average width from hot pressing
164 experiments and final deformed width measured in thin sections.

165 For the determination of the stress exponents and the activation energies, data
166 from the strain rate-stepping experiments and some of the constant shear strain-rate
167 experiments performed at the same deformation temperatures were used. The mean
168 steady-state differential stress and the mean shear strain-rate of each strain-rate step
169 and the differential stress at $\gamma \sim 3$ and the average shear strain rate of the constant
170 shear strain rate experiments were used. The stress corrections of Holyoke and
171 Kronenberg (2010) were not applied because they were not found to be appropriate
172 for the shear experiments in our apparatus (*Richter et al.*, 2017).

173 The friction coefficient of the samples was calculated for the 45° angle of the
174 forcing block pre-cut using a simple Mohr Coulomb construction: $\mu = \tau / \sigma_n$ (Fig. 1b).
175 During deformation, the normal stress on the sample (σ_n) increases (σ_n is calculated as

176 2D mean stress). Steady-state shear stress at $\gamma = 3$ was used to calculate the friction
177 coefficient for high strain experiments. For samples only loaded to peak-strength, the
178 maximum friction coefficient was calculated. In the strain rate-stepping experiments,
179 the stress value before decreasing the displacement rate was used for the first step, and
180 for the later strain rate steps the mean values at steady-state conditions were used.

181

182 2.3 Microstructure and texture analysis

183 For the preparation of polished thin sections, the sample jackets were cut
184 parallel to the shear displacement direction and the samples were impregnated under
185 vacuum with epoxy before cutting. For all subsequent microstructural analyses, the
186 samples are viewed with a sinistral shear sense (shear zone boundary is horizontal).
187 All samples were analysed with light microscopy and scanning electron microscopy
188 (SEM; for imaging: a field emission Philips XL 30 ESEM, for electron backscatter
189 diffraction: a field emission Zeiss Merlin SEM with a Nordlys nano camera).

190 Electron backscatter diffraction (EBSD) was used to obtain quartz crystal
191 orientations. Polishing and lapping for EBSD analysis was carried out with colloidal
192 silica suspension Struers OP-U non dry for 3-6 minutes. Samples were coated with a
193 thin carbon layer to prevent charging under high vacuum conditions. Acceleration
194 voltages between 10 kV and 15 kV were used with step sizes of 0.1 to 0.2 μm . EBSD
195 data were measured with AZtec software and analysed with the MTEX toolbox
196 (*Hielscher and Schaeben, 2008*). Initial noise reduction was performed with
197 CHANNEL 5 software by removing isolated points and replacing non-indexed points
198 with the orientation of their neighbours (iteratively filled starting with eight similar
199 neighbours down to six or five similar neighbours).

200 Grain maps obtained with MTEX show individual grains separated by a

201 misorientation angle of 10° . Dauphine twin boundaries (misorientation of $60 \pm 5^\circ$)
202 were not considered grain boundaries. Grains had to contain at least five pixels to be
203 considered as grains. The 2D grain diameters (d_{equ} = diameter of area equivalent
204 circle) were used as input for the StripStar programme (*Heilbronner and Barrett,*
205 2014) to obtain the 3D diameters (D_{equ} = diameter of the volume equivalent spheres).
206 The volume weighted distributions of D_{equ} were fitted with a Gaussian Normal, the
207 modal value and the dispersion being given by the mean and the standard deviation.
208 For details on segmentation and grain size determination, see *Heilbronner and Kilian*
209 (2017).

210 The kernel average misorientation of a grain (gKAM) is calculated from noise
211 reduced EBSD data with a kernel of an order of 4 (see *Kilian and Heilbronner, 2017*).
212 The 'mis2mean' value of each point of a grain is determined with MTEX. Averaging
213 the 'mis2mean' value of a single grain yields the grain orientation spread (GOS). The
214 GOS is normalised for the long axis (GOS_{la}) to account for the grain-size dependence,
215 which is especially pronounced for highly elongated grains. Both, GOS_{la} and gKAM,
216 indicate the misorientation density of a grain and are therefore considered a measure
217 for intragranular deformation (for derivations of GOS, see *Cross et al., 2017*).

218 Using smoothed grain boundaries, the PARIS factor, a measure for grain
219 boundary lobateness (*Panozzo and Hürlimann, 1983*) is used. It is defined by the
220 difference between the length of the convex hull of a grain and that of the real
221 perimeter.

222

223 3. Mechanical results

224 27 constant shear strain-rate experiments between 500°C and 1000°C (Table
225 1) and five strain rate-stepping experiments at shear strain rates between $\sim 2.5 \times 10^{-6} \text{ s}^{-1}$

226 ¹ and $\sim 2.5 \times 10^{-3} \text{ s}^{-1}$ for $\sim 650 \text{ }^\circ\text{C}$, $800 \text{ }^\circ\text{C}$, $900 \text{ }^\circ\text{C}$ and $1000 \text{ }^\circ\text{C}$ (Table 2) were
227 conducted.

228 **Insert Table 1 and 2 here**

229

230 3.1 Temperature dependence

231 Above temperatures of $\sim 650 \text{ }^\circ\text{C}$, samples clearly weaken systematically with
232 increasing temperature, whereas at $650 \text{ }^\circ\text{C}$ and below, the strength-temperature-
233 relationship is weak or unsystematic (Fig. 2a). Samples deformed at temperatures
234 below $700 \text{ }^\circ\text{C}$ show steady-state behaviour or slight strain hardening. At $700 \text{ }^\circ\text{C}$ or
235 higher, the samples deform below the Goetze criterion ($\Delta\sigma = P_c$) and show steady-
236 state or minor strain weakening at high strain. The difference in strength between 650
237 $^\circ\text{C}$ and $700 \text{ }^\circ\text{C}$ is very large ($\sim 1300 \text{ MPa}$). At low temperatures, no significant stress
238 drop or strain weakening occur after yield strength, except for 450br and 481br (see
239 Table 1). These samples show a stress drop as a result of slip along the forcing block.
240 In addition, the alumina forcing blocks started to deform because of the high stresses
241 (e.g., 415br).

242 The slopes of the loading curves up to temperatures of $650 \text{ }^\circ\text{C}$ are almost
243 identical up to a differential stress of $\sim 1 \text{ GPa}$. At temperatures above $650 \text{ }^\circ\text{C}$ the slope
244 decreases with decreasing strength and shear strain rate (Figs. 2, 3 and 4).

245 **Insert Figure 2 here**

246

247 3.2 Pressure dependence

248 At $650 \text{ }^\circ\text{C}$, the sample strength increases with increasing confining pressure,
249 whereas at higher temperatures ($700 \text{ }^\circ\text{C}$ and $800 \text{ }^\circ\text{C}$; Fig. 3) strength decreases with
250 increasing confining pressure. At $800 \text{ }^\circ\text{C}$, a pressure dependence is not obvious

251 between 1.0 and 1.5 GPa, but between 0.5 and 1.0 GPa, the weakening with
252 increasing confining pressure is very clear (Fig. 3).

253 **Insert Figure 3 here**

254

255 3.3 Influence of initial grain size

256 When hot pressed at 1000 °C for 20 hours prior to deformation, samples
257 systematically reach higher strengths compared to samples without hot pressing (Fig.
258 2c). The difference in flow stress is at least 500 MPa at 600 °C at $\gamma \sim 3$ (the forcing
259 blocks start to deform in the hot-pressed sample at such high stresses). At 700 °C, the
260 hot-pressed sample is about 900 MPa stronger and shows strain hardening, whereas
261 the non-hot pressed sample weakens. At 800 °C, the difference is ~200 MPa and both
262 samples show strain weakening.

263 One sample with a small initial grain-size fraction (7-11 μm) is deformed at
264 1.5 GPa, 800 °C and $2.5 \cdot 10^{-5} \text{ s}^{-1}$ (Fig. 2c, 445br). It is weaker than the experiments
265 with a larger initial grain-size fraction ($< 100 \mu\text{m}$) performed at the same strain rate
266 and temperature conditions. At $\gamma \sim 3$, the differential stress of 445br is less than half as
267 high as of 388br (difference ~500 MPa). Steady-state conditions exist between a
268 shear strain of ~0.5 to 2.5, after that the sample hardens by ~100 MPa until the end of
269 the experiment.

270

271 3.4 Strain rate dependence

272 Strain rate has a pronounced effect on sample strength at temperatures above
273 600 °C. At 650 °C and 800 °C, increasing the strain rate by one order of magnitude
274 shifts the flow stress from below to above the Goetze criterion (Fig. 2b). At 900 °C
275 the same shift is achieved by increasing the strain rate by two orders of magnitude.

276 Strain rate-stepping experiments in combination with constant displacement
277 experiments at different rates show distinct strain rate dependence for all higher
278 temperature experiments, except at 650 °C, where the rate dependence is only
279 observed at very low strain rates ($\sim 10^{-6} \text{s}^{-1}$; Fig. 4). The fastest strain rate causes the
280 highest stresses, and lower stresses with increasing temperature and lower strain rate
281 occur at all strain rates (Fig. 4). The strain-rate-stepping tests are plotted together with
282 constant strain-rate tests to check the reproducibility of the results. At 900 °C and
283 1000 °C, the last step has slightly higher shear strain-rates than the first step (because
284 of the thinning of the shear zone), and therefore, the differential stress is slightly
285 higher. The experiment at 900 °C shows abrupt strain hardening at the end of the last
286 strain rate step. This behaviour is a consequence of the sample geometry where the
287 lower forcing block collided with the upper alumina piston. At 800 °C, the experiment
288 failed at the slowest strain rate step.

289 **Insert Figure 4 here**

290 One strain-rate-stepping experiment included a hot-pressing stage prior to
291 deformation (480br). The initial sample strength is similar to that of the hot-pressed
292 constant-displacement experiment (419br, Fig. 4). At lower strain rates, the stresses of
293 the hot-pressed sample are similar the sample 388br without hot pressing. At the end
294 of the experiment, the strain-stepping sample (480br) is 200 MPa weaker than the
295 constant rate sample (419br).

296

297 4. Microstructural observations

298 The brittle and the viscous microstructures are described in terms of being
299 discrete Riedel surfaces without discernible shear displacement and a synthetic low-
300 angle orientation (R) or an antithetic high-angle orientation (R') with respect to the

301 shear plane are termed "Riedel surfaces". When such features have a discernible
302 width, they are termed "shear bands" (SB, not distinguishing C or C' orientations in
303 the sense of *Berthé et al. (1979)*). Riedel surfaces and shear bands may occur in the
304 same sample. Elongated quartz grains or grain aggregates typically develop a shape
305 preferred orientation, which is termed "foliation" (F) here.

306

307 4.1 Starting material

308 From analyses with a laser diffraction particle size analyzer, we know that the
309 crushed quartz powder initially has a fractal size distribution with a fractal dimension
310 of 2.4 in the size range up to 100 μm . During the run-in of the σ_1 -piston, before the
311 piston touches the forcing block, the samples are exposed to varying periods (up to 25
312 hours) of hydrostatic heat treatment. During this time, the same kind of grain growth
313 takes place as in the healing faults described by Keulen et al. (2008), so that the grain-
314 size fraction $<1 \mu\text{m}$ disappears (Fig. 5). Grain growth creates a normal distribution of
315 grains at the lower size end of the fractal distribution.

316 A few samples were additionally hot pressed after reaching experimental
317 conditions (20h at 1000°C). After 25 h and 800°C, the 3D mode of the grain size
318 fraction $<30 \mu\text{m}$ is $\sim 9.1 \mu\text{m}$, and after 20 h at 1000 °C, it is $\sim 12.8 \mu\text{m}$ (Table 3). The
319 initial gouge material is now fully compacted and fully cohesive. For the higher
320 temperature samples (700 °C to 1000 °C), porosity is $< 1\%$, whereas for lower
321 temperature samples (500 to 600°C) porosity is up to $\sim 10 \%$ (values obtained from
322 image analysis) due to a lack of grain growth.

323 **Insert Figure 5 here**

324 **Insert Table 3 here**

325

326 4.2 Deformation microstructures

327 Low-temperature samples ($T \leq 650^\circ\text{C}$) are dominated by a complex Riedel
328 surface geometry with synthetic R and rare antithetic R' surfaces (Fig. 6; samples
329 450br, 479br, 415br, 435br). The R surfaces form at an angle of $20\text{-}30^\circ$ to the
330 direction of the applied load (σ_1 - direction) and have a predominantly brittle
331 appearance at 500°C . The R surfaces are not connected and never transect the whole
332 sample. These observations, in conjunction with the mechanical data, indicate that
333 these R surfaces do not fully control the sample strength. Most original clasts are still
334 visible but have rounded edges and corners. Undulatory extinction and discrete
335 surfaces with small misorientation and with a high angle towards the shear zone
336 boundary exist in several clasts at 650°C (Fig. 6; sample 435br). Tails at clasts are
337 partly developed without resolvable small particles at the light or scanning electron
338 microscope scale at 650°C . Deformation lamellae start to develop in clasts at 600°C .
339 Shear bands are developed at 650°C in addition to the R surfaces. At 600°C , zones
340 with small, equi-axed grains evolve in R surface orientation. These zones become
341 more pronounced at higher temperatures, defining shear bands (Fig. 6; samples 479br,
342 435br, 493br, 419br).

343 **Insert Figure 6 here**

344 At higher temperatures ($T \geq 700^\circ\text{C}$), viscous processes dominate the
345 microstructure (Fig. 6; samples 383br, 388br, 412br, 493br, 419br). At 700°C and
346 800°C , a shear band and foliation fabric is developed (Figs. 6, 7; samples 383br,
347 388br, 412br, 493br, 419br, 452br, 447br, 448br, 499br), and Riedel surfaces are
348 absent. Elongated tails of recrystallized grains develop at rounded clasts. With
349 increasing shear strain and higher temperature, the shear band and foliation fabric
350 evolves into a single penetrative foliation of elongated clasts and recrystallised grains.

351 Large clasts show more penetrative recrystallisation with increasing temperature of
352 deformation and with increasing strain. At $\gamma \sim 5$ about 10 % clasts remain at 700 °C
353 and 5 % clasts can be distinguished at 800 °C (Fig. 6; samples 383br, 493br, 388br).
354 Rounded clasts are predominant at 700 °C. At 800 °C, highly elongated aggregates of
355 recrystallised grains dominate. Deformation lamellae are pronounced in clasts at 700
356 °C and 800 °C, but rare at 900 °C. At 900 °C and 1000 °C, the elongated aggregates
357 of recrystallised grains give way to a more homogeneous groundmass of recrystallised
358 grains with some clasts preserved in the recrystallised matrix (Fig. 6; samples 412br,
359 337br).

360 In samples with hot pressing (20h at 1000°C), pre-existing cracks are anneal
361 and barely visible. Subsequent deformation at 600 °C does not produce an obvious
362 brittle deformation fabric of the sample (Fig. 6; sample 415br). No Riedel surfaces
363 develop and only minor grain-boundary alignment occurs. At 700 °C and high strains,
364 a shear band and foliation fabric is present with several remaining rounded clasts that
365 develop tails (Fig. 6; samples 493br). At a given shear strain, the foliation angle with
366 the shear zone boundary is clearly larger than in samples without hot pressing and the
367 microstructure appears less deformed. At 800 °C, a pervasive foliation dominates the
368 fabric, again with a slightly larger angle after similar shear strain than in the hot
369 pressed sample (Fig. 6; sample 483br). More or less elongated clasts are present
370 compared to the sample without hot pressing.

371

372 4.3 Effect of strain rate on microstructure

373 Three constant shear strain-rate experiments were conducted at shear strain
374 rates different from $\sim 2.5 \cdot 10^{-5} \text{ s}^{-1}$ (Fig. 2b). At 650 °C and a shear strain rate of
375 $0.35 \cdot 10^{-5} \text{ s}^{-1}$ several grains show more brittle deformation, and less rounded grain

376 shapes at low shear strain ($\gamma = 1.1$; Fig. 7; sample 500br). Shear bands are absent and
377 the fabric resembles samples deformed at lower temperatures at $2.5 \times 10^{-5} \text{ s}^{-1}$ (Fig. 6;
378 sample 479br). At 800 °C and 900 °C, faster shear strain rates ($27 \cdot 10^{-5} \text{ s}^{-1}$ and $189 \cdot 10^{-5}$
379 s^{-1} , respectively) cause a more heterogeneous deformation, shear bands, and samples
380 resemble those deformed at ~ 100 to 200 °C lower temperatures at strain rates of $2.5 \times$
381 10^{-5} s^{-1} (Fig. 7; samples 447br, 499br).

382 **Insert Figure 7 here**

383

384 4.4 Effect of confining pressure on microstructure

385 Samples deformed at 1.0 GPa confining pressure and 650 °C show Riedel
386 surfaces and less commonly shear bands, very similar to samples deformed at 1.5 GPa
387 confining pressure (Figs. 6, 7; samples 494, 435br). Clast shapes are less rounded than
388 at 1.5 GPa confining pressure (cf. Figs. 6 and 7, shear strain is higher in Fig. 7;
389 samples 494br, 435br). At 700 °C, 1.0 GPa, the samples are characterised by a larger
390 number of shear bands and less homogeneous deformation than at 1.5 GPa (cf. Figs. 6
391 and 7; samples 494br, 435br), whereas at 800 °C, 1.0 GPa, more clasts survive and the
392 recrystallisation is less complete than at 1.5 GPa (cf. Figs. 6 and 7; samples 448br,
393 388br).

394 At 0.5 GPa confining pressure and 800 °C, deformation is localised in long
395 synthetic R surfaces accompanied by several transgranular fractures (Fig. 8; sample
396 386br). Most of the displacement is accumulated along the R surfaces, where the
397 gouge material is highly pulverised (submicron-scale) (Fig. 8b). Large clasts are
398 slightly rounded at the edges (Fig. 8a) and microstructures resemble those of the
399 650°C, 1.5 GPa sample (cf. Fig. 6; sample 435br). In the series of 0.5, 1.0, and 1.5
400 GPa samples, more brittle deformation microstructures clearly develop with

401 decreasing confining pressure, particularly toward the lower pressure end.

402 **Insert Figure 8 here**

403

404 4.5 Grain size

405 At conditions of 1.5 GPa confining pressure and shear strain rates of $\sim 3 \cdot 10^{-5} \text{ s}^{-1}$
406 ¹, the 3D mode of recrystallized grain size increases from 2.1 μm at 700 °C to $>15 \mu\text{m}$
407 at 1000 °C (Fig. 9a, Table 3). The sample that was prepared with a grain-size fraction
408 of 7-10 μm , yields a slightly larger grain size of 4.4 μm compared to the standard
409 sample that yields 4.1 μm at the same temperature (800°) (Fig. 9b). At 1.0 GPa
410 confining pressure, the recrystallised grain size is slightly smaller than at 1.5 GPa (1.5
411 versus 2.1 μm at 700 °C, and 3.3 versus 4.1 μm at 800°C). At 0.5 GPa and 800 °C, no
412 recrystallization occurs. Shear strain rates faster than the standard value of $3 \cdot 10^{-5} \text{ s}^{-1}$
413 cause smaller recrystallised grain sizes. At 800 °C and 10 times faster, the 3D mode is
414 2.0 μm versus 4.1 μm , at 900 °C and 100 times faster, it is 1.5 μm versus 6.1 μm
415 (Table 3).

416 **Insert Figure 9 here**

417 An initial hot-pressing stage causes growth of the small grains (Fig. 5, Table 3)
418 and the resulting grain sizes at the onset of deformation are larger. After deformation,
419 the recrystallized grain size of these samples is similar to that of samples without hot
420 pressing (1.6 μm compared to 2.1 μm at 700 °C, 4.8 μm compared to 4.1 μm at 800
421 °C; cf. Fig. 9b, Table 3).

422

423 4.6 Texture

424 The values of GOS and gKAM, indicators of intragranular deformation,
425 decrease with increasing temperature between 700 °C and 1000 °C (Fig. 10) with hot

426 pressed samples showing similar values to samples without hot pressing. For
427 individual grains, neither PARIS factors, indicating high lobateness, nor grain size
428 correlate with GOS and gKAM values.

429 **Insert Figure 10 here**

430 Above 650 °C, the recrystallised matrix dominates the CPO for standard
431 confining pressure (1.5 GPa) and standard shear strain rates ($\sim 2.5 \cdot 10^{-5} \text{ s}^{-1}$). Separate
432 pole figures are calculated for smaller and larger fractions of recrystallized grains
433 (Fig. 11). The delimiting size between small and large grains is derived from the 3D
434 mode of the size distribution of recrystallized grains ($< 25 \mu\text{m}$; Fig. 11). Pole figures
435 are calculated for grains with 2D diameters (= area equivalent diameters) larger or
436 smaller than the delimiting 3D diameter, i.e., pole figures for grains larger than the 3D
437 mode and pole figures for grains predominantly smaller than the 3D mode. For the
438 larger grain size fraction, the CPO is always considerably stronger. The CPO
439 progressively evolves between 700 °C and 1000 °C. At 700 °C and 800 °C, there is
440 one peripheral maximum of the *c*-axes slightly rotated with the sense of shear. At 900
441 °C, a peripheral and a central *c*-axis maximum both are established. Towards 1000 °C
442 the CPO evolves to a single central *c*-axes maximum.

443 The pole figures of the fine-grained fraction shows a different development
444 with increasing temperature. At 700°C, the CPO is more diffuse and the peripheral *c*-
445 axis maximum is less pronounced compared to that of the larger grain size. The
446 orientation of the maximum is similar to the maximum of the larger grains. At 800 °C,
447 the smaller grains ($< 4 \mu\text{m}$) again show a more diffuse CPO, but the *c*-axis maximum
448 is rotated by 20° with the sense of shear with respect to that of the larger grains. At
449 900 °C, the peripheral *c*-axes are more dispersed and the *c*-axis maximum is rotated
450 by 10° with the sense of shear compared to that of the larger grains. The central

451 maximum of *c*-axes is less pronounced than that of the larger grains. The central *c*-
452 axis maximum at 1000 °C is present in fine grains as well as in larger grains. A
453 rotation with the sense of shear cannot be identified.

454 **Insert Figure 11 here**

455

456 5. Discussion

457 Our series of experiments employs crushed material of natural quartz. This
458 approach simulates a cataclasite produced by brittle deformation in nature such as
459 seismic or aseismic movement along a fault. Such a cataclastic rock deforms
460 dominantly by frictional mechanisms at low temperatures, high strain rates and low
461 confining pressures, and by fully viscous mechanisms at higher temperatures, lower
462 strain rates and higher confining pressures. The differences in the mechanical data and
463 microstructures demonstrate that the starting material used here is adequate to study
464 the brittle-to-viscous transition (BVT) as a function of pressure, temperature and
465 strain rate in polycrystalline quartz rocks. Another aspect that may be studied by using
466 such a material is how deformation mechanisms change as a function of deformation
467 history, i.e. from a brittle precursor material to a subsequently viscously deformed
468 material. Such a transition may occur, e.g., as a transition from seismic to postseismic
469 creep.

470

471 5.1 Mechanical parameters of the brittle-to-viscous transition

472 The BVT can be defined on the basis of different parameters: mechanical data
473 with respect to the Goetze criterion ($\Delta\sigma \approx P_c$); pressure dependence of differential
474 stress; friction coefficients and stress exponents, and microstructural transition from
475 dominantly brittle to viscous deformation structures.

476 The greatest difference in differential stress at a strain rate of $\sim 10^{-5} \text{ s}^{-1}$ is
477 observed between the 600/650 °C and 700 °C samples (Fig. 2a) where the strengths
478 lie above and below the Goetze criterion that marks the transition from brittle ($\Delta\sigma >$
479 P_c) to viscous ($\Delta\sigma < P_c$) deformation (“plastic” in *Kohlstedt et al.*, 1995). This
480 observation places the BVT between 650 °C and 700 °C for a strain rate of $\sim 10^{-5} \text{ s}^{-1}$ in
481 terms of the Goetze criterion.

482 For experiments by others at the same axial strain rates as our shear strain rates
483 (*Hirth and Tullis*, 1994), the strength of quartzite samples at 700 °C and 850 °C (at P_c
484 =1.2 GPa) shows substantial scatter, but similar average values as our samples. The
485 deformation processes in that study were identified as semi-brittle flow (700 °C) and
486 dislocation creep (850 °C). The similar sample strengths of the intact rock and our
487 gouge material indicate that at higher temperatures the cataclasite is fully compacted
488 and behaves like a normal polycrystalline material. We attribute the temperature
489 differences for the BVT between our samples and those of *Hirth and Tullis* (1994) to
490 differences in the amount of total strain attained and that samples in shear are weaker
491 than in axial compression, so that localisation in coaxially deformed samples occurs in
492 narrower zones than in our shear zones, causing greater strain rates.

493 The BVT coincides with another mechanical observation in the samples: At
494 stresses below the Goetze criterion, the slope of the loading part of the stress strain
495 curves decreases systematically with decreasing flow stress (Figs. 2, 3 and 4). The
496 loading curve in the Griggs apparatus is not purely elastic at higher temperatures. The
497 systematically decreasing slope at higher temperatures is the result of increasing
498 viscous deformation processes in the samples during loading. In experiments
499 deformed above the Goetze criterion, the slope is similar for all samples, indicating no
500 substantial viscous deformation processes during loading.

501 Higher confining pressures cause greater sample strength for frictional sliding
502 (*Byerlee, 1978*) and cracking (*Paterson and Wong, 2005* and references within),
503 whereas the viscous creep strength of wet quartz decreases with increasing confining
504 pressure (*Tullis et al., 1979; Kronenberg and Tullis, 1984*). The observed
505 strengthening of samples with increasing pressure at low temperatures (650 °C, Fig. 3)
506 is consistent with frictional or brittle behaviour (cf. *Hirth and Tullis, 1994*). The
507 lowering of flow-stress with increasing pressure observed at $T > 650$ °C (Fig. 3)
508 indicates the onset of viscous deformation. At a first glance, the difference in flow
509 stress between samples deformed at 1.0 and 1.5 GPa P_c (453br and 437br) does not
510 appear significant (Fig. 3), but when seen with respect to the Goetze criterion, the
511 difference is well defined: The sample at 1.5 GPa (437br) barely reaches the Goetze
512 criterion, whereas the sample at 1.0 GPa (453br) is clearly above it. The difference in
513 flow stress is clearly established at low P_c between 0.5 GPa and 1.0 GPa (Fig. 3). A
514 very similar trend was observed in novaculite by *Kronenberg and Tullis (1984)*: a
515 smaller stress dependence at $P_c \geq 1.0$ GPa and a distinct pressure dependence at lower
516 confining pressures. The decreasing peak stress with increasing pressure is related to
517 increased water fugacity and its enhancing effect on crystal plasticity (*Tullis et al.,*
518 *1979; Kronenberg and Tullis, 1984; Paterson and Luan, 1990; Kohlstedt et al., 1995*).
519 The pressure dependence delineates the BVT also in the range of 650 °C to 700 °C for
520 $\sim 10^{-5}$ s⁻¹.

521

522 5.2 Coefficient of friction

523 To delineate the BVT better, mechanical properties such as friction coefficient
524 and stress exponent can be used. Frictional deformation should be rather temperature
525 insensitive up to 440 to 500 °C (*Paterson and Wong, 2005, p. 172*), whereas viscous

526 deformation is by definition temperature dependent. Viscous flow laws imply a strong
527 positive stress dependence for the strain rate (*Orowan, 1940; Kohlstedt and Hansen,*
528 2015), whereas in frictional deformation the strain rate at slow sliding rates (as
529 employed in this study) are assumed to be weakly dependent or strain-rate
530 independent as a first approximation (*Byerlee, 1978; Kohlstedt et al., 1995; Paterson*
531 *and Wong, 2005, p. 178, and references therein*). To better use the mechanical data for
532 defining the BVT, we determined the friction coefficients and stress exponents for
533 many of our experiments, even if these mechanical properties are outside the range of
534 conditions for which brittle deformation would be expected.

535 At 1.5 GPa and below 700 °C, the friction coefficient ($\mu \sim 0.45$; Fig. 12) is
536 somewhat less than normal rock friction values (0.6; *Byerlee, 1978*). The temperature
537 dependence is very small up to 650 °C. From 700 °C to 1000 °C, the friction
538 coefficient shows a systematic temperature dependence. At 1.5 GPa confining
539 pressure and a strain rate of $2.5 \cdot 10^{-5} \text{ s}^{-1}$, the friction coefficient $\mu \sim 0.3$ to 0.05, at a
540 strain rate of $2.5 \cdot 10^{-4} \text{ s}^{-1}$, $\mu \sim 0.35$ to 0.16. At strain rates of $\sim 10^{-6} \text{ s}^{-1}$, the friction
541 coefficients become very small ($\mu < 0.02$). Low confining pressures cause greater
542 friction coefficients between 650 °C and 800 °C (Fig. 12b): At 0.5 GPa and 800 °C,
543 the greatest friction coefficient occurs ($\mu = 0.53$), which is twice the value at 1.0 GPa.
544 A distinct jump in the values occurs for the friction coefficient between 650 °C and
545 700 °C for a strain rate of $2.5 \times 10^{-5} \text{ s}^{-1}$, coinciding with the Goetze criterion (Fig. 12).

546 **Insert Figure 12 here**

547 Frictional deformation in quartz and granite, in general, is only weakly
548 temperature-dependent below 350-400 °C (*Blanpied et al., 1995; Chester and Higgs,*
549 1992), so that the smaller friction coefficients and the strong temperature dependence
550 at $T > 650 \text{ °C}$ also indicate a change in deformation mechanism to viscous behaviour.

551 The pronounced strain rate dependence of strength between 650 °C and 900 °C
 552 (Figs. 2b, 4, 12a) is present down to temperatures as low as 650 °C (Fig. 4). This
 553 behaviour emphasises the contribution of viscous deformation processes, and thus a
 554 semi-brittle character at these low temperatures. It is remarkable that in one sample
 555 (500br) at temperatures of 650 °C, the flow stress can be below the Goetze criterion.
 556 However, in that sample, steady state was not achieved because at the low strain rate
 557 of $\sim 10^{-6} \text{ s}^{-1}$ only a small total strain was attained (Figs. 2b and 4). Strain rates of $\sim 10^{-4}$
 558 s^{-1} are required to achieve sample strengths above the Goetze criterion and realistic
 559 friction coefficients at $T = 800 \text{ °C}$, whereas a strain rate of $\sim 10^{-3} \text{ s}^{-1}$ is required at $T =$
 560 900 °C (Figs. 2b, 12a). These results can be used to extrapolate the BVT to lesser
 561 strain rates (see below).

562

563 5.3 Stress exponent and activation energy

564 Based on a power-law creep relationship, the stress and strain rate data can be
 565 used to derive a stress exponent and an activation energy (Fig. 13):

$$566 \quad \dot{\gamma} = A \cdot \Delta\sigma^n \cdot \exp\left(-\frac{Q}{RT}\right) \quad (\text{Eq. 1})$$

567 where $\dot{\gamma} [\text{s}^{-1}]$ is the shear strain rate, $A [\text{MPa}^{-n} \cdot \text{s}^{-1}]$ is a material-dependent
 568 constant, $\Delta\sigma [\text{MPa}]$ is the differential stress, n is the stress exponent, $Q [\text{J/mol}]$ is the
 569 activation energy, $R [\text{J} \cdot \text{mol}^{-1} \cdot \text{K}^{-1}]$ is the ideal gas constant and $T [\text{K}]$ is the
 570 temperature. At low temperatures ($\sim 650 \text{ °C}$), the n -value is high ($n = 6.4 \pm 1.3$). The
 571 stress exponent of high-temperature experiments ($800\text{-}1000 \text{ °C}$) is 1.9 ± 0.6 (Fig. 13a)
 572 and shows little variation with temperature. For high temperature experiments, the
 573 activation energy is determined to be $\sim 170 \pm 72 \text{ kJ/mol}$ (Fig. 13b).

574 The highest stress values at 900 °C (499br at $\sim 10^{-3} \text{ s}^{-1}$) and 800 °C (447br, fast step of
 575 488br at $\sim 10^{-4} \text{ s}^{-1}$; Fig. 4) are not included in the determination of the stress exponent

576 and the activation energy because steady state is not indicated by the mechanical data.

577 **Insert Figure 13 here**

578 The calculated stress exponents confirm the transition from brittle-dominated
579 to viscous-dominated deformation at temperatures of 650 / 700 °C, and strain rates of
580 $\sim 10^{-5} \text{ s}^{-1}$. The stress exponent of ~ 6.4 of samples deformed at low temperatures (Fig.
581 13) is too high for dislocation creep deformation with typical values of $n = 3-5$ (e.g.,
582 *Karato, 2008; Paterson, 2013; Kohlstedt and Hansen, 2015*), thus indicating the
583 beginning of the power-law breakdown, i.e., the lack of rate-controlling viscous
584 deformation at $T < 700 \text{ °C}$. On the other hand, the n -values of 1.8 to 2 derived for
585 samples deformed at $T > 700 \text{ °C}$ (Fig. 13) are too low for dislocation creep, yet rather
586 high for diffusion creep.

587 Our determined Q-value of 168 to 170 kJ/mole is very similar to values
588 determined by *Jaoul et al. (1984)* and lies in the range of other experimentally
589 determined values for dislocation creep (Table 4). Activation energies for diffusion
590 creep vary considerably and the values are highly dependent on the involved material
591 (silicon or oxygen diffusion) and the controlling process (transport or reaction) (e.g.,
592 137-178 kJ/mol for silicon diffusion in *Farver and Yund, 2000*; 142-243 kJ/mol for
593 oxygen diffusion in *Giletti and Yund, 1984*; 220 kJ/mol in *Rutter and Brodie, 2004a*).
594 Hence, the range of previously determined activation energies and the precision of our
595 determination are inadequate to conclude decisively about the nature of the process
596 causing it. *Rutter and Brodie, 2004a,b* are the only studies that have determined
597 activation energies for both processes, and the values are very similar (Table 4). Based
598 on this evidence and our observations of a constant stress exponent of $n \sim 2$ between
599 800 °C to 1000°C, we would like to maintain the idea that the activation energies of
600 contributing diffusion creep and dislocation creep mechanisms should be similar.

601 **Insert Table 4 here**

602 A stress exponent ($n \sim 2$) has been derived for deformation by dislocation-
603 accommodated grain-boundary sliding by, e.g., *Kohlstedt and Hansen* (2015).
604 However, the rather strong CPOs occurring in our samples argue against grain
605 boundary sliding (GBS). Although evidence exists for strong CPOs produced by GBS
606 (e.g., *Schmid et al.*, 1987; *Gomez Barreiro et al.*, 2007; *Hansen et al.*, 2011), the
607 general consensus is that dominant GBS should produce weak CPOs (e.g., *Edington et*
608 *al.*, 1976; *Bell and Langdon*, 1967). A possible explanation is a combination of
609 deformation processes, where dislocation creep produced strong CPOs and n -values of
610 3 to 5, in tandem with grain-size-sensitive diffusion creep, including grain boundary
611 sliding, which produced weak CPOs. Both together yield n -values of ~ 2 .

612 To derive a grain-size exponent, we used samples 388br (standard), 419 (hot
613 pressed) and 445br (sieved to 7-11 μm), which were all deformed at 800 °C, 1.5 GPa
614 and 10^{-5} s^{-1} , but yielded significantly different differential stresses. The grain size
615 exponent $p = m / n$, where m is the slope of the linear fit in the log(stress) versus
616 log(grain size) diagram (Fig. 13c) and n is the average stress exponent of 1.9. The
617 correlation coefficient for this fit is very low ($R=0.258$), and the value of $p = 1.08$ is
618 not well constrained. While our database is far too small for a reliable determination
619 of the grain size exponent, it is nevertheless interesting to note that similar uncertainty
620 is present in published data (Rutter and Brodie, 2004a).

621

622 5.4 Microstructure development at the brittle-to-viscous transition

623 The microstructural changes correspond to the transition conditions inferred
624 from the mechanical data. At strain rates of $\sim 10^{-5} \text{ s}^{-1}$, the samples at $T \geq 700 \text{ °C}$ show
625 features of dynamic recrystallisation, whereas at lower temperatures, Riedel fractures

626 across grains are common (Figs. 6 and 7). The transition between brittle and viscous
627 microstructures is clearly visible between 650 °C and 700 °C at the strain rate of $\sim 10^{-5}$
628 s^{-1} and confining pressures of 1.0 and 1.5 GPa. This observation is in excellent
629 agreement with the transition defined by mechanical data discussed above. The effect
630 of confining pressure becomes obvious in the microstructures at low confining
631 pressure of 0.5 GPa, where samples at 800 °C show predominantly brittle
632 microstructures (Fig. 8). The strain rate effect is not as clearly expressed in the
633 microstructure: At 650 °C, deformation at a strain rate of $\sim 10^{-6} s^{-1}$ produces similar
634 microstructures as a strain rate of $\sim 10^{-5} s^{-1}$ (cf. Figs. 6, 7). But at $\sim 10^{-5} s^{-1}$, clasts are
635 more rounded, and Riedel surfaces and shear bands are more pronounced. These
636 differences may well be due to the less total strain of the sample for a slower strain
637 rate. The faster strain rates at 800 °C and 900 °C yield microstructures that resemble a
638 mixture of microstructures at a strain rate of $\sim 10^{-5} s^{-1}$ between 600 °C and 700 °C (for
639 high shear strain): several remaining large clasts coexist with clusters of recrystallised
640 grains in a fabric dominated by shear bands (below referred to as “transitional”).

641 At stresses above the Goetze criterion, typical regime 1 stress-strain curves
642 with pronounced weakening after peak stress (*Hirth and Tullis (1992)*) are only
643 observed at 800 °C and a strain rate of $\sim 2.5 \cdot 10^{-4} s^{-1}$ (Fig. 2). Bulging recrystallisation
644 concentrates along shear bands producing small new grains. After sufficient
645 recrystallisation, strain partitioning and weakening occur while mechanical and
646 microstructural steady state are not achieved. Below the Goetze criterion, generally at
647 higher temperatures and slower strain rates, minor strain weakening occurs, except at
648 1000 °C where steady state is attained (Fig. 2). The associated microstructure is
649 dominated by a pervasive shape foliation of recrystallised grains and the development
650 of a CPO. Hence, mechanical steady state is approached, but not perfectly realised,

651 and this result is consistent with incomplete recrystallisation (Fig. 6), a switch from
652 one deformation mechanism to the next, or simultaneous operation of two
653 mechanisms.

654

655 5.5 Texture and grain size at the brittle-to-viscous transition

656 5.5.1 Misorientation density

657 So as to distinguish recrystallised grains from potential survivor grains of the
658 original quartz material on the basis of some intragranular misorientation density, the
659 grain kernel average misorientation (gKAM) and the grain orientation spread
660 normalised with respect to the long axis (GOS_{la}) were measured. We initially assumed
661 that low intragranular misorientation densities are characteristic of newly
662 recrystallised, recovered grains, whereas high misorientation densities are typical for
663 the original crushed material. However, it was found that recrystallising grains
664 continue to accumulate intragranular strain as the overall shear deformation continues.
665 Accordingly, the gKAM remains high and rather reflects grain-scale strain (*Kilian and*
666 *Heilbronner, 2017*). A correlation of high gKAM with small (recrystallized) grain size
667 has also been noted (*Heilbronner and Kilian, 2017*). In other words, the gKAM, or
668 any other measure of internal misorientation density, does not reflect recovery, and
669 therefore cannot be used to distinguish recrystallized grains from relict grains.

670 However, gKAM and GOS_{la} do vary as a function of temperature: The higher
671 the deformation temperature, the smaller the intragranular misorientation density (Fig.
672 10). Pre-deformation hot pressing or sieving does not significantly influence this
673 trend. At lower temperatures, large grains with high PARIS factors (more lobate
674 grains) have higher gKAM and GOS_{la} values than the small grains with low PARIS
675 factor (fully convex grains). In other words, large grains tend to have high

676 misorientation densities while small grains display the full spectrum of misorientation
677 density, from fully recovered to highly strained. This distinction becomes
678 progressively smaller with increasing temperature, until, at 1000 °C, all grains,
679 irrespective of shape and size, have very small misorientation densities, i.e., appear
680 fully recovered.

681 5.5.2 CPO of diffusion and dislocation creep

682 To investigate if diffusion creep and dislocation creep are grain-size selective,
683 we consider the textures of the small and the large grain-size fractions separately (Fig.
684 11). Small and large grain-size fractions are delimited by the 3D mode which as a
685 result the number of grains in the smaller and larger fraction differ considerably. Pole
686 figures are therefore weighted by the area of the evaluated grains to avoid artefacts.
687 We also checked by comparing number-weighted pole figures that were calculated for
688 the large grain-size fraction and for the same number of randomly selected small
689 grains. The texture indices and the pole figure maxima of $[c]$, $\langle a \rangle$, and $\langle r \rangle$ pole
690 figures of smaller grains are weaker than those for larger grains. The weaker textures
691 are consistent with diffusion creep mechanisms being active in the smaller grain size
692 fraction.

693 At 700 °C, the weaker texture of the small grains is attributed to processes
694 such as solution precipitation and nucleation. At 800 °C and 900 °C, textures of the
695 small grains are not only weakened but also the c -axis maxima are rotated with
696 respect to those of the large grains. For 800 °C and 900 °C, the rotation is 20° and 10°,
697 respectively, clockwise in the sense of the applied shear, compatible with grain-
698 boundary sliding and a stiff rotation of grains. At 1000 °C, the difference between the
699 pole figures of the smaller and larger grain size fractions is the texture strength, not in
700 the texture type. As the rotation axis of the applied shear is parallel to the (strong) c -

701 axis maximum, a potential rotation is difficult to discern.

702 Comparing the experimental quartz deformation analysed here with results
703 derived from naturally or experimentally deformed quartzites, we find that the CPO
704 evolution of the larger grain-size fraction (Fig. 11) is consistent with observations
705 where high temperature deformation produces a central *c*-axis maximum, whereas low
706 temperature deformation (or small shear strains in experiments) produces peripheral
707 maxima (e.g., *Schmid and Casey*, 1986; *Stipp et al.*, 2002; *Heilbronner and Tullis*,
708 2002, 2006). In terms of the three microstructural regimes identified in nature, the 700
709 °C and the 800 °C experiments would coincide with BLG (bulging), the 900 °C
710 sample with SGR (subgrain rotation) and the 1000°C sample with GBM (grain
711 boundary migration). In a more recent study by *Kilian and Heilbronner* (2017), it was
712 found that the textures of Black Hills quartzite (BHQ) deformed in the dislocation
713 creep regimes 1, 2, and 3, develop from a peripheral *c*-axis maximum towards a
714 central *c*-axis maximum as the result of a transition from dominant nucleation /
715 bulging recrystallisation to dominant subgrain rotation recrystallisation.

716 5.5.3 Grain size distributions in diffusion and dislocation creep

717 In a mixed mode of diffusion creep and dislocation creep, as inferred here
718 from the stress exponents of $n \sim 2$, diffusion creep is expected to be more efficient in
719 small grains while dislocation creep, which is grain-size insensitive, should be more
720 active in larger grains (*Tullis*, 2002). An estimate for the upper grain-size limit of
721 grain-size-sensitive creep is given as $<1 \mu\text{m}$ (*Rutter and Brodie*, 2004a), whereas *Luan*
722 *and Paterson* (1992) estimate the upper size limit to be $\sim 20\mu\text{m}$. The recrystallised
723 grain size measured for our experiments at $T = 800 - 1000 \text{ }^\circ\text{C}$, is well within these
724 limits: Recrystallised grain sizes range from $<1 \mu\text{m}$ up to $25 \mu\text{m}$, with modal values
725 (3D mode) of ~ 4 , ~ 6 and $\sim 10 \mu\text{m}$ for $800 \text{ }^\circ\text{C}$, $900 \text{ }^\circ\text{C}$ and 1000°C , respectively (Fig.

726 9). As was shown, the partitioning of deformation mechanisms into smaller and larger
727 grain size fractions takes place in our samples for grain size below and above these
728 modal values as a threshold. Our threshold values are closer to the transition limit of
729 Luan and Paterson (1992) for dislocation and diffusion creep.

730 Before reaching the hit point, the original fractal grain-size distribution has
731 been modified by grain growth. We can estimate from the analysis of two hot-
732 pressed samples that the very smallest size fraction has been obliterated in a manner
733 described by Keulen et al. (2008) for healed faults. However, we do not know how
734 far grain growth proceeded during pressurization and heating, and what the smallest
735 grain size may be at the start of the experiment. In contrast, when the starting
736 material consists of a grain-size fraction of 7-11 μm (sample 445br), we know that
737 any grain smaller than 7 μm must have formed during deformation, possibly by a
738 process such as bulging recrystallisation, nucleation (*Kilian and Heilbronner, 2017*),
739 or creep cavitation (*Precigout and Stunitz, 2016*). Comparing samples 445br
740 (sieved), 388br (standard) and 419br (hot pressed), we note that the grain sizes and
741 stress do not follow a piezometric relation. Grain sizes (3D modes) of 4.4, 4.1 and
742 4.8 μm were measured for flow stresses of 309, 791 and 1016 MPa, respectively.
743 Rather than decreasing with grain size, stress seems to increase (cf. Fig. 13c). In
744 other words, the piezometric relation does not hold and pure dislocation creep can be
745 excluded, suggesting that a substantial contribution of diffusion creep has to be
746 inferred.

747

748 5.6 Using the Griggs apparatus for the derivation of stress exponents

749 As mentioned above, for dislocation creep in quartz, stress exponents of $n = 3$ -
750 5 are often given in the literature (*Gleason and Tullis, 1995; Luan and Paterson,*

1992, *Hirth et al.*, 2001), despite the fact that lower values were determined experimentally ($n \leq 2.5$) in many cases (e.g., *Jaoul et al.*, 1984; *Kronenberg and Tullis*, 1984; *Paterson and Luan*, 1990; *Rutter and Brodie*, 2004b, see Table 4). For some earlier data acquired with solid-medium apparatus, a large uncertainty is attributed to imprecise stress measurements in the solid-medium deformation apparatus (e.g., *Gleason and Tullis*, 1995). However, a large part of the lack of precision and accuracy of the solid medium apparatus is caused by friction and errors associated with the hit point determination. Strain-rate-stepping experiments should not be affected by this error, because all data within a single experiment is determined with respect to the same hit point, and only a slope is fitted to the data, regardless of the absolute values of stresses. In addition, a recent study indicates good accuracy for stresses derived from Griggs apparatus (*Richter et al.*, 2016). Furthermore, the lack of evidence for partial melting in our samples would be consistent with expected low values for stress exponents as suggested by *Jaoul et al.*, (1984); *Luan and Paterson* (1992).

Stress exponents can only be correlated with deformation processes if steady state conditions are reached. Achieving this state may be especially problematic for regime 1 conditions (*Hirth and Tullis*, 1994). The required high strain conditions are difficult to achieve in coaxial compression experiments. Our shear experiments are deformed to high shear strain (up to $\gamma \sim 5$) where mechanical and microstructural steady state is more or less achieved, at least at high temperatures (800-1000 °C; Fig. 2). Hence, the low stress exponents cannot be explained by incomplete steady state conditions as suggested by *Gleason and Tullis* (1995). In addition, *Gleason and Tullis* (1995) associate low stress exponents with the transition from regime 2 to regime 1 after *Hirth and Tullis* (1992). Such a temperature dependent microstructural change is

776 not observed in our samples used for calculating stress exponents. However, the
777 observed microstructures indicate dislocation creep and diffusion creep between 800
778 °C and 1000 °C. In contrast, dislocation creep was solely inferred in earlier studies
779 (e.g., *Gleason and Tullis, 1995; Jaoul et al., 1984*). These studies used quartzites with
780 narrow grain-size ranges and large average grain sizes where grain-size-sensitive
781 deformation mechanisms are unlikely. The broad grain-size range of our starting
782 material with a pronounced fine-grained fraction enables grain-size-sensitive diffusion
783 creep in addition to grain-size-insensitive dislocation creep resulting in mixed stress
784 exponents.

785

786 5.7 Extrapolation to natural conditions

787 It is important to attempt the extrapolation of experimental results to natural
788 conditions. As a first step, the different mechanical and microstructural criteria should
789 be combined to delineate the BVT. In the present study, sample deformation was
790 classified as viscous, semi-brittle, and transitional on the basis of the microstructural
791 suites and experimental behaviour, where transitional deformation is defined by the
792 presence of many remaining large clasts coexisting with clusters of recrystallised
793 grains, the fabric dominated by shear bands at high shear strain. Deformation
794 microstructures can be plotted for the same strain rate in a differential stress vs.
795 confining pressure diagram at a strain rate of $2.5 \cdot 10^{-5} \text{ s}^{-1}$ (Fig. 14a). The transitional
796 samples all plot above the Goetze criterion, so that the Goetze criterion, as to be
797 expected, marks the upper stress limit of dominantly viscous deformation
798 mechanisms. For high confining pressures (1.5 GPa), the BVT can be well delineated
799 using the microstructures and strain rate - temperature relationships (Fig. 14b),
800 although the Goetze criterion is more difficult to define at low temperatures. Using the

801 broad division boundary (green line) from the experimental data, the BVT can be
802 extrapolated to natural conditions of strain rate and temperature (Fig. 14c). As can be
803 seen, the extrapolation is in fairly good agreement with the well documented BVT
804 data point of *Stipp et al.* (2002a,b) for a strain rate of $\sim 10^{-12} \text{ s}^{-1}$. For the representative
805 natural conditions (280 °C, $P_c = 300 \text{ MPa}$, $\Delta\sigma = 250 \text{ MPa}$), the stresses, which were
806 determined were converted to strain rates using the flow law from *Hirth et al.* (2001)
807 and recalculated for 1.5 GPa confining pressure using the appropriate water fugacity
808 values. The microstructures of the *Stipp et al.* (2002a,b) sample at 280 °C are within
809 the viscous field at stresses just below the brittle conditions, consistent with the
810 Goetze criterion and the extrapolation from this study. If natural conditions of 1.0 GPa
811 confining pressures are used, our corrected results for $P_c = 1 \text{ GPa}$ and the *Stipp et al.*
812 (2002a,b) data are consistent, too (Fig. 14d). For 0.5 GPa confining pressure, our
813 experiments have only one data point, but it is also consistent with the extrapolation
814 derived from the series of experiments at higher pressure (Fig. 14d). Thus, this
815 extrapolation should serve as a guideline to determine the BVT in quartz for a wide
816 range of conditions between experiments and nature. For example, semibrittle
817 microstructures in rocks at elevated temperatures in quartz could be used to infer
818 minimum strain rates.

819 **Insert Figure 14 here**

820 If creep conditions of laboratory data for quartz are to be extrapolated to
821 natural conditions, a power-law behaviour (Eq. 1) is always assumed. Existing and
822 commonly used flow laws assume pure dislocation creep with a relatively high stress
823 exponent, typically $n = 4$ (*Hirth et al.*, 2001; *Paterson and Luan*, 1990). Our flow law
824 parameter of a stress exponent of $n = 1.9$ (Table 4) introduces combined (mixed
825 mode) deformation mechanisms of dislocation and diffusion creep. It should be

826 pointed out that the stress exponent for silica gel in the experiments by *Luan and*
827 *Paterson* (1992) also show a value of $n = 2.3$, the data by *Jaoul et al.*, (1984) show n
828 $= 1.4$ to 2.4 , and *Kronenberg and Tullis* (1984) show $n = 2.5$ for novaculite. Thus,
829 several studies have determined stress exponents of $n \approx 2$, independently from each
830 other. The reason why these stress exponents have been questioned in the past is that
831 either impurities (*Luan and Paterson*, 1992) or melt (*Jaoul et al.*, 1984) may have
832 affected the rheology of the samples. In our case, no melt was detected, and we can
833 demonstrate the effect of smaller and larger grain-size fractions for the activation of
834 different deformation mechanisms. Our value for the activation energy is greater than
835 those of *Hirth et al.* (2001) and *Kronenberg and Tullis* (1984) and less than those of
836 *Rutter and Brodie* (2004) and *Gleason and Tullis* (1995), but the range of values is
837 consistent with previous determinations (Table 4).

838 When our data are extrapolated to low temperatures at natural strain rates, the
839 BVT in terms of temperature, strain rate, and pressure will very much depend on the
840 grain size, where small sizes that are very common at low temperatures will favour the
841 operation of diffusion creep mechanism, which are part of the inferred deformation
842 mechanisms in this study. In nature, the expected deformation process probably is
843 solution precipitation creep. It is an important result of this study that the BVT in
844 quartz is not simply a transition from cracking to crystal-plastic deformation, but,
845 instead, it involves grain-size dependent diffusion-creep processes, too.

846 Cataclasis is a very efficient process to reduce grain size, so that our simulated
847 cataclasite is an appropriate starting material for studying the deformation history
848 dependent transition from cracking to viscous deformation. The results clearly show
849 that cataclasites are very likely candidates for subsequent viscous deformation. This
850 interplay of brittle and viscous deformation processes is particularly applicable to high

851 stress deformation settings such as seismically active deformation zones. Catclasis
852 will provide the fine-grained material, which helps to accommodate aseismic creep in
853 interseismic periods, i.e., postseismic creep deformation.

854

855 6. Conclusions

856 A set of shear experiments performed on quartz material under elevated
857 confining pressures (predominantly 1.5 GPa) and temperatures (500 °C - 1000 °C) at
858 intermediate to fast shear strain rates ($3.5 \cdot 10^{-6} \text{ s}^{-1}$ to $\sim 2 \cdot 10^{-3} \text{ s}^{-1}$) documents the
859 transition from (semi)-brittle to viscous deformation. The Goetze criterion ($\Delta\sigma > P_c$) is
860 confirmed to delineate the upper limit of differential stress for viscous deformation.

861 Samples above the Goetze criterion are characterised by Riedel fractures or
862 shear bands at high shear strain, normal geological friction coefficients, and n -values
863 too high for dislocation creep. At low temperatures, increasing confining pressure
864 causes increasing strength, as is to be expected for fracturing and frictional
865 deformation. A somewhat unsystematic temperature-dependence of stress is observed
866 under these conditions. Cataclastic flow partly accompanied by stress-induced
867 dissolution precipitation is suggested as the dominating deformation process at
868 temperatures just below the transition to viscous deformation (650°C) for a strain rate
869 of $2.5 \times 10^{-5} \text{ s}^{-1}$, indicated by a power-law breakdown with a stress exponent of $n = 6.4$
870 ± 1.3 .

871 Below the Goetze criterion ($\Delta\sigma < P_c$), viscous deformation dominates, as
872 demonstrated by weakening of samples with increasing pressure and temperature. The
873 microstructure is dominated by a pervasive foliation at high shear strain accompanied
874 by an increasing recrystallised grain size with increasing temperature, only partially
875 dependent on flow stress. Presence of different CPO's in different grain-size fractions

876 and the stress exponents ($n = 1.9 \pm 0.6$) indicate a combination of diffusion creep and
877 dislocation creep. It is argued that diffusive mass transfer and grain-boundary-sliding
878 prefer the small grain-size fraction while dislocation creep is more effective in large
879 grains. The constant stress exponent between 800 °C and 1000 °C suggests no change
880 in the rate-limiting factor and a similar activation energy for the diffusion and
881 dislocation creep mechanism.

882 From these results, it can be inferred that the brittle to viscous transition with
883 increasing temperature in nature may occur as a combination of diffusion and
884 dislocation creep. The combination favours the viscous deformation to occur in fine
885 grained aggregates likely to have formed by previous cataclastic deformation. Such a
886 sequential transition in time elegantly explains the alternation of episodic seismic
887 (brittle) and aseismic deformation in high stress, seismically active zones.

888

889 Acknowledgments

890 We would like to thank Rüdiger Kilian for extensive stimulating discussions
891 and help with the MTEX toolbox. Furthermore, we wish to thank Willy Tschudin for
892 preparing excellent thin sections, Hans-Rudolf Rüegg for supplying equipment in the
893 deformation lab, Trine Merete Dahl for preparing thin sections for EBSD, and the
894 team of the Nano Imaging Lab and Tom Ivar Eilertsen for support with the SEM. Raw
895 data and samples can be acquired at the corresponding author. Constructive and
896 insightful reviews of 2 anonymous reviewers and Raphael Gottardi and the very
897 constructive input by the editor William Dunne have substantially improved the
898 manuscript. Funding by the Swiss National Science Foundation grant no. 200021-
899 138216 is thankfully acknowledged.

900

- 901 References
- 902 Barber, D. J., Wenk, H.-R., Hirth, G., Kohlstedt, D. L. (2010) Dislocations in
903 minerals In: Hirth, J. P., Kubin, L. (Ed.) Dislocation in solids, Elsevier, 171-232,
904 doi:10.1016/SI572-4859(09)01604-0
- 905 Bell, R. L., Langdon, T. G. (1967) An investigation of grain-boundary sliding
906 during creep, *Journal of Material Science*, 2, 313-323
- 907 Berthé, D, Choukroune, P., Jegouzo, P. (1979) Orthogneiss, mylonite and non
908 coaxial deformation of granites: the example of the South Armorican Shear Zone,
909 *Journal of Structural Geology*, 1, 31-42
- 910 Blanpied, M. L., Lockner, D. A., Byerlee, J. D., (1995) Frictional slip of
911 granite at hydrothermal conditions, *Journal of Geophysical Research*, 100, 13045-
912 13064
- 913 Brace, W. F., Kohlstedt, D. L. (1980) Limits on lithospheric stress imposed by
914 laboratory experiments, *Journal of Geophysical Research: Solid Earth*, 85, 6248-6252
- 915 Byerlee, J. D. (1968) Brittle-ductile transition in rocks, *Journal of Geophysical*
916 *Research*, 73, 4741-4750
- 917 Byerlee, J. (1978) Friction of Rocks, *Pure and Applied Geophysics*, 116, 615-
918 626, doi:10.1007/BF00876528
- 919 Chester, F M., Higgs, N. G. (1992) Multimechanism friction constitutive
920 model for ultrafine quartz gouge at hypocentral conditions, *Journal of Geophysical*
921 *Research*, 97, 1859-1870
- 922 Cross, A. J., Priop, D. J., Stipp, M., Kidder, S. (2017) The recrystallized grain
923 size piezometer for quartz: An EBSD-based calibration, *Geophysical Research*
924 *Letters*, 44, 6667-6674, doi:10.1002/2017GL073836

- 925 Edington, J. W., Melton, K. N., Cutler, C. P. (1976) Superplasticity, Progress
926 in Material Science, 21, 61-158
- 927 FitzGerald, J. D., Boland, J. N., McLaren, A. C., Ord, A., Hobbs, B. E. (1991)
928 Microstructures in water-weakened single crystals of quartz, Journal of Geophysical
929 Research, 96, 2139-2155
- 930 Farver, J., and Yund, R. (2000) Silicon diffusion in a natural quartz aggregate:
931 constraints on solution-transfer diffusion creep, Tectonophysics, 325, 193-205
- 932 Gilletti, B. J., and Yund, R. A. (1984) Oxygen diffusion in quartz, Journal of
933 Geophysical Research, 89, 4039-4046
- 934 Gleason, G. C., and Tullis, J. (1995) A flow law for dislocation creep of quartz
935 aggregates determined with the molten salt cell, Tectonophysics, 247, 1-23
- 936 Gomez Barreiro, J., Lonardelli, I., Wenk, H. R., Dresen, G., Rybacki, E.,
937 Tomé, C. N. (2007) Preferred orientation of anorthite deformed experimentally in
938 Newtonian creep, Earth and Planetary Science Letters, 264, 188-207
- 939 Handy, M. R. (1989) Deformation regimes and the rheological evolution of
940 fault zones in the lithosphere: the effects of pressure, temperature, grainsize and time,
941 Tectonophysics, 163, 119-152
- 942 Hansen, L. N., Zimmerman, M. E., Kohlstedt, D. L. (2011) Grain boundary
943 sliding in San Carlos olivine: Flow law parameters and crystallographic-preferred
944 orientation, Journal of Geophysical Research, 116, B08201,
945 doi:10.1029/2011JB008220
- 946 Heilbronner, R., and Barrett, S. (2014) Image analysis in earth sciences,
947 Springer Berlin Heidelberg, p. 520

- 948 Heilbronner, R., and Kilian, R. (2017) The grain size(s) of Black Hills
949 Quartzite deformed in the dislocation creep regime, *Solid Earth*,
950 <https://doi.org/10.5194/se-8-1071-2017>
- 951 Heilbronner, R., and Tullis, J. (2002) The effect of static annealing on
952 microstructures and crystallographic preferred orientations of quartzites
953 experimentally deformed in axial compression and shear, Geological Society, London,
954 Special Publications, 200, 191-218, doi:10.1144/GSL.SP.2001.200.01.12
- 955 Heilbronner, R., and Tullis, J. (2006) Evolution of c axis pole figures and grain
956 size during dynamic recrystallization: Results from experimentally sheared quartzite,
957 *Journal of Geophysical Research*, 111, B10202, doi:10.1029/2005JB004194
- 958 Hielscher, R., and Schaeben, H. (2008) A novel pole figure inversion method:
959 specification of the MTEX algorithm, *Journal of Applied Crystallography*, 41, 1024-
960 1037, doi:10.1107/S0021889808030112
- 961 Hirth, G., Teyssier, C., Dunlap, W. J. (2001) An evaluation of quartzite flow
962 laws based on comparisons between experimentally and naturally deformed rocks,
963 *International Journal of Earth Science*, 90, 77-87, doi:10.1007/s005310000152
- 964 Hirth, G., and Tullis, J. (1992), Dislocation creep regimes in quartz aggregates,
965 *Journal of Structural Geology*, 14, 145-159, doi:10.1016/0191-8141(92)90053-Y
- 966 Hirth, G., and Tullis, J. (1994), The brittle-plastic transition in experimentally
967 deformed quartz aggregates, *Journal of Geophysical Research*, 99, 11731-11747,
968 doi:10.1029/93JB02873
- 969 Jaoul, O., Tullis, J., Kronenberg, A. (1984) The effect of varying water
970 contents on the creep behaviour of Heavitree quartzite, *Journal of Geophysical*
971 *Research*, 89, 4298-4312

- 972 Karato, S., Jung, H., Katayama, I., Skemer, P. (2008) Geodynamic significance
973 of seismic anisotropy of the upper mantle: new insights from laboratory studies,
974 *Annu. Rev. Earth Planet. Science*, 36, 59-95,
975 doi:10.1146/annurev.earth.36.031207.124120
- 976 Keulen, N., Stünitz, H., Heilbronner, R. (2008): Healing microstructures of
977 experimental and natural fault gouge. – *J. Geophys. Research*,
978 doi:10.1029/2007JB005039
- 979 Kilian, R., and Heilbronner, R. (2017) Texture analysis of experimentally
980 deformed Black Hills Quartzite, *Solid Earth*, <https://doi.org/10.5194/se-8-1095-2017>
- 981 Kohlstedt, D. L., Evans, B., Mackwell, S. J. (1995) Strength of the lithosphere:
982 Constraints imposed by laboratory experiments, *Journal of Geophysical Research*,
983 100, 17,587-17,602, doi:10.1029/95JB01460
- 984 Kohlstedt, D. L., and Hansen, L. N., (2015) Constitutive equations, rheological
985 behaviour, and viscosity of rocks, In: Schubert, G. (Ed.) *Treatise on geophysics*, 2nd
986 edition, Vol. 2, Oxford: Elsevier, 441-472
- 987 Kronenberg, A. K., and Tullis, J. (1984) Flow Strengths of Quartz Aggregates:
988 Grain Size and Pressure Effects due to Hydrolytic Weakening. *Journal of Geophysical*
989 *Research*, 89, 4281-4297, doi:10.1029/JB089iB06p04281
- 990 Luan, F. C., and Paterson, M. S. (1992) Preparation and deformation of
991 synthetic aggregates of quartz, *Journal of Geophysical Research*, 97, 301-320
- 992 Menegon, L., Pennachioni, G., Heilbronner, R., Pittarello, L. (2008) Evolution
993 of quartz microstructure and *c*-axis crystallographic preferred orientation within
994 ductilely deformed granitoids (Arolla unit, Western Alps), *Journal of Structural*
995 *Geology*, 30, 1332-1347, doi:10.1016/j.jsg.2008.07.007

- 996 Orowan, E. (1940) Problems of plastic gliding, Proceedings of the Physical
997 Society, 52, 8-22
- 998 Panozzo, R., and Hürlimann, H. (1983) A simple method for the
999 discrimination of convex and convex-concave lines, Microscopica Acta, 87, 169-176
- 1000 Paterson, M. S. (1989) The interaction of water with quartz and its influence in
1001 dislocation flow – an overview, In: Karato, S.-I., and Toriumi, M. (Ed.), Rheology of
1002 solids and of the earth, Oxford University Press, Oxford, 107-142
- 1003 Paterson, M. S. (2013) Materials science for structural geology, Springer
1004 Dordrecht Heidelberg New York London, p. 247, doi:10.1007/978-94-007-5545-1
- 1005 Paterson, M. S., and Luan, F. C. (1990) Quartzite rheology under geological
1006 conditions, In: Knipe, R. J., Rutter, E. H. (eds.), Deformation mechanisms, rheology
1007 and tectonics, Geological Society Special Publication, 54, 299-307
- 1008 Paterson, M. S., and Wong, T. (2005) Experimental rock deformation - the
1009 brittle field, Springer Berlin Heidelberg, p. 347, doi:10.1007/b137431
- 1010 Pec, M., Stünitz, H., Heilbronner, R. (2012) Semi-brittle deformation of
1011 granitoid gouges in shear experiments at elevated pressures and temperatures, Journal
1012 of Structural Geology, 33, 200-221, doi:10.1016/j.jsg.2011.09.001
- 1013 Pec, M. (2014), Experimental investigation on the rheology of fault rocks,
1014 dissertation, Basel Universität, Basel
- 1015 Poirier, J.P., and Guillope, M. (1979) Deformation induced recrystallization of
1016 minerals, Bull. De. Mineral. 102, 67-74.
- 1017 Précigout, J., Stünitz, H. (2016): Evidence of phase nucleation during olivine
1018 diffusion creep: A new perspective for mantle strain localization. - Earth and
1019 Planetary Science Letters, 455, p. 94-115, doi.org/10.1016/j.epsl.2016.09.029

- 1020 Richter, B, Stünitz, H., Heilbronner, R. (2016) Stresses and pressures at the
1021 quartz-to-coesite transformation in shear deformation experiments, *Journal of*
1022 *Geophysical Research: Solid Earth*, 121, doi:10.1002/2016JB013084
- 1023 Rutter, E. H., and Brodie, K. H. (2004a) Experimental grain size-sensitive flow
1024 of hot pressed Brazilian quartz aggregates, *Journal of Structural Geology*, 26:11,
1025 2011-2023
- 1026 Rutter, E. H., and Brodie, K. H. (2004b) Experimental intracrystalline plastic
1027 flow in hot pressed synthetic quartzite prepared from Brazilian quartz crystals, *Journal*
1028 *of Structural Geology*, 26, 259-270, doi: 10.1016/S0191-8141(03)00096-8
- 1029 Schmid, S. M., and Casey, M. (1986) Complete fabric analysis of some
1030 commonly observed quartz c-axis patterns, *Geophysical Monographs*, 36, 263-286
- 1031 Schmid, S. M., Panozzo, R., Bauer, S. (1987) Simple shear experiments on
1032 calcite rocks: rheology and microfabric, *Journal of Structural Geology*, 9, 747-778
- 1033 Scholz, C. H. (2007) *The Mechanics of Earthquakes and Faulting*, 2nd edition,
1034 Cambridge University Press, Cambridge, p. 471
- 1035 Sibson, R. H. (1989) Earthquake faulting as a structural process, *Journal of*
1036 *Structural Geology*, 11, 1-14, doi:10.1016/0191-8141(89)90032-1
- 1037 Stipp, M., Stünitz, H., Heilbronner, R., Schmid, S. M. (2002a) Dynamic
1038 recrystallisation of quartz: correlation between natural and experimental conditions,
1039 *Geological Society, London, Special Publications*, 200, 171-190,
1040 doi:10.1144/GSL.SP.2001.200.01.11
- 1041 Stipp, M., Stünitz, H., Heilbronner, R. & Schmid, S. M. (2002b):
1042 *Dynamic Recrystallization of quartz: Correlation between Natural and Experimental*
1043 *Conditions*. In: S. de Meer, M. R. Drury, J. H. P. de Bresser & G. M. Pennock:
1044 *Deformation Mechanisms, Rheology and Tectonics: Current Status and Future*

- 1045 Perspectives. - Geological Society, London, Special Publications 200, 171-190.
- 1046 Stünitz, H., Thust, A., Behrens, H., Kilian, R., Tarantola, A., FitzGerald, J. D.
- 1047 (2017) Water redistribution in experimentally deformed natural milky quartz single
- 1048 crystals – Implications for H₂O-weakening processes, Journal of Geophysical
- 1049 Research: Solid Earth, 122, doi:10.1002/2016JB013533
- 1050 Tarantola, A., Diamond, L. W., Stünitz, H. (2010) Modification of fluid
- 1051 inclusions in quartz by deviatoric stress I: experimentally induced changes in
- 1052 inclusion shapes and microstructures, Contribution to mineralogy and Petrology, 160,
- 1053 825-843, doi:10.1007/s00410-101-0509-z
- 1054 Tarantola, A., Diamond, L. W., Stünitz, H., Thust, A., Pec, M. (2012)
- 1055 Modification of fluid inclusion in quartz by deviatoric stress III: Influence of principal
- 1056 stresses on inclusion density and orientation, Contribution to Mineralogy and
- 1057 Petrology, 164, 537-550, doi:10.1007/s00410-012-0749-1
- 1058 Trepmann C. A., and Stöckhert B. (2003) Quartz microstructures developed
- 1059 during non-steady state plastic flow at rapidly decaying stress and strain rate, Journal
- 1060 of Structural Geology, 25, 2035-2051, doi:10.1016/S0191-8141(03)00073-7
- 1061 Trepmann, C. A., Stöckhert, B. (2013) Short-wavelength undulatory extinction
- 1062 in quartz recording coseismic deformation in the middle crust – an experimental
- 1063 study, Solid Earth, 4, 263-276, doi:10.5194/se-4-263-2013
- 1064 Tullis, J. (2002) Deformation of granitic rocks: Experimental studies and
- 1065 natural examples In: Karato, S.I. and Wenk, H.-R., Plastic deformation of minerals
- 1066 and rocks, Reviews in mineralogy and Geochemistry, 51, 51-95,
- 1067 doi:10.2138/gsrmg.51.1.51

1068 Tullis, J., Shelton, G. L., Yund, R. A. (1979) Pressure dependence of rock
1069 strength: implications for hydrolytic weakening, *Bulletin de Minéralogie*, 102, 110-
1070 114

1071 Tullis, J., and Yund, R.A. (1977) Experimental deformation of dry Westerly
1072 granite, *Journal of Geophysical Research*, 82, 5705–5718

1073 Twiss, R. J., and Moores, E. M. (2007) *Structural geology*, W. H. Freeman and
1074 Company, New York, Second Edition, p. 736

1075 Van Daalen, M., Heilbronner, R., Kunze, K. (1999) Orientation analysis of
1076 localized shear deformation in quartz fibres at the brittle–ductile transition,
1077 *Tectonophysics*, 303, 83-107

1078 Yund, R.A., and Tullis, J. (1991) Compositional changes of minerals
1079 associated with dynamic recrystallisation, *Contributions to Mineralogy and Petrology*,
1080 108, 346–355

1081

1082

1083 Figures and tables

1084 Figure 1: Sample assembly.

1085 (a) Sample (quartz powder) is inserted between 45° pre-cut forcing blocks, in a
1086 jacket surrounded by confining medium (NaCl) and a carbon furnace (after *Richter et*
1087 *al.*, 2016). Displacement in the shear zone is at 45° to the plane of drawing. (b)
1088 Stresses in the sample: F = load applied to upper forcing block, P_c = confining
1089 pressure, σ_n = normal stress, τ = shear stress.

1090

1091 Figure 2: Stress-strain curves for constant shear strain rate experiments.

1092 Confining pressure is 1.5 GPa; horizontal lines mark the Goetze criterion. (a)

1093 Shear experiments at different temperatures; arrow indicates assumed initiation of slip
1094 at sample - forcing block interface. (b) Experiments with different shear strain rates at
1095 650 °C, 800 °C and 900 °C. (c) Experiments with different starting material: crushed
1096 = gouge ($d \leq 100 \mu\text{m}$); hot pr. = gouge ($d \leq 100 \mu\text{m}$), hot pressed before deformation
1097 (20h at 1000°C, 1.5 GPa); sieved = gouge ($7 \leq d \leq 11 \mu\text{m}$); arrow indicates the onset
1098 of forcing block deformation.

1099

1100 Figure 3: Stress-strain curves to demonstrate the influence of confining
1101 pressure at three different temperatures.

1102 Strain rate is $2.5 \cdot 10^{-5} \text{ s}^{-1}$; horizontal lines mark the Goetze criterion for
1103 different confining pressures.

1104

1105 Figure 4: Stress-strain curves for strain rate stepping experiments.

1106 Stress-strain curves for experiments at 650 °C, 800 °C, 900 °C, 1000 °C and
1107 800 °C (hot pressed; dashed line as in Fig. 2) are shown in comparison with constant
1108 shear strain rate experiments (numbers 500br, 499br, 412br, 388br, 337br, 419br) at
1109 same conditions. Confining pressure is 1.5 GPa in all samples; horizontal lines mark
1110 the Goetze criterion. The arrow at 488br (800 °C) points to a failure of the experiment.
1111 The arrow at 482br (900 °C) at very high strain marks the change of sample geometry
1112 due to collision of forcing blocks.

1113

1114 Figure 5: Starting material.

1115 Quartz powder after run-in of the σ_1 piston but before the hit point (pre-
1116 deformation) at 800 °C and 1000 °C. (a) Light micrograph of sample 487br at
1117 $T=800^\circ\text{C}$ and $P_c=1.5 \text{ GPa}$, total time of experiment: 25h. Look-up table in upper right

1118 indicates circular polarisation. (b) SEM/band contrast image of sample 487br. (c)
1119 Light micrograph of sample 417br at $T=1000^{\circ}\text{C}$ and $P_c=1.5\text{ GPa}$, total time of
1120 experiment: 20h. Look-up table in upper right indicates crossed polarisation. (d)
1121 SEM/band contrast image of sample 417br. SEM and light micrographs do not show
1122 the same regions.

1123

1124 Figure 6: Microstructures across the brittle-to-viscous transition.

1125 High strain samples deformed at temperatures between 500°C and 1000°C ,
1126 1.5 GPa and $\sim 10^{-5}\text{ s}^{-1}$. Look-up tables indicate circular polarisation for all
1127 micrographs, except 450br and 435br which are cross polarised; sinistral shear sense
1128 applies to all. Left two columns: experiments using crushed starting material, right
1129 column: experiments with hot pressed starting material. Solid lines (F) indicate
1130 orientation of foliation; dashed lines indicate shear band orientation (SB); dotted lines
1131 mark Riedel surfaces (R and R'), schematic of Riedel geometry in inset lower right.

1132

1133 Figure 7: Dependence of microstructures on confining pressure and strain rate.

1134 Look-up tables indicate circular polarisation or crossed polarisation; sinistral
1135 shear sense applies to all. Solid lines (F) indicate orientation of foliation; dashed lines
1136 indicate shear band orientation (SB); dotted lines mark Riedel surfaces (R).

1137

1138 Figure 8: Brittle structures at high temperature.

1139 Sample (386br) deformed at 800°C , 0.5 GPa and $\sim 10^{-5}\text{ s}^{-1}$. (a) Light
1140 micrograph showing fracturing; look-up tables indicate crossed polarisation; dotted
1141 lines mark Riedel surfaces (R and R'). (b) SEM/BSE micrograph of very fine-grained
1142 material generated by comminution along Riedel fractures.

1143

1144 Figure 9: Grain size distribution of recrystallised grains.

1145 Histograms show volume weighted frequency distributions of the diameter of
1146 volume equivalent spheres (D_{equ}); modal values are indicated. Grain size maps for
1147 samples deformed between 700°C and 1000°C are shown with the same magnification
1148 (see scale) and color coded such that blue to yellow corresponds to $2\mu\text{m} \leq D \leq 9\mu\text{m}$.
1149 (a) Grain size distributions for standard starting material ($d \leq 100 \mu\text{m}$). (b) Special
1150 starting material for comparison: hot pr. = hot pressed before deformation; sieved =
1151 starting material ($7 \leq d \leq 11 \mu\text{m}$).

1152

1153 Figure 10: Internal misorientation density of recrystallised grains.

1154 Two measures for misorientation density at the grain scale are evaluated for
1155 samples deformed at temperatures from 700 °C to 1000 °C; gKAM = grain kernel
1156 average misorientation (*Heilbronner and Kilian, 2017*); GOS_{la} = grain orientation
1157 spread, normalised for long axis (see text); for each data point, the PARIS factor is
1158 colour coded and the symbol size is related to the equivalent diameter.

1159

1160 Figure 11: Textures for different grain size fractions.

1161 Textures are shown for samples with standard starting material (crushed),
1162 deformed at 700 °C to 1000 °C, standard confining pressure of 1.5 GPa, and standard
1163 strain rate of $2.5 \cdot 10^{-5} \text{ s}^{-1}$. For each temperature, $[c]$, $[a]$, and $[r]$ pole figures are shown
1164 for all recrystallised grains in the range of ($d \leq 25 \mu\text{m}$) (top row), for the small grain
1165 size fraction (middle row) and the large grain size fraction (bottom row); the
1166 delimiting grain size is indicated. Contouring interval = 1 m.u.d.; pole figure
1167 maximum in the upper left and pole figure J-index on the lower right of the pole

1168 figure.

1169

1170 Figure 12: Friction coefficients for different experimental conditions.

1171 Friction coefficient is calculated from shear and normal stress on sample: $\mu =$
 1172 τ / σ_n (Figure 1). (a) Different shear strain rates at constant confining pressure of 1.5
 1173 GPa. (b) Different confining pressures at constant shear strain rate of $2.5 \cdot 10^{-5} \text{ s}^{-1}$.

1174

1175 Figure 13: Derivation of stress exponent and activation energy.

1176 (a) At 650 °C, the stress exponent $n \sim 6.4$. For 800 °C -1000 °C, the average of
 1177 the stress exponent is determined: $n = 1.9 \pm 0.6$. (b) From experiments at strain rates of
 1178 10^{-4} s^{-1} and 10^{-5} s^{-1} , the activation energy is derived: $Q \sim 170 \text{ kJ/mol}$. (II) indicates the
 1179 second measurement of stress at a given strain rate in strain rate stepping experiments
 1180 (cf. Table 2). (c) At 800°C, 1.5 GPa and 10^{-5} s^{-1} , and for a stress exponent $n = 1.9$, the
 1181 grain size exponent p is 1.08; $m =$ slope of liner fit. Samples used: 388br = standard
 1182 starting material; 419br = hot pressed at 1000°C; 445br = sieved to ($7 \leq d \leq 11 \mu\text{m}$).

1183

1184 Figure 14: Extrapolation of the brittle-to-viscous transition from the lab to
 1185 nature.

1186 Discrimination of 'brittle', 'transitional' and 'viscous' is based on
 1187 microstructure. (a) Differential stress versus confining pressure for experimental
 1188 samples and one natural samples. (b) Shear strain rate versus temperature for
 1189 experimental samples deformed at constant confining pressure; black numbers = flow
 1190 stress; grey numbers = peak stress; green line traces the brittle-to-viscous transition
 1191 (BVT). (c) Extrapolation of (b) to natural conditions. The transition of a natural
 1192 sample (*Stipp et al. (2002)*) is indicated; water fugacity is considered after *Hirth et al.*,

1193 (2001). (d) Same extrapolation as in (c) using additional data points recalculated for
1194 1.0 GPa (orange) and 0.5 GPa (blue) confining pressure; filled circles - using flow
1195 law after *Hirth et al.*, 2001; open circles - using flow law of this study.

1196

1197

1198 Table 1: Experimental conditions for constant shear strain rate experiments.

1199 1) Pre-treatment: Hot pressed = 20 hours at 1000°C and 1.5-1.6 GPa. Sieved = powder
1200 sieved to grain size fraction ($7 \leq d \leq 11 \mu\text{m}$).

1201 2) Friction coefficient determined at peak stress.

1202

1203 Table 2: Experimental conditions for shear strain rate stepping experiments.

1204 1) Temperature approximate due to technical problem with furnace.

1205 2) Approximate value due to power failure.

1206 3) Sample hot pressed for 20 hours at 1000°C and 1.5-1.6 GPa.

1207 4) Hardening at end of experiment due to contact of forcing blocks.

1208

1209 Table 3: Grain size analysis

1210 1) Arithmetic mean of area equivalent diameters of circles (d_{equ})

1211 2) Median of d_{equ}

1212 3) Root-mean-square of d_{equ}

1213 4) Mode = Mean of Gaussian curve fit to volume weighted histogram of volume
1214 equivalent diameters of spheres (D_{equ})

1215 5) Standard deviation of Gaussian curve fit.

1216 6) Hot pressed (24 h) undeformed sample

1217 7) Hot pressed (20 h) undeformed sample

1218 8) Hot pressed (20 h) at 1000°C and 1.5-1.6 GPa.

1219 9) Powder sieved to grain size fraction ($7 \leq d \leq 11 \mu\text{m}$).

1220

1221 Table 4: Selection of flow law parameters from literature.

1222

ACCEPTED MANUSCRIPT

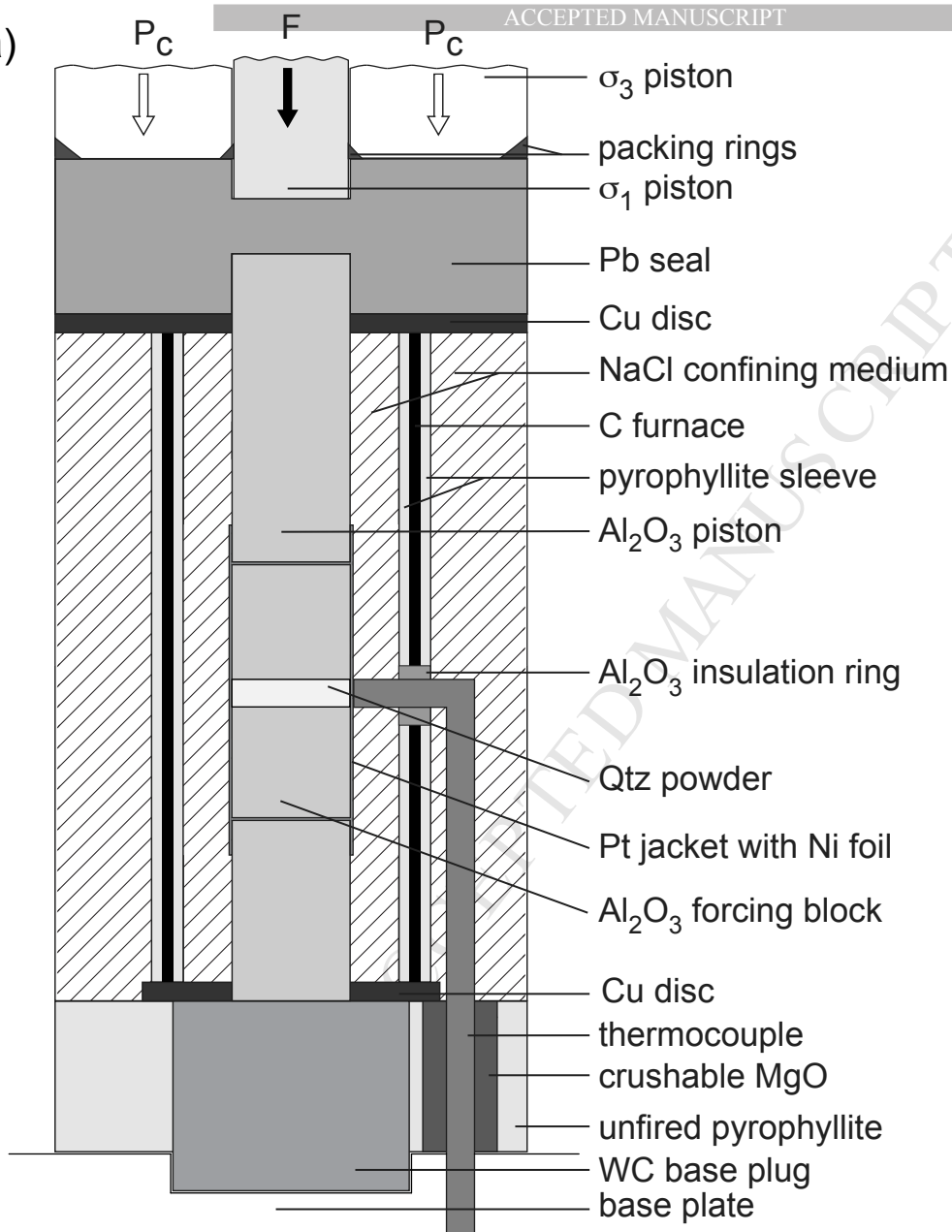
Sample	Temperature (°C)	Confining Pressure (MPa)	Pre- treatment ¹⁾	Shear strain	Shear strain rate (s ⁻¹)	Maximum differential stress (MPa)	Friction coefficient ($\mu = \tau / \sigma_n$) at $\gamma = 3$	Microstructure (for $\gamma > 3$)
340br ²⁾	500	1510		1.6	1.4	2738	0.47	-
450br	500	1540		3.2	2.1	3212	0.46	brittle
338br ²⁾	600	1522		1.4	1.4	2513	0.45	-
479br	600	1538		3.9	2.1	2423	0.43	brittle
415br	600	1512	hot pressed	3.0	1.9	3246	0.51	brittle
435br	650	1507		3.6	2.1	2698	0.46	transitional
481br	650	1554		4.2	3.0	2538	0.43	transitional
380br	700	1500		0.0	0.0	0	0.00	-
339br ²⁾	700	1524		2.0	2.1	1298	0.30	-
437br ²⁾	700	1529		1.7	1.9	1483	0.32	-
383br	700	1585		4.9	2.8	1246	0.25	viscous
493br	700	1512	hot pressed	4.9	2.7	2051	0.39	transitional
487br	800	1511		0.0	0.0	0	0.00	-
439br ²⁾	800	1526		1.4	2.1	856	0.22	-
388br	800	1527		4.8	2.8	858	0.21	viscous
445br	800	1578	sieved	4.7	3.0	415	0.09	viscous
419br	800	1556	hot pressed	4.2	2.8	1159	0.25	viscous
412br	900	1530		2.9	2.8	475	0.10	viscous
417br	1000	1576		0.0	0.0	0	0.00	-
337br	1000	1506		3.2	3.0	152	0.05	viscous
494br	650	1088		5.7	4.8	2396	0.49	transitional
452br	700	1064		4.4	2.7	1536	0.40	transitional
448br	800	1067		4.5	2.9	864	0.25	viscous
386br	800	574		3.2	2.3	1500	0.53	brittle
500br	650	1502		1.1	0.3	1276	0.30	-
447br	800	1556		4.1	27.0	1783	0.35	transitional
499br	900	1535		4.0	189.0	2015	0.39	transitional

Sample	Temperature (°C)	Confining Pressure (MPa)	Shear strain	Stress exponent	Shear strain rate (s ⁻¹)	Flow stress (MPa)	Friction coefficient ($\mu = \tau / \sigma_n$)
498br	650 ¹⁾	1589	5.4	6.4	2.60	2608	0.46
					1.20	2517	0.44
					0.30	1842	0.36
488br	800	1623	6.4	1.8	28.00	1811	0.37
					5.10	783	0.20
					1.20	422	0.11
					0.48 ²⁾	250	0.07
480br ³⁾	800	1601	4.5		2.30	1040	0.25
					0.63	293	0.09
					2.70	820	0.20
482br	900	1583	8.4	2.0	28.00	1272	0.29
					3.60	389	0.11
					0.49	178	0.05
					41.00 ⁴⁾	1494	0.32
485br	1000	1588	6.2	1.8	27.00	578	0.16
					4.00	189	0.06
					0.37	75	0.02
					34.00	794	0.20

Sample	T [°C]	Pc [GPa]	$\dot{\gamma}$ [$10^{-5} \cdot s^{-1}$]	Width [px]	Height [px]	Step size [μm]	No. of grains	2D mean ¹⁾ [μm]	2D median ²⁾ [μm]	2D RMS ³⁾ [μm]	3D mode ⁴⁾ [μm]	3D st.dev. ⁵⁾ [μm]
487br ⁶⁾	800°	1.5	-	700	625	0.20	386	5.21	4.31	6.50	9.1	2.7
417br ⁷⁾	1000°	1.5	-	1250	1649	0.20	583	7.56	6.65	9.21	12.8	4.3
383br	700	1.5	2.8	525	325	0.20	3988	0.98	0.75	1.41	2.1	0.5
388br	800	1.5	2.8	500	500	0.20	1517	2.27	1.86	2.90	4.1	1.9
412br	900	1.5	2.8	925	850	0.20	2789	3.02	2.67	3.79	6.1	0.9
337br	1000	1.5	3	1250	1000	0.20	696	5.80	4.53	7.99	15.3	13.4
493br ⁸⁾	700	1.5	2.7	400	350	0.20	3518	0.93	0.77	1.36	1.6	0.2
419br ⁸⁾	800	1.5	2.8	800	900	0.15	2257	2.34	1.99	3.00	4.8	0.8
445br ⁹⁾	800	1.5	3	1200	700	0.10	2495	1.30	0.78	2.05	4.4	3.7
452br	700	1	2.7	820	600	0.15	9716	0.77	0.63	1.12	1.5	0.2
448br	800	1	2.9	1600	900	0.10	4102	1.49	1.17	2.1	3.3	0.5
447br	800	1.5	27	1000	750	0.20	16390	1.173	1.01	1.51	2.0	0.3
499br	900	1.5	189	708	512	0.20	11521	0.914	0.81	1.22	1.5	0.2

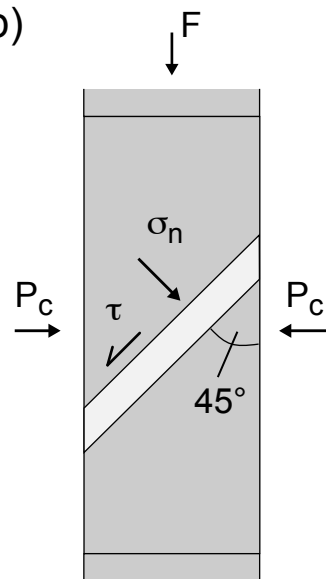
Source	Confining pressure Pc [GPa]	Stress exponent n	Activation energy Q [kJ/mol]	Factor A [MPa ⁻¹ s ⁻¹]	Material	Water content
Jaoul et al. (1984)	1.5	1.4 – 2.4	146 - 172	$2.95 \cdot 10^{-4}$ to $7.68 \cdot 10^{-8}$	Heavitree Quartzite d = 0.2 mm	H ₂ O in different amounts
Kronenberg & Tullis (1984)	0.9 – 1.45	2.9 – 3.2	170 - 220	-	Heavitree Quartzite d = 211 μm	As-is
Kronenberg & Tullis (1984)	1.5	2.5	120 - 150	-	Novaculite d = 4.9 μm	0.4 wt% H ₂ O added
Paterson & Luan (1990)	0.3	2.3	150	-	Silica Gel d = 30 – 80 μm	1000 – 10000 H/106 Si
Paterson & Luan (1990)	0.3	3.9	150	$\sim 4.0 \cdot 10^{-10}$	Silicic Acid d = 20 μm	1000 – 10000 H/106 Si
Gleason & Tullis (1995)	1.5 – 1.7	3.9 – 4.1	137 - 223	$1.1 \cdot 10^{-4}$	Black Hills Quartzite d = 100 μm	0.15 wt% H ₂ O added
Hirth et al. (2001)	-	4	135	$6.3 \cdot 10^{-12}$	Fitted flow law experimental / natural	-
Rutter & Brodie (2004a)	0.3	2.97	224	$1.17 \cdot 10^{-5}$	Synthetic d = 12 - 20 μm	0.6 wt%
Rutter & Brodie (2004b)	0.3	1	220	0.4	Synthetic d = 0.4, 1.3, 4.5 μm	0.6 wt%
This Study	1.5	1.8 - 2.0	168 - 170	$3.1 \cdot 10^{-4}$	Crushed Quartz d < 100 μm	0.2 wt% H ₂ O added

(a)

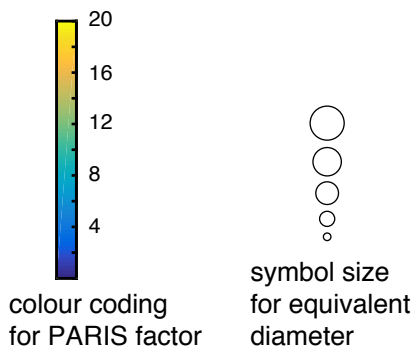
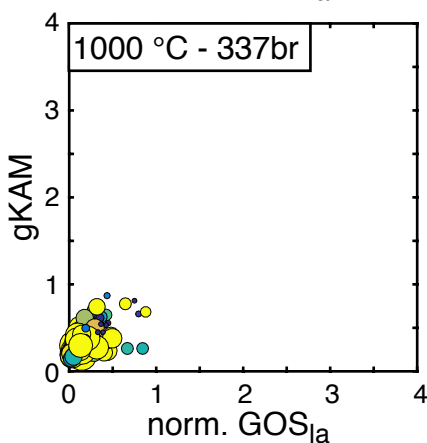
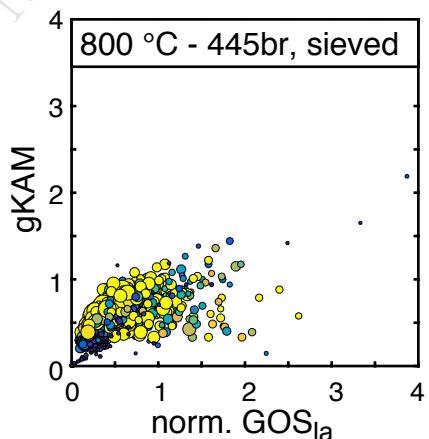
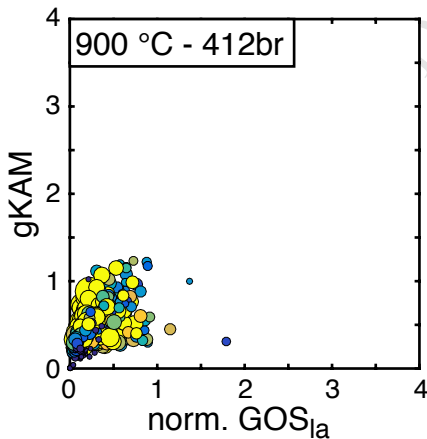
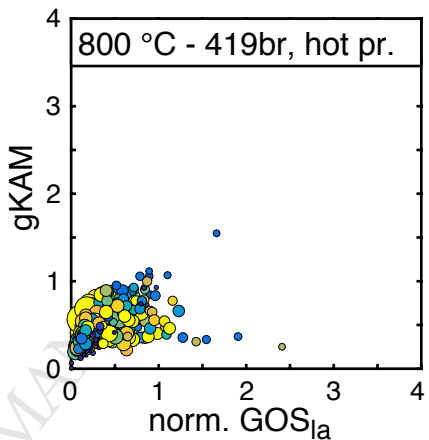
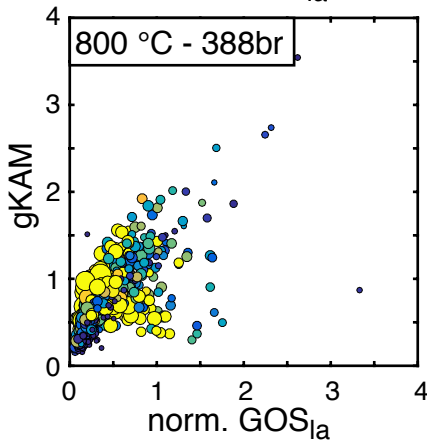
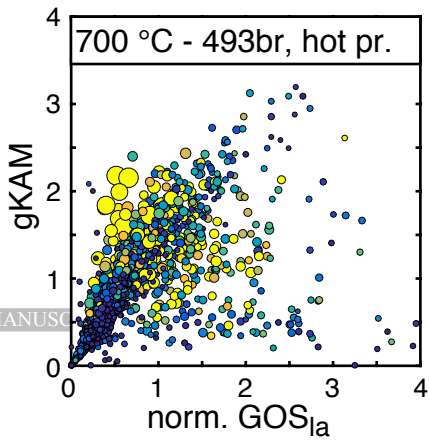
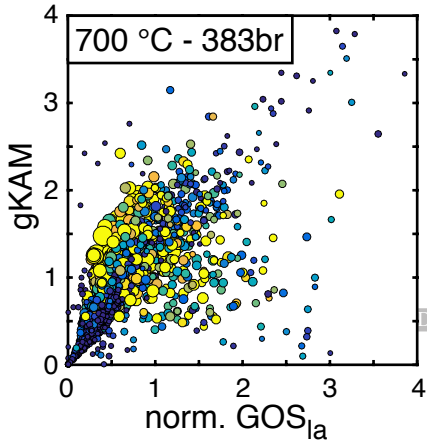


0 5 10 mm

(b)



0 5 mm

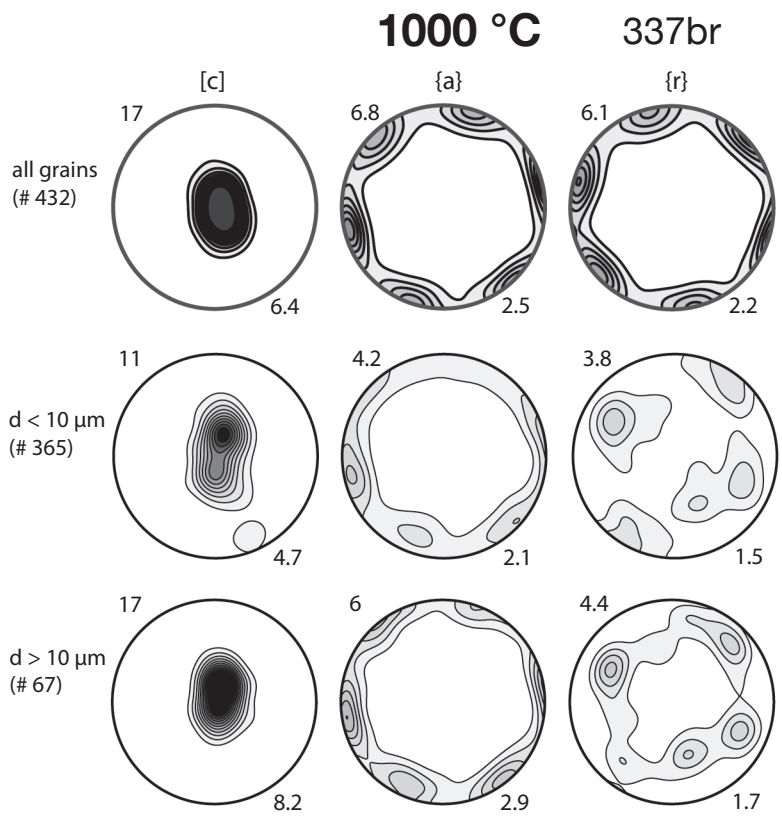
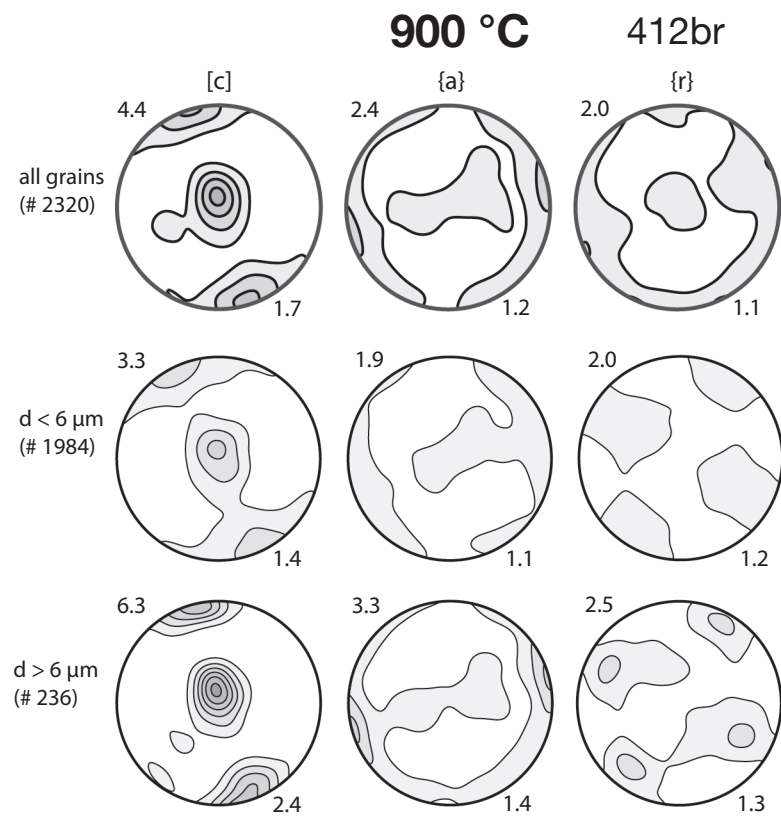
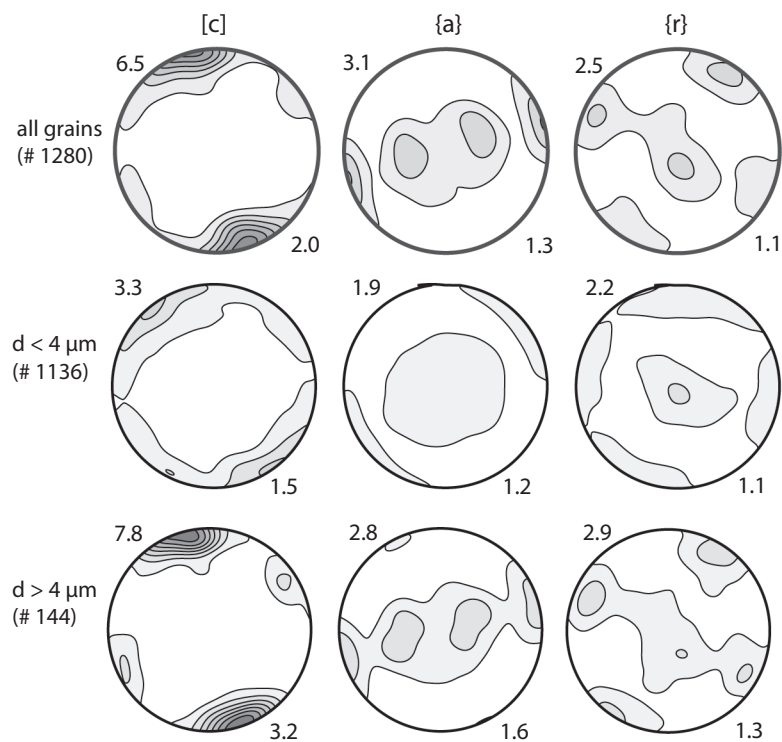
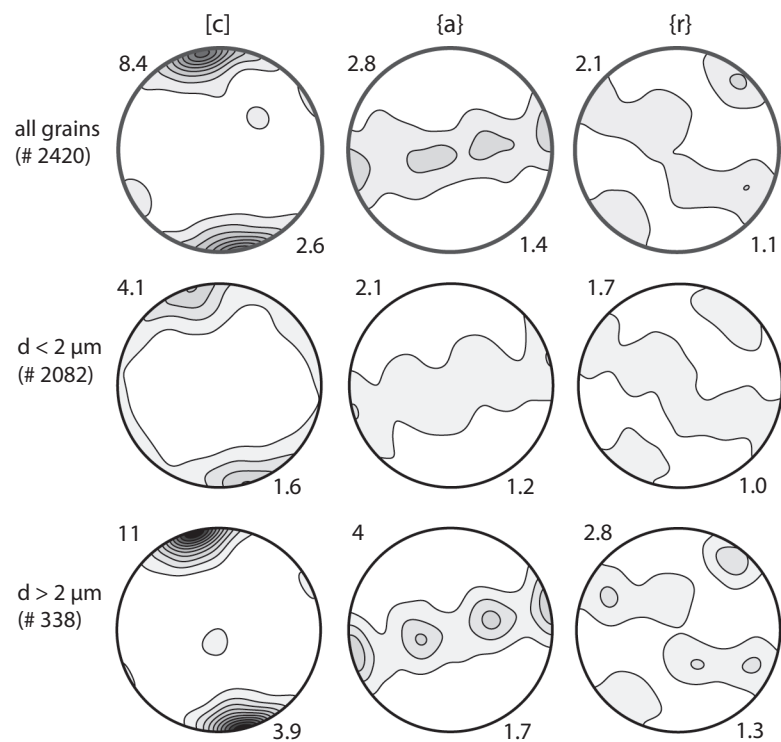


700 °C

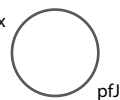
383br

800 °C

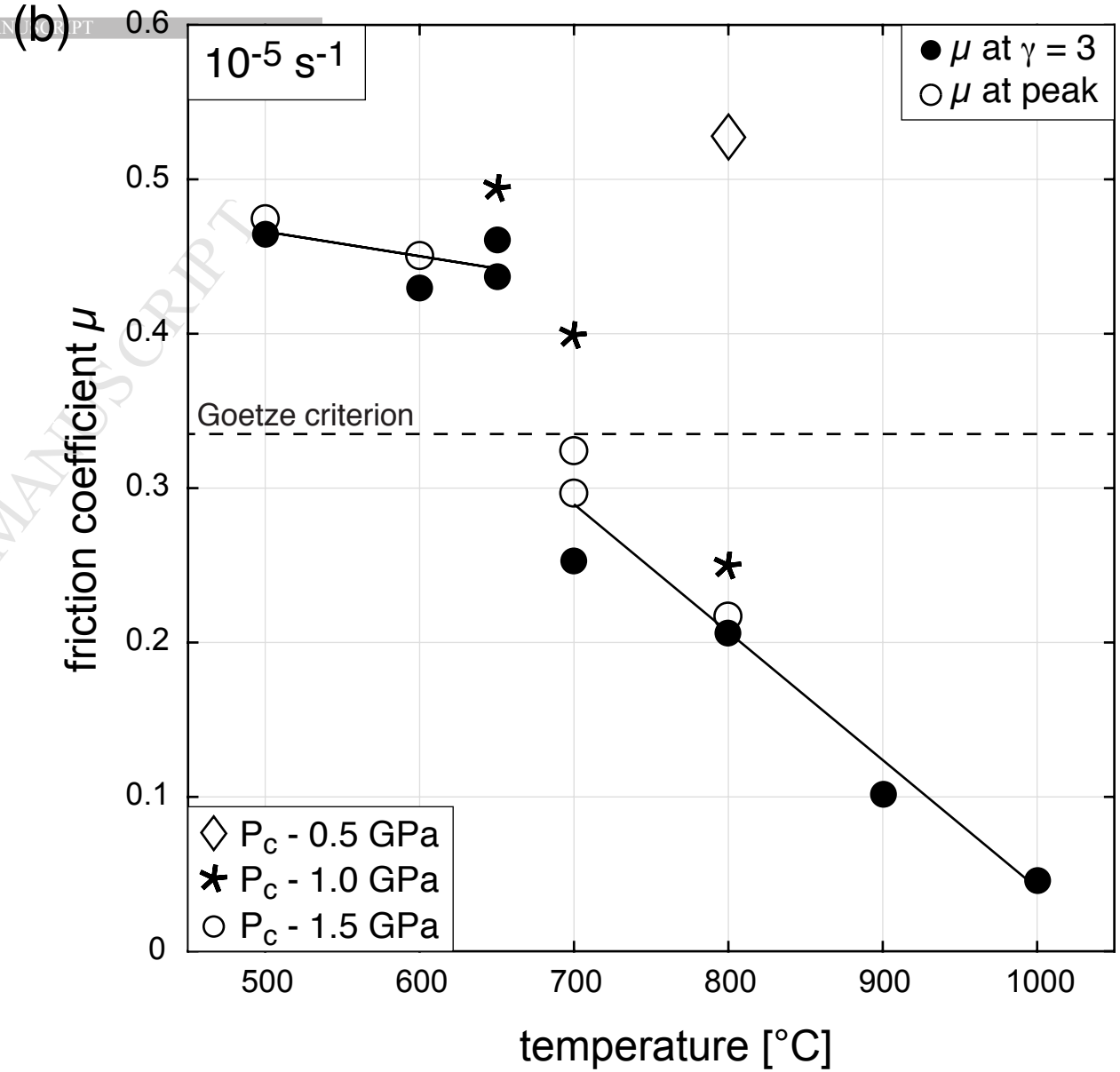
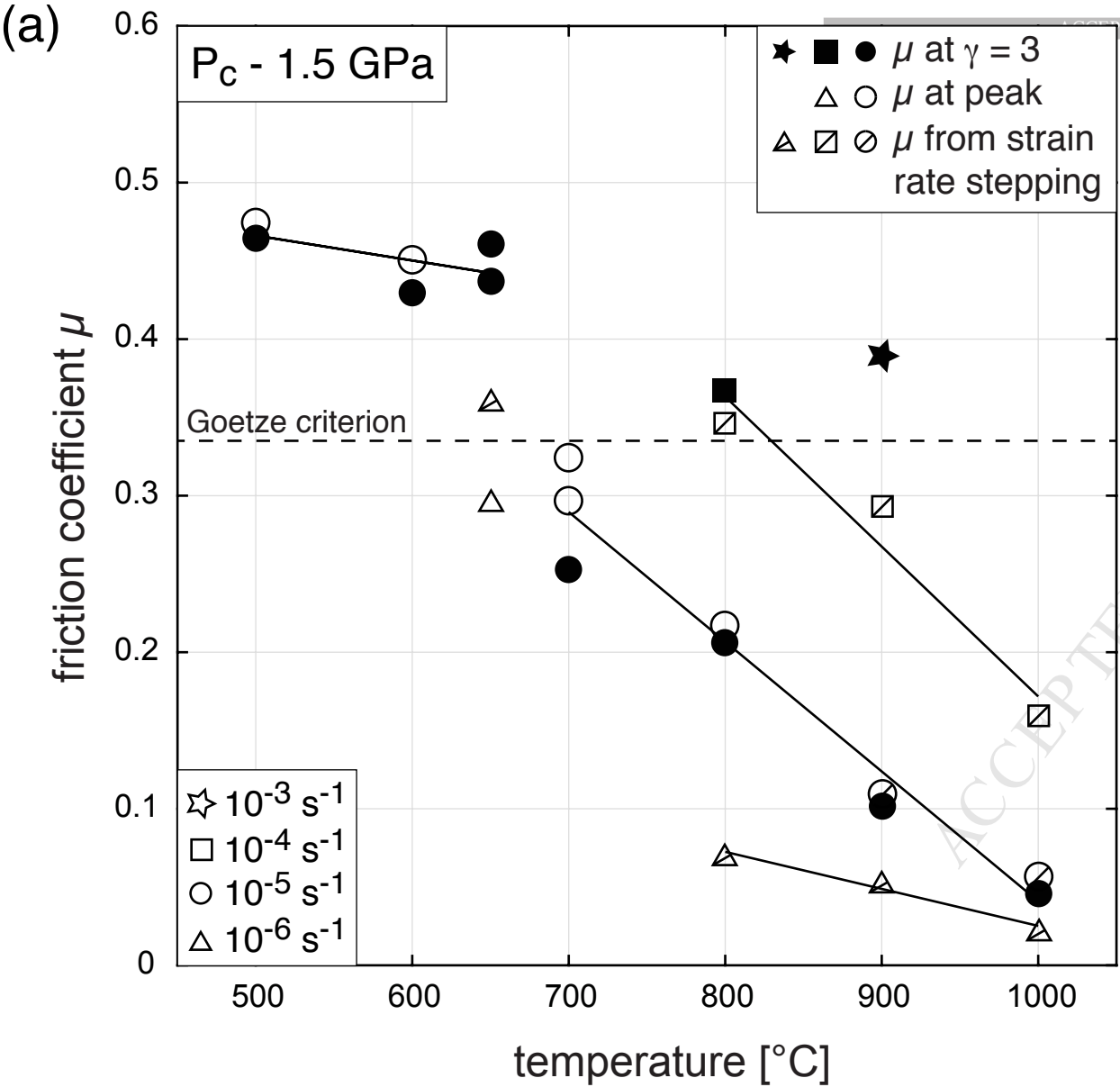
388br



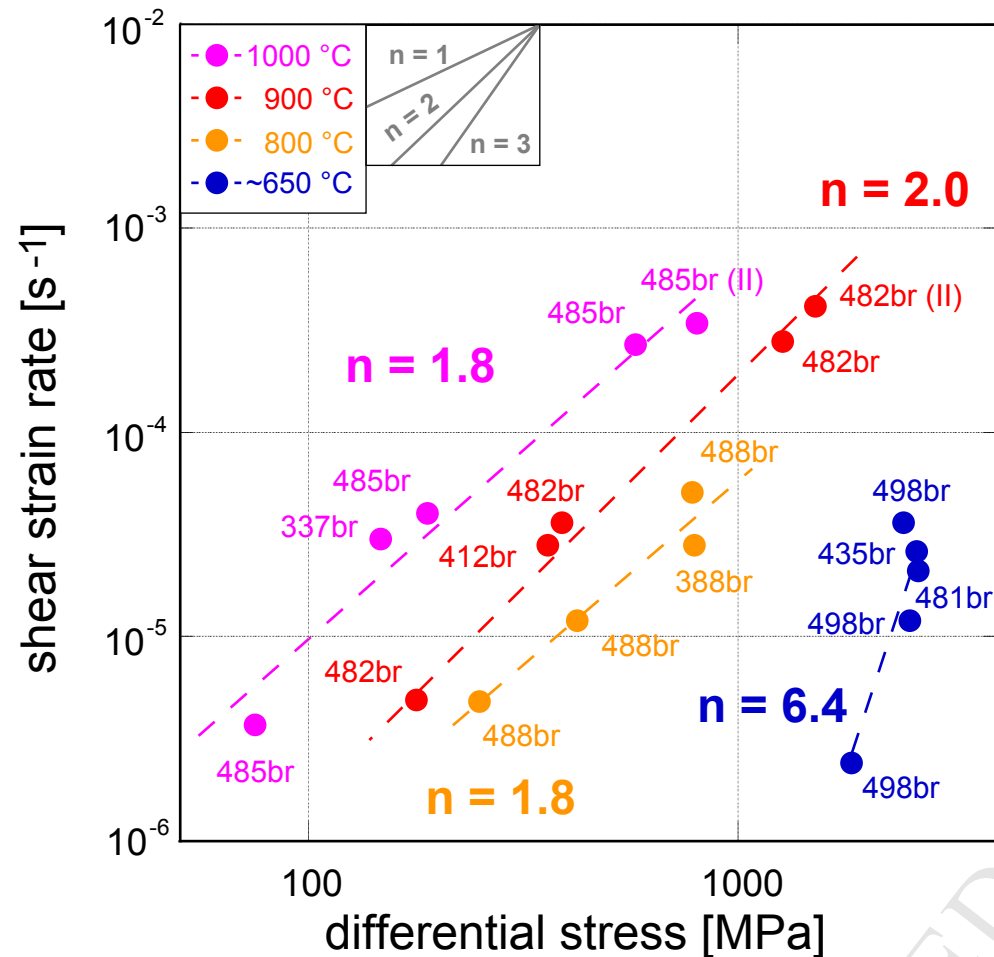
pf max



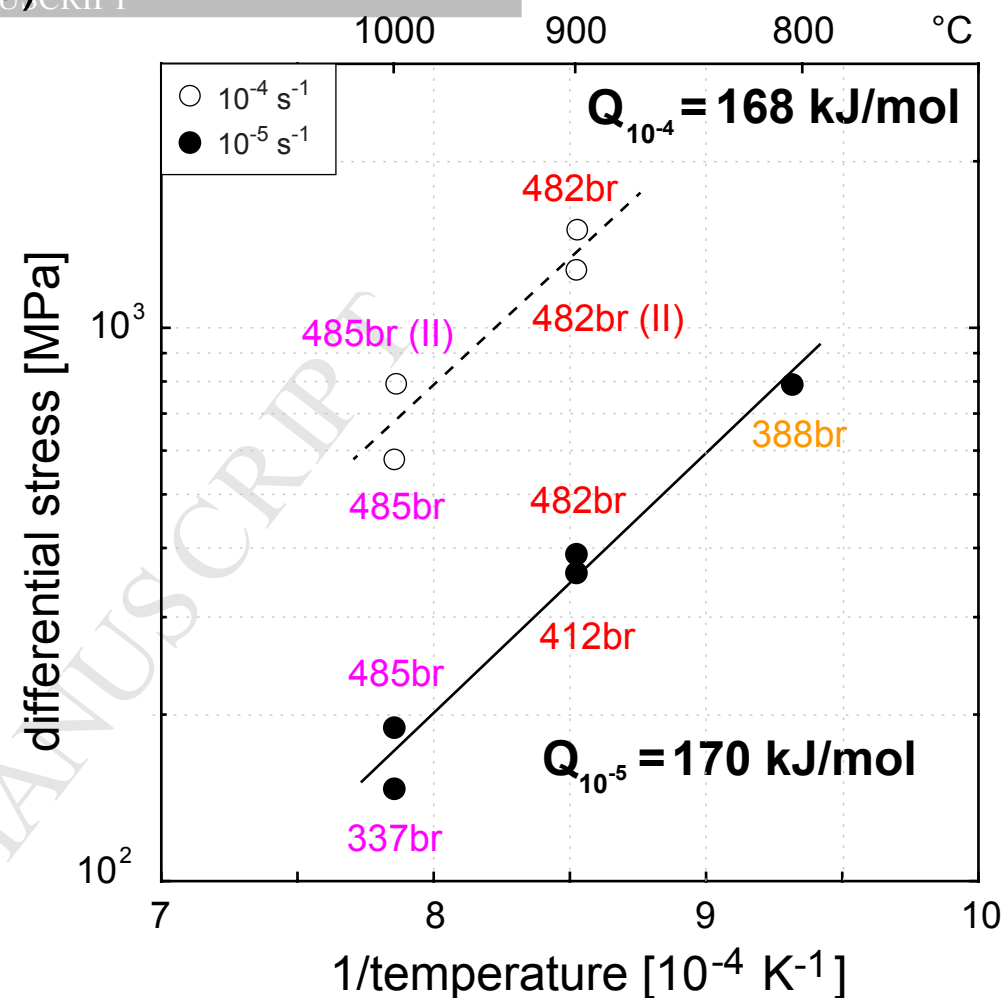
0 2 4 6 8 10



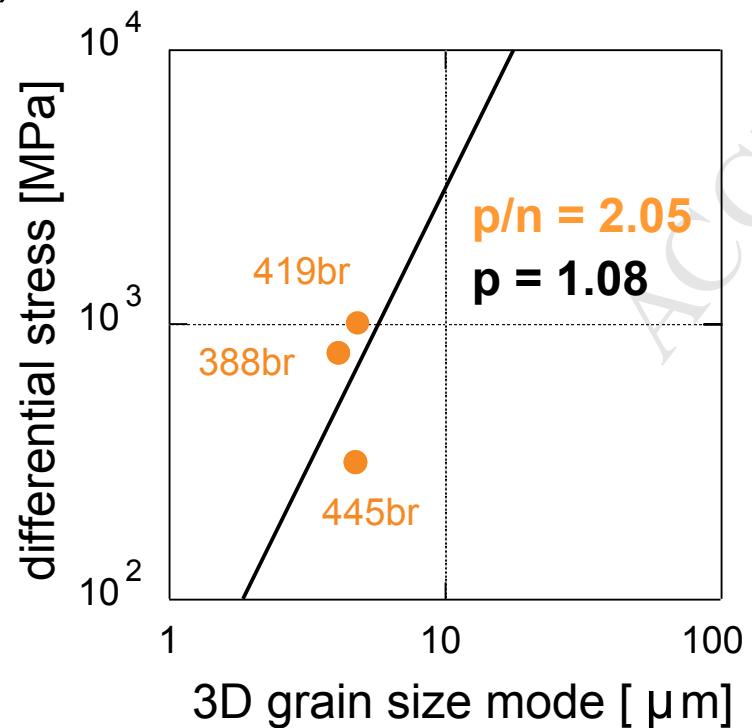
(a)

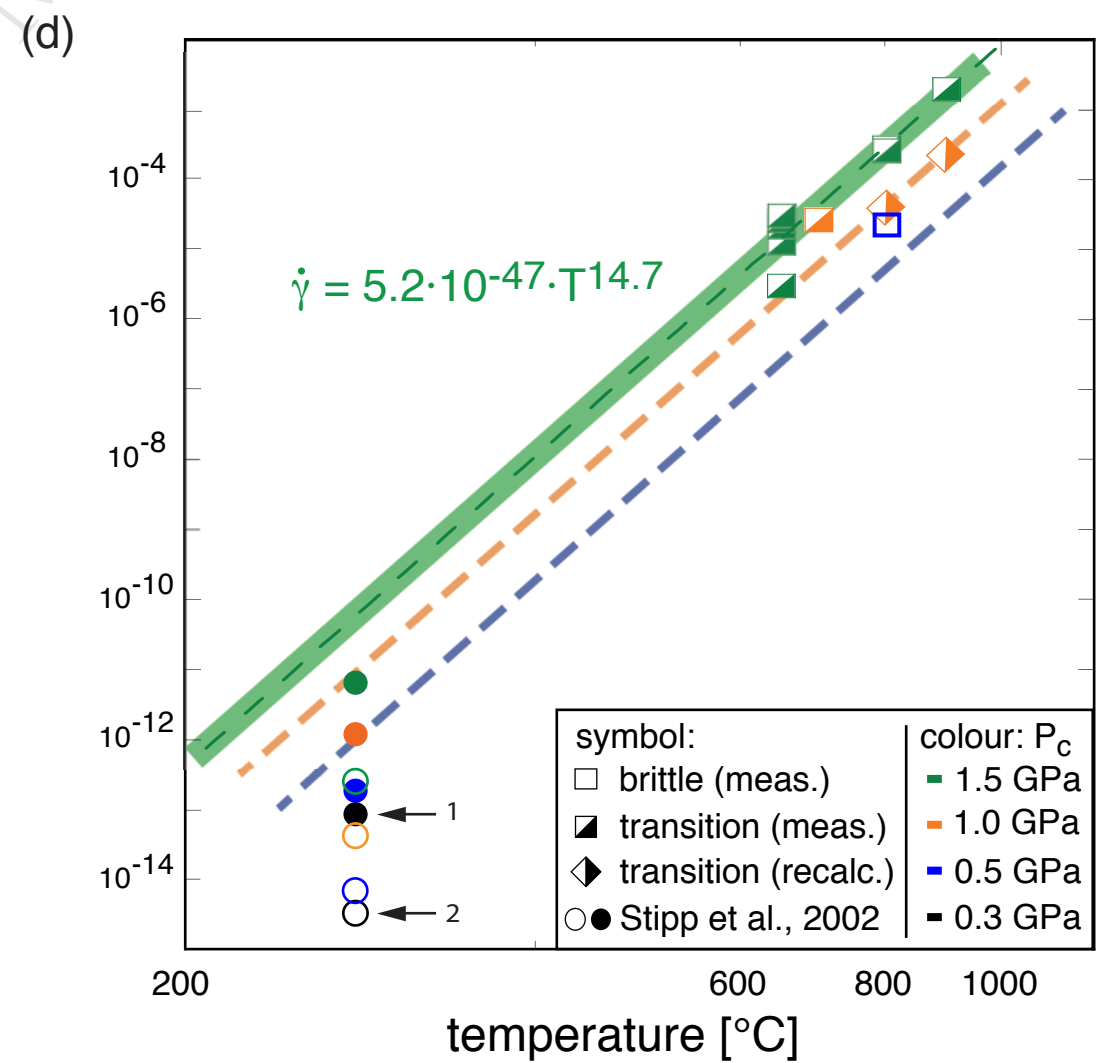
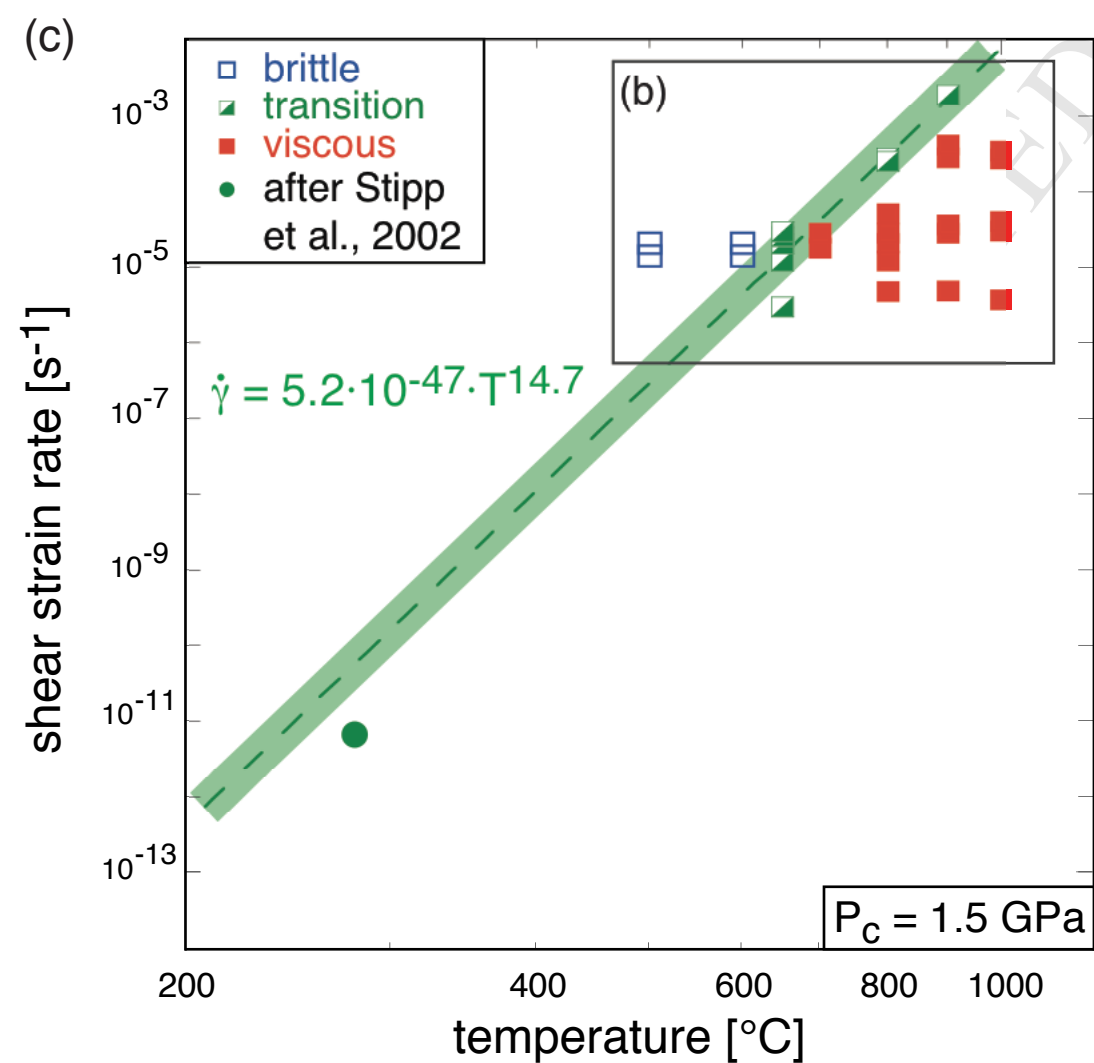
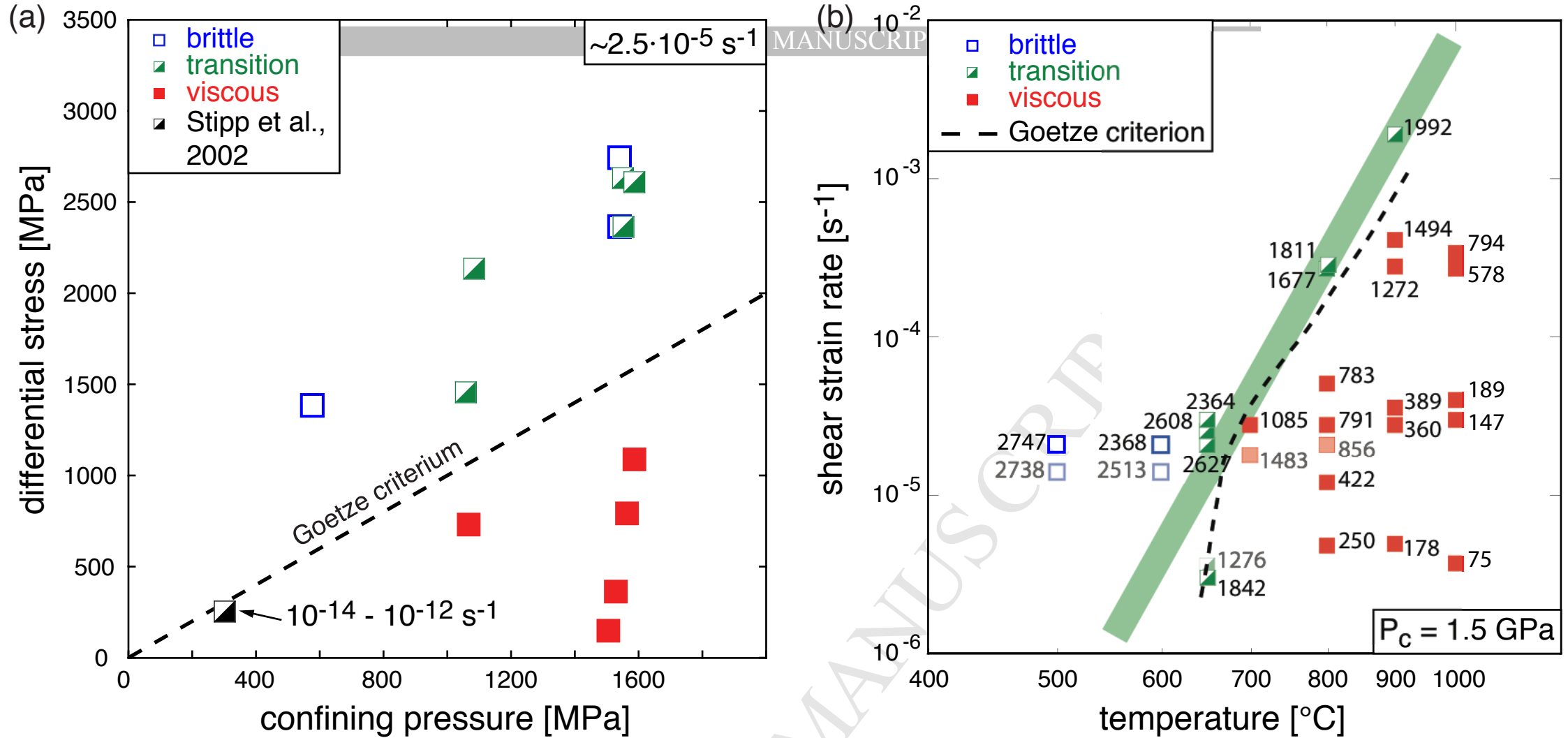


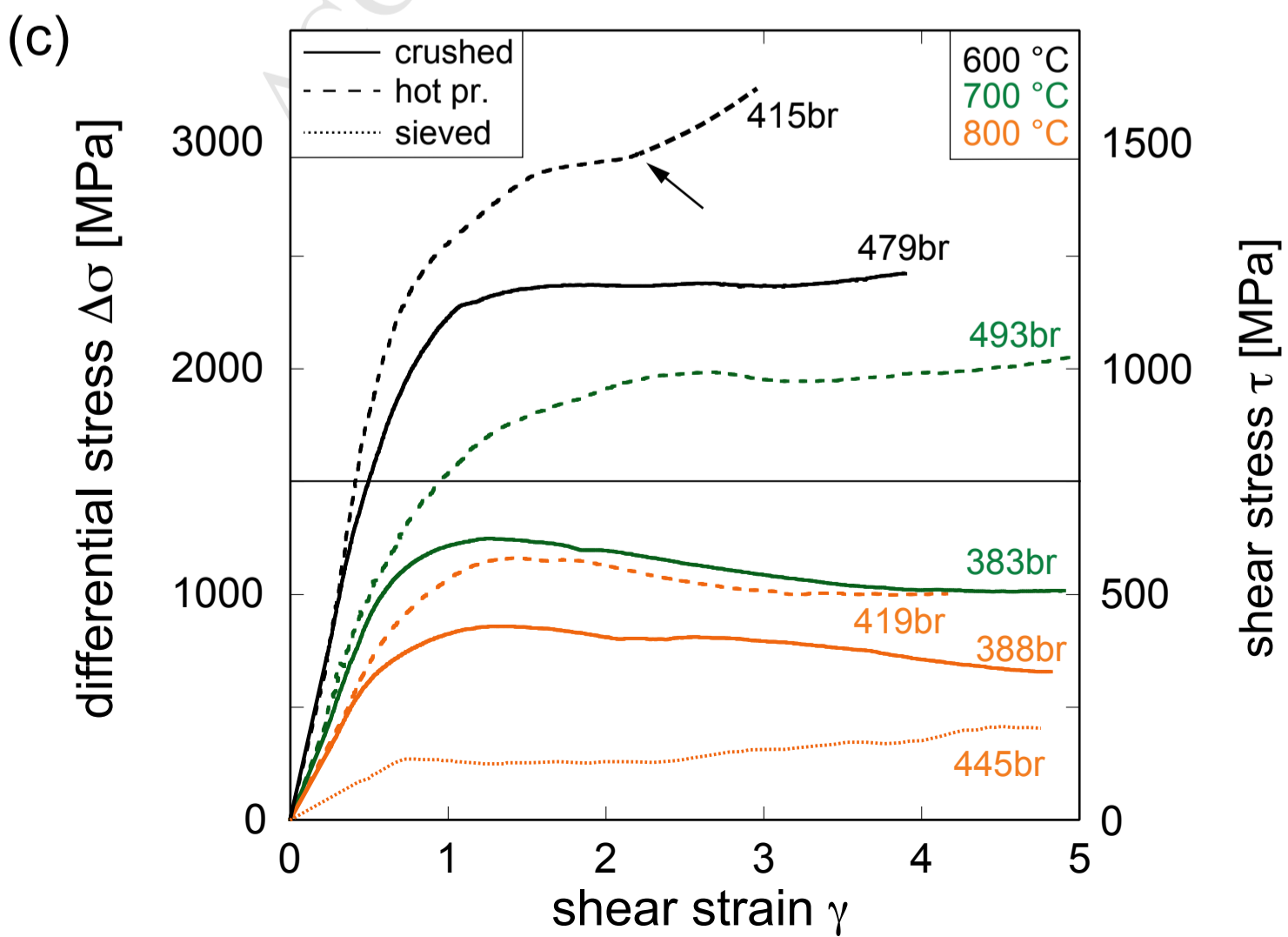
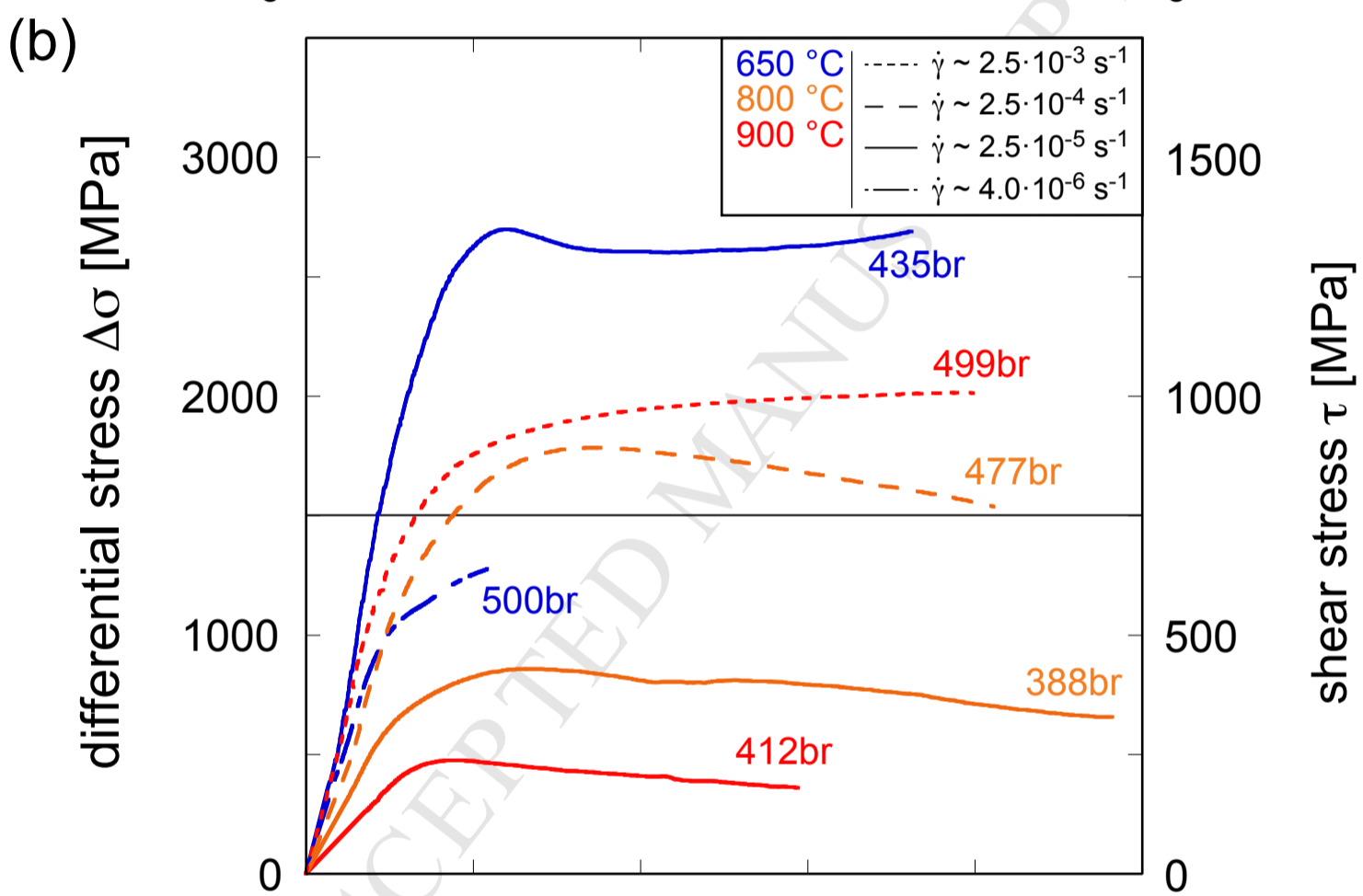
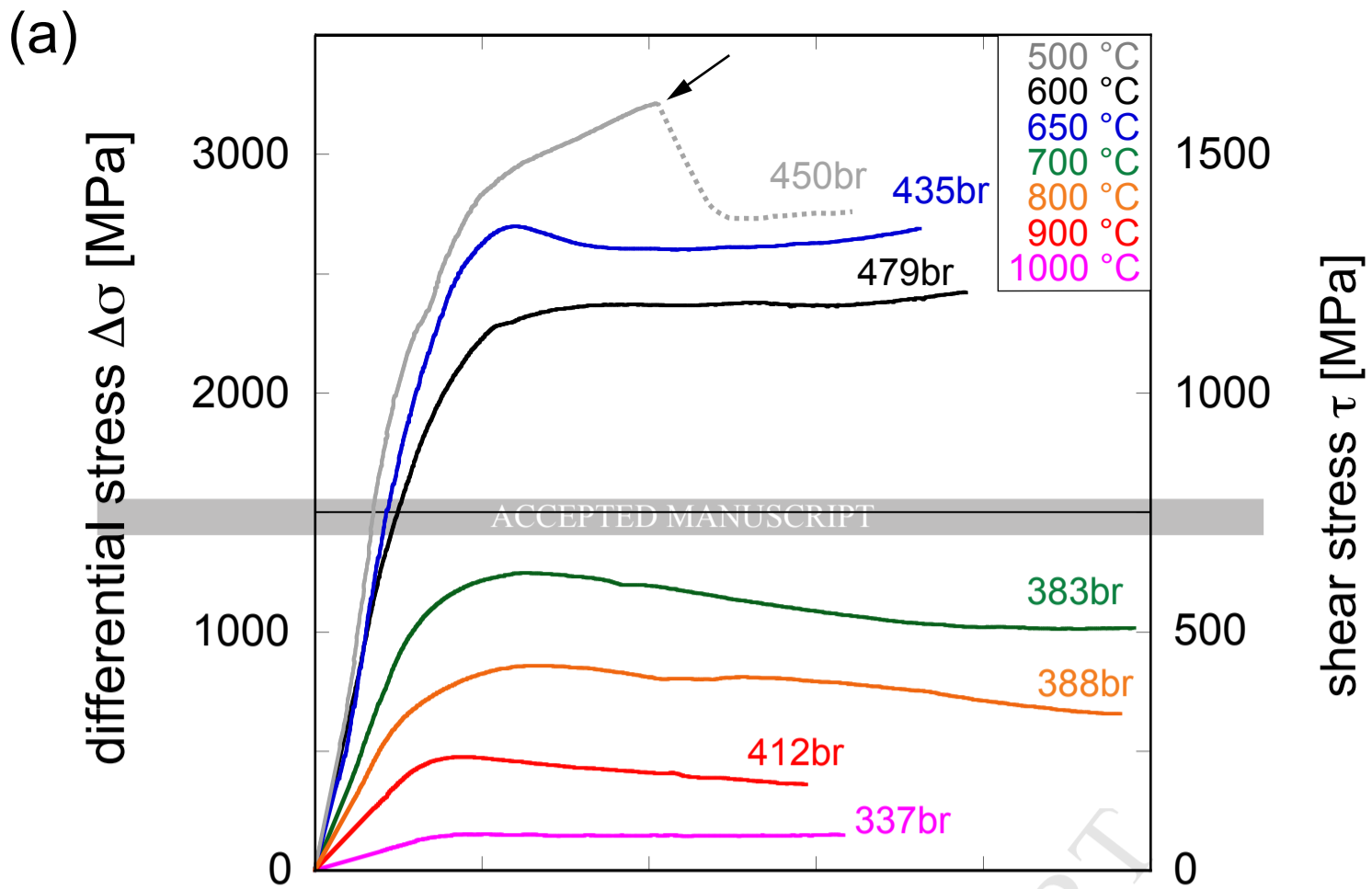
(b)

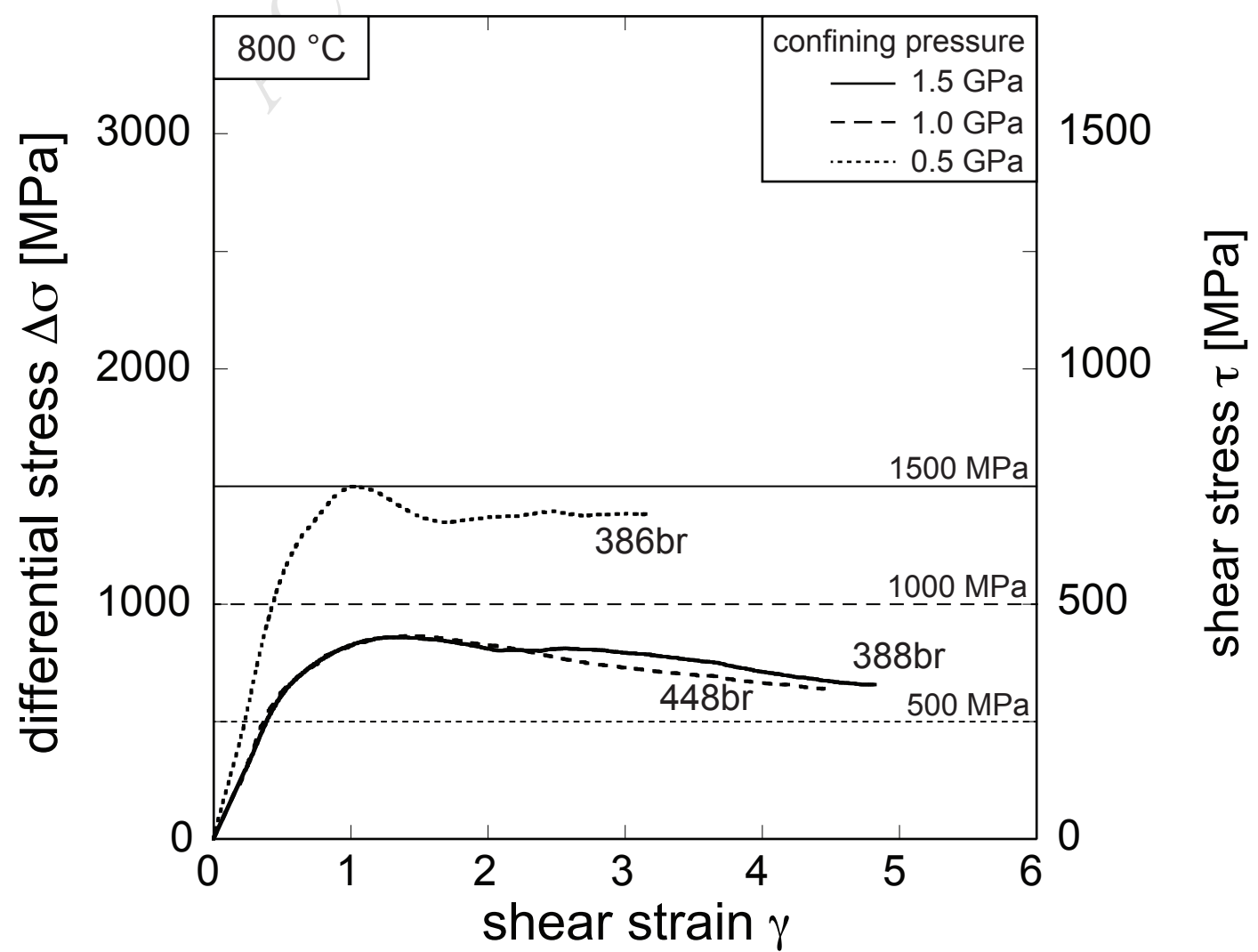
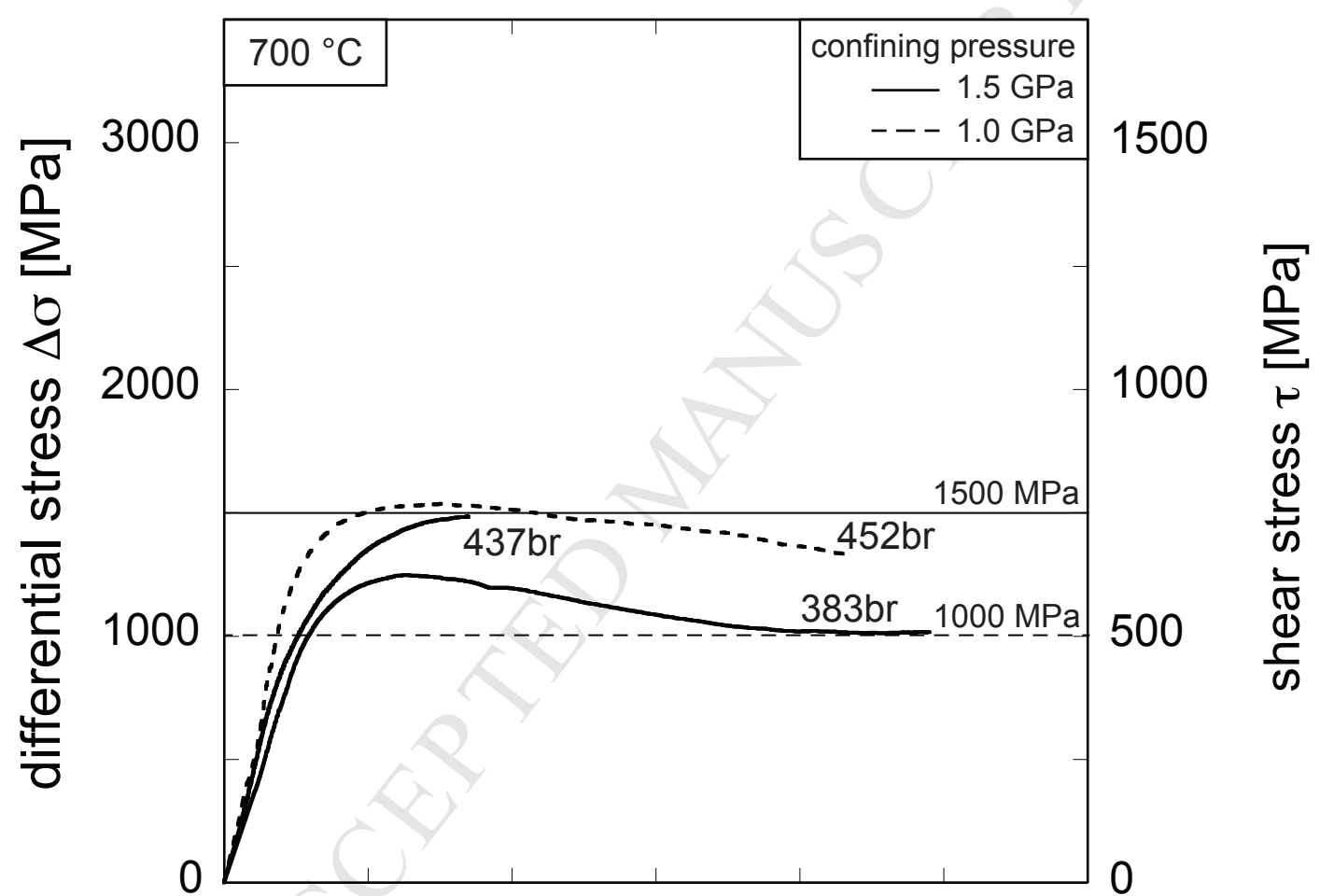
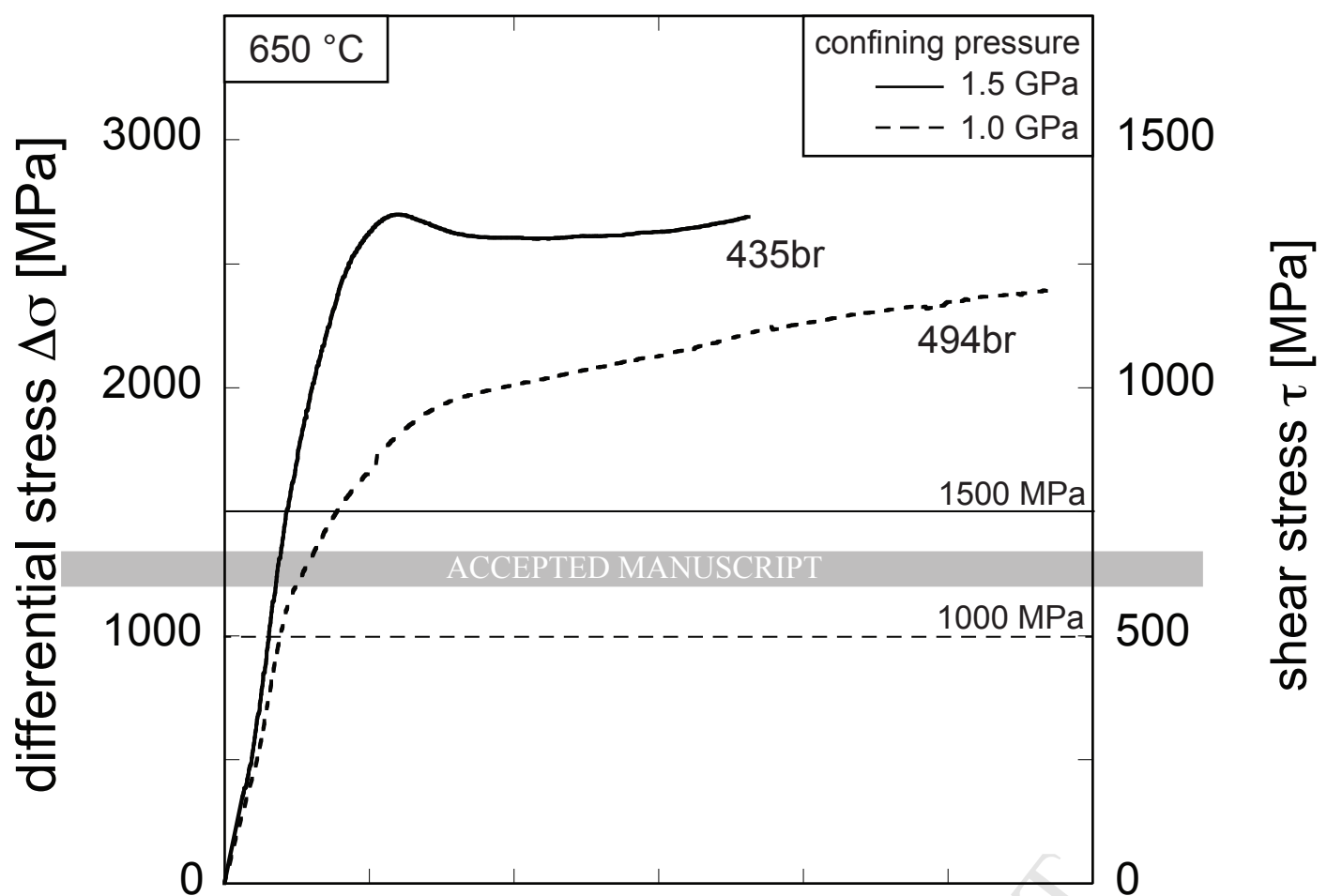


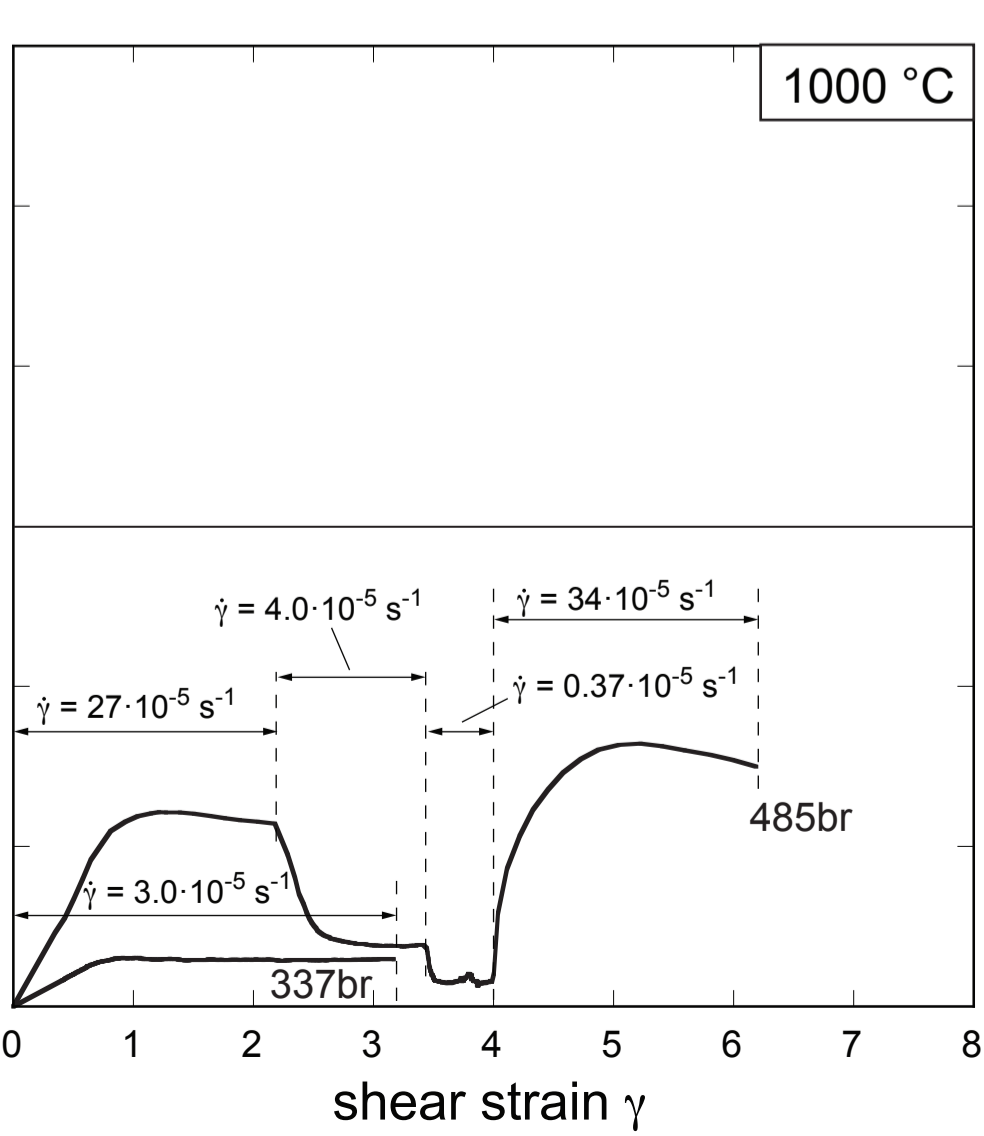
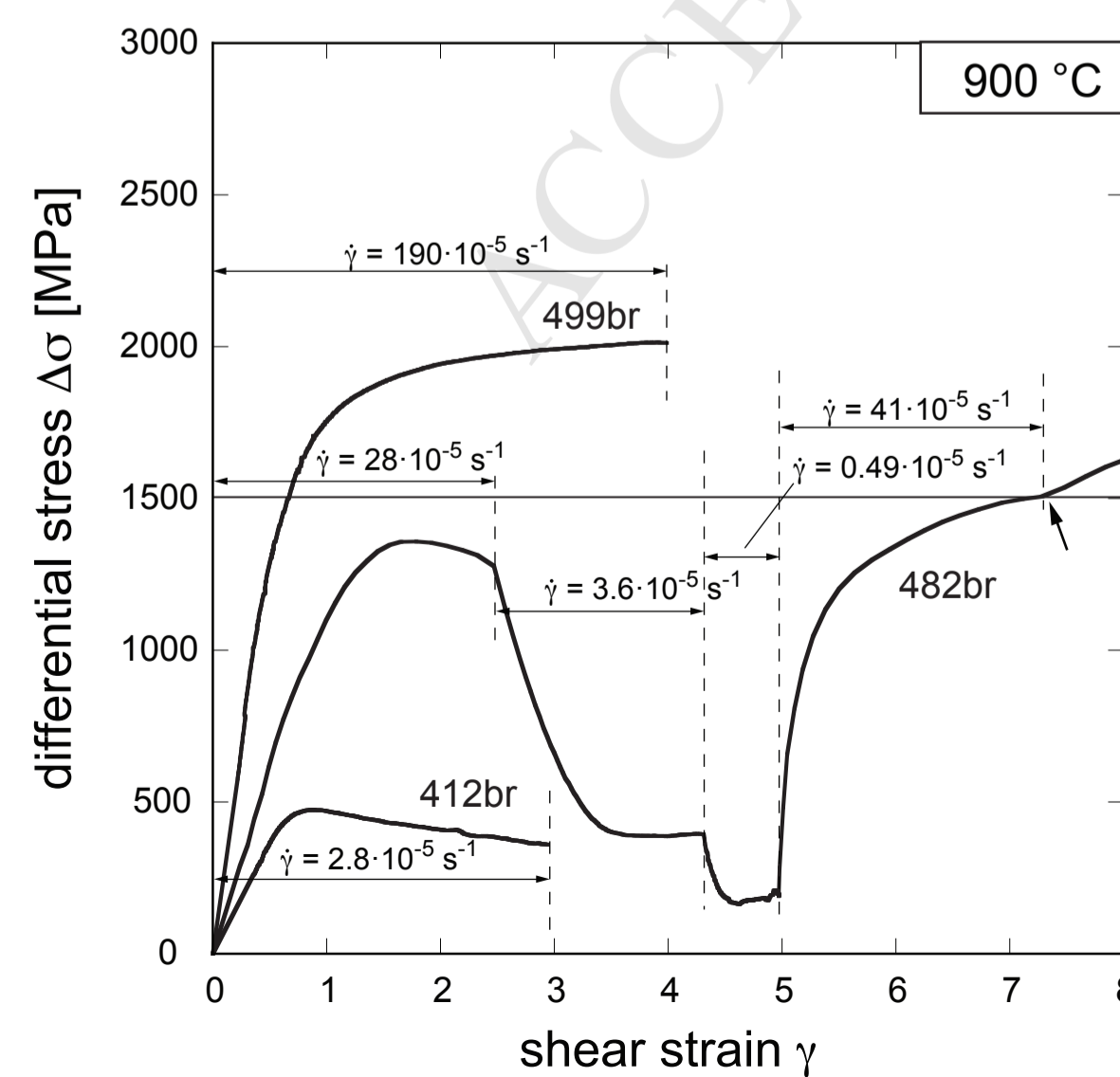
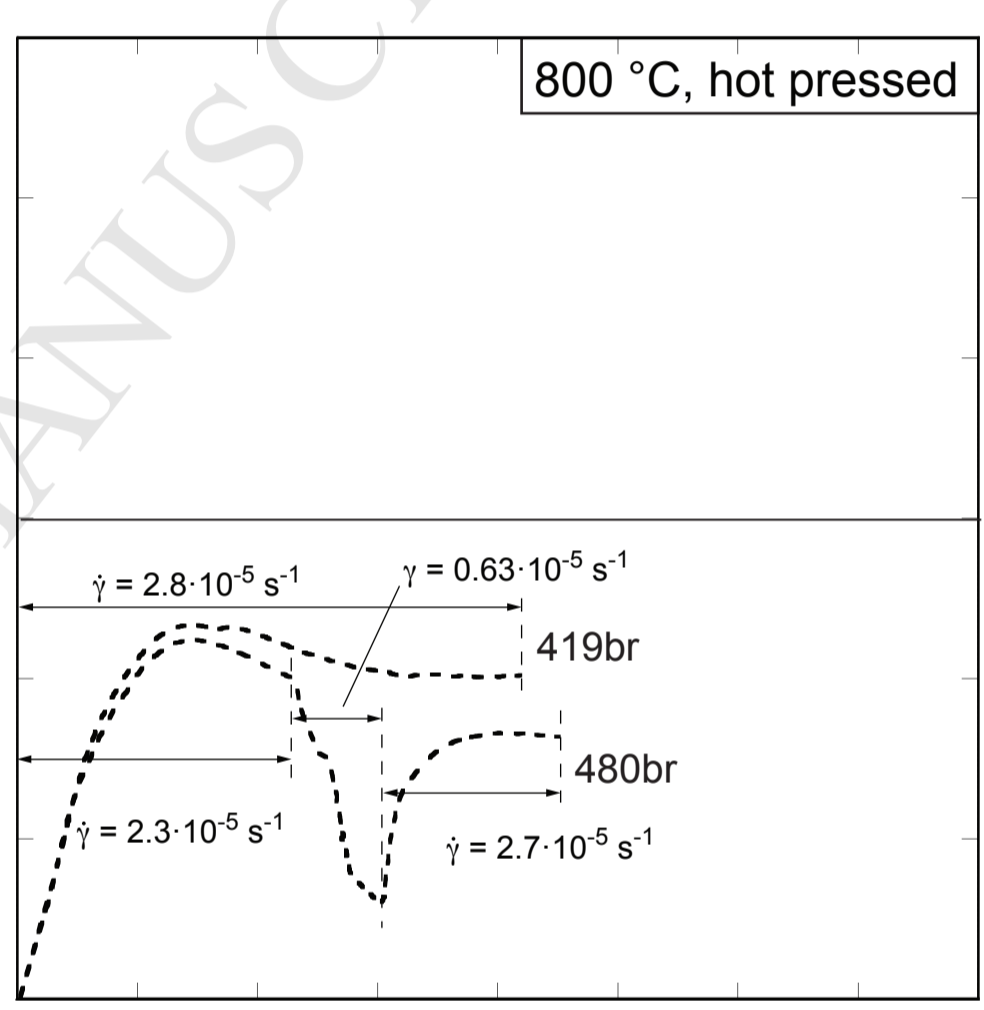
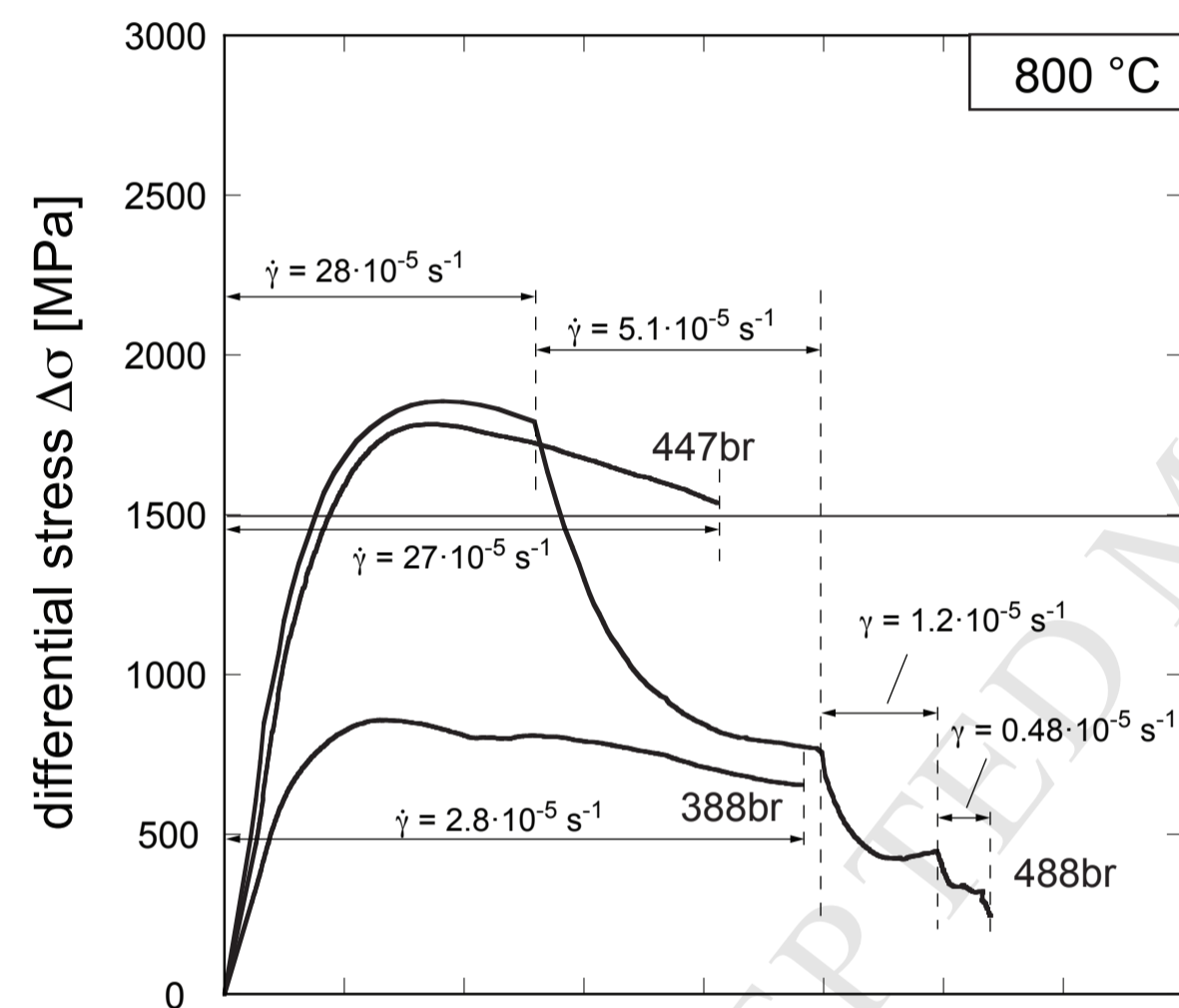
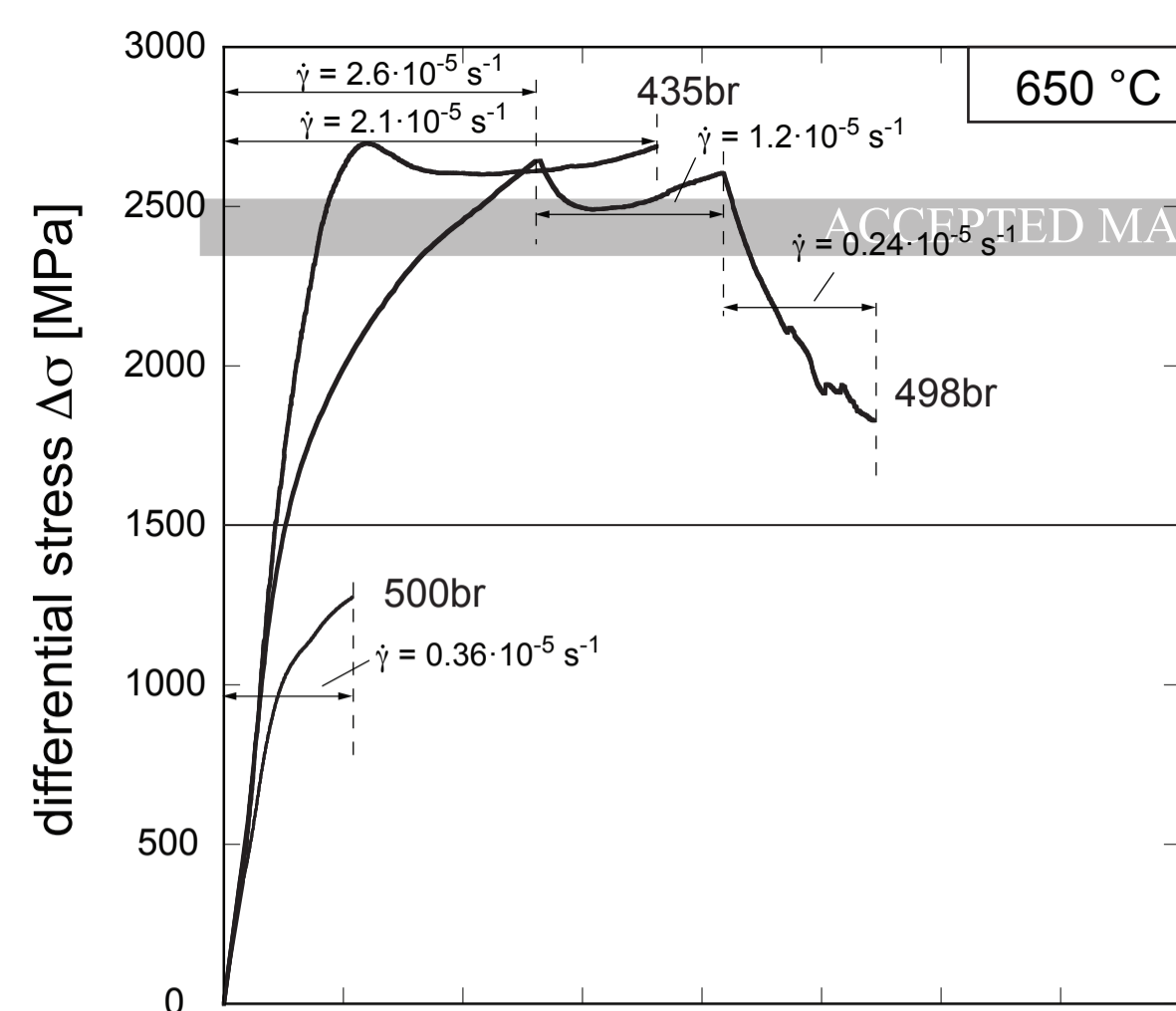
(c)

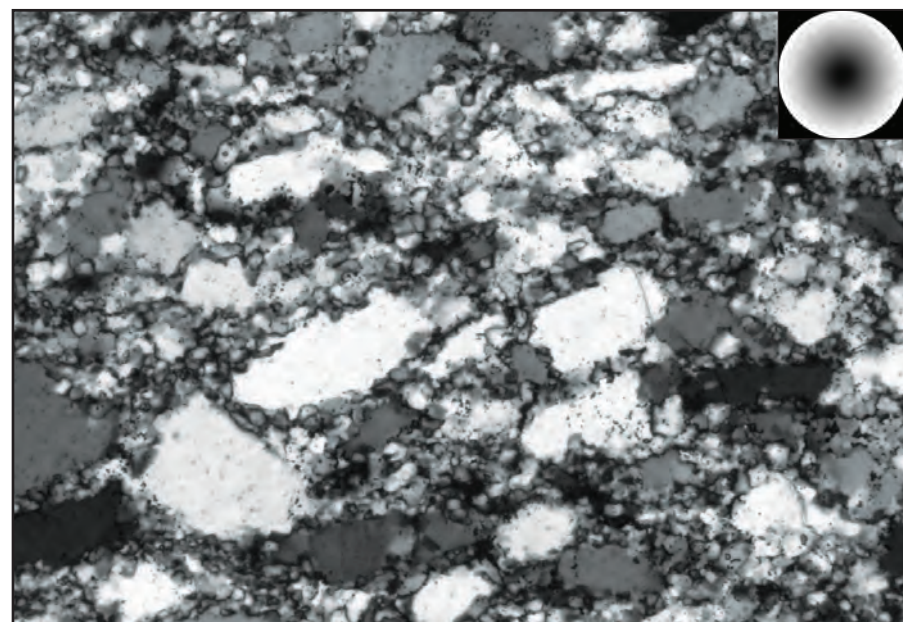






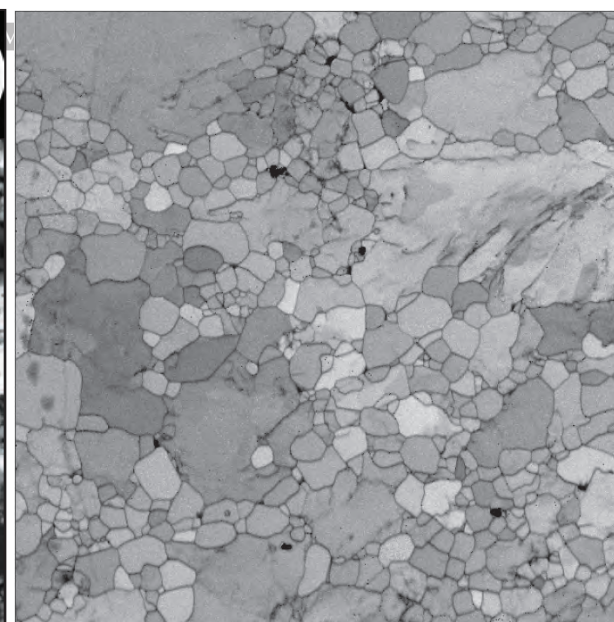






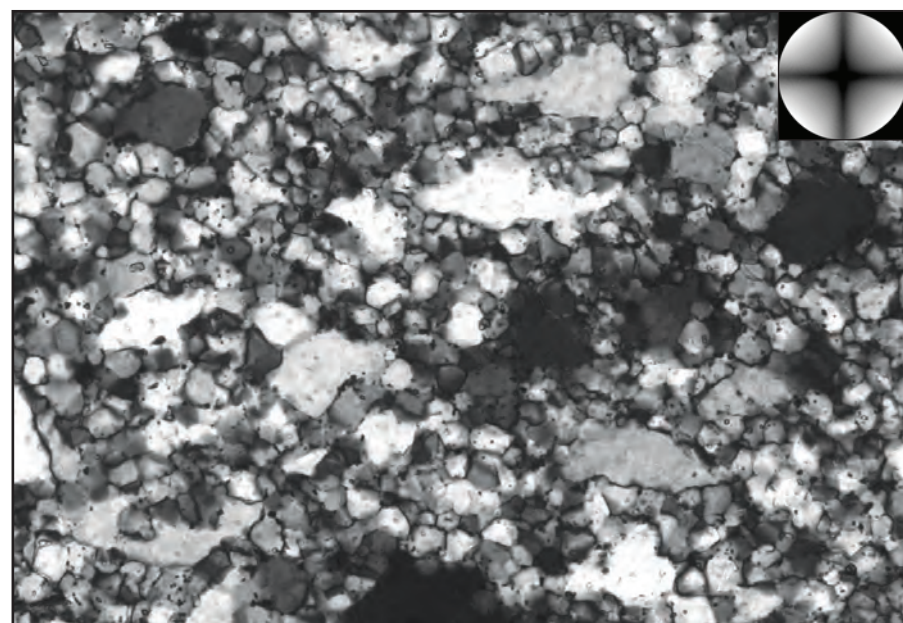
(a) 487br - 800°C

50 μm



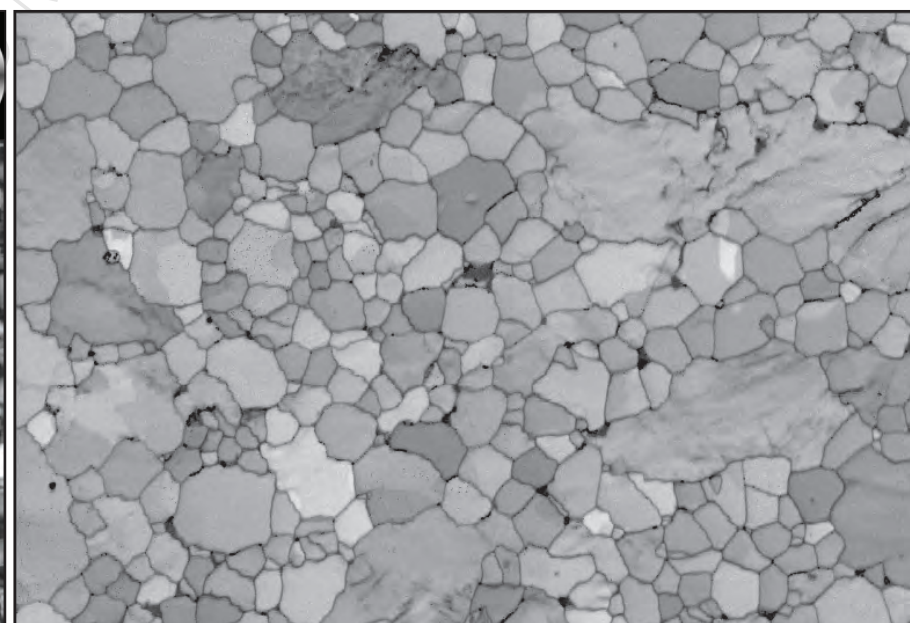
(b) 487br

25 μm



(c) 417br - 1000°C

50 μm



(d) 417br

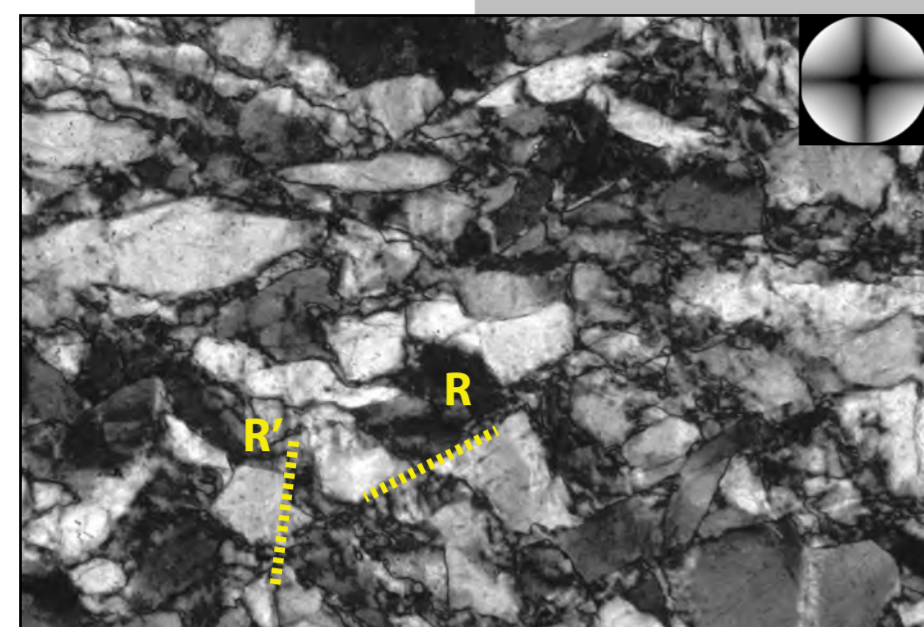
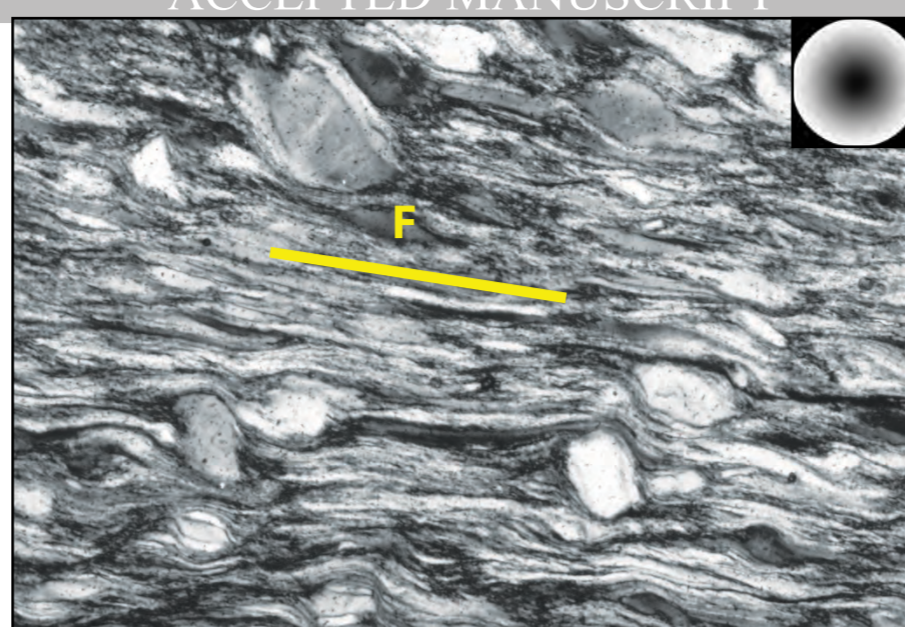
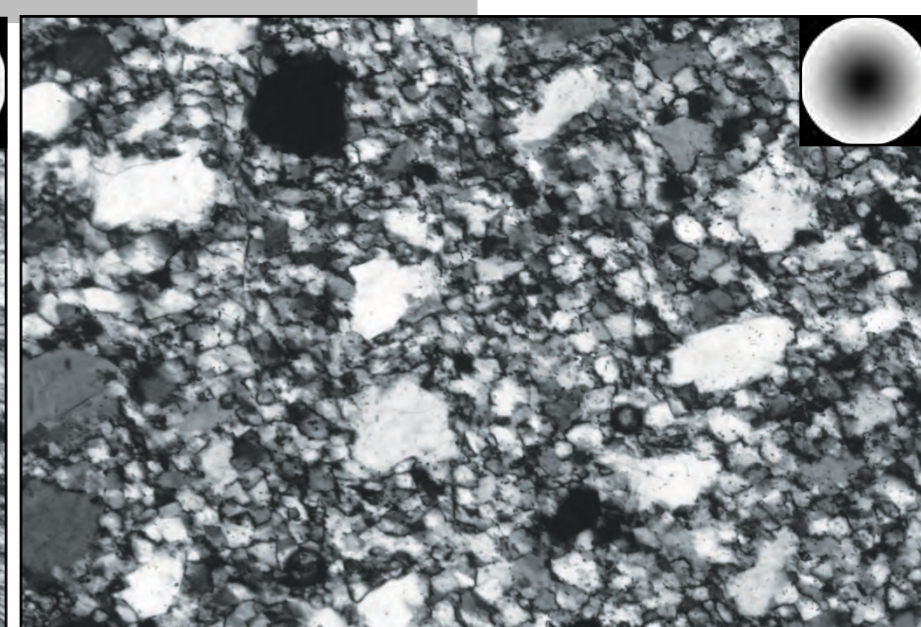
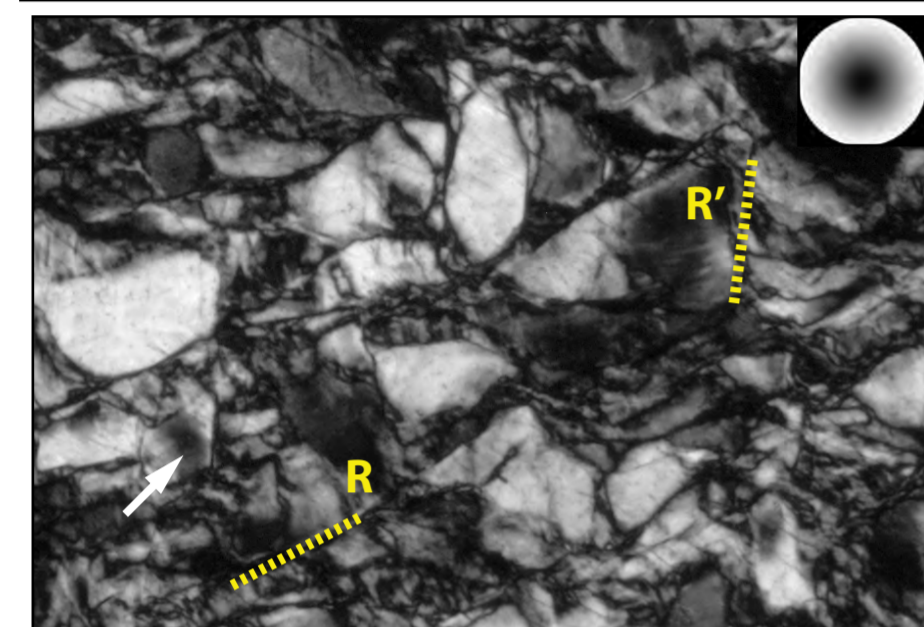
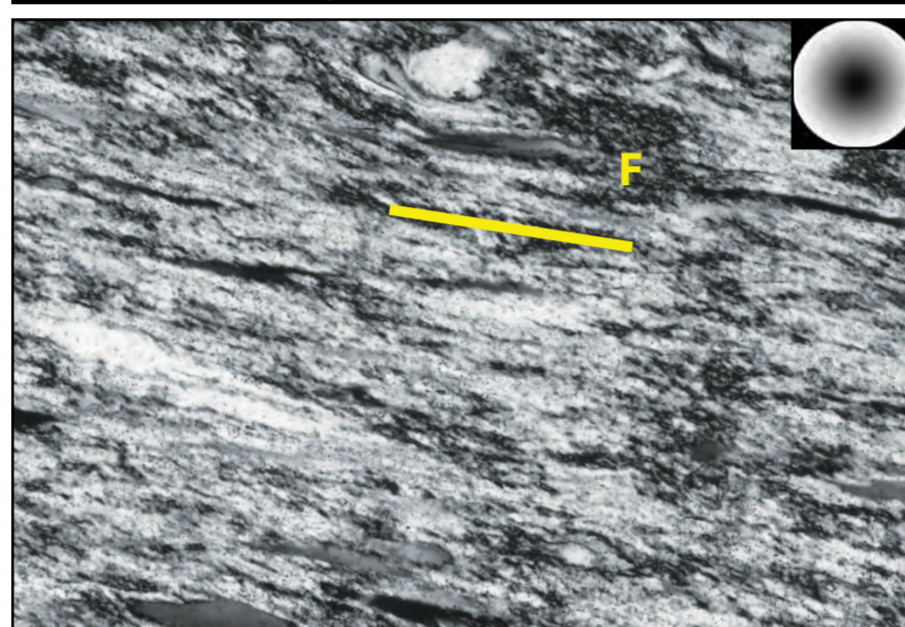
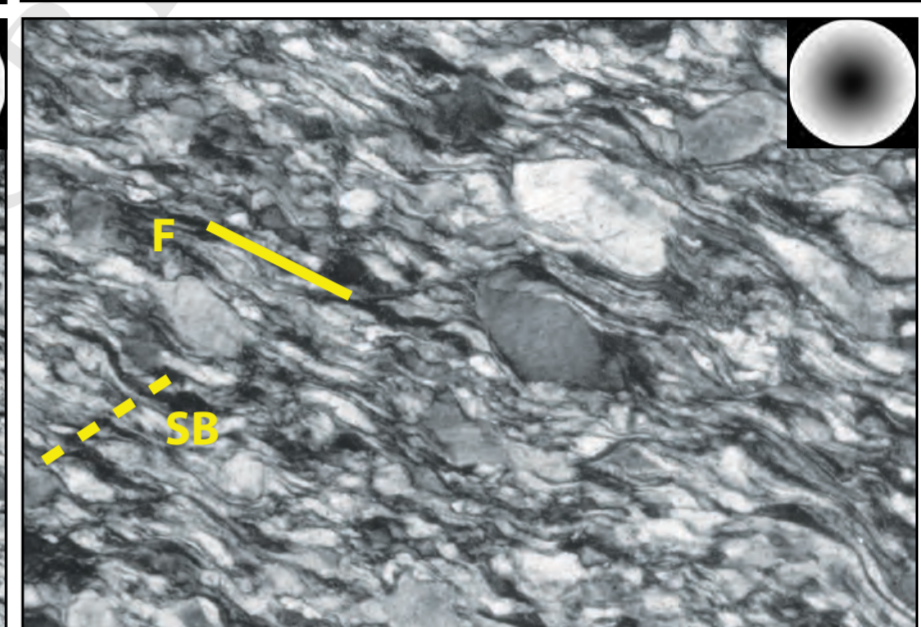
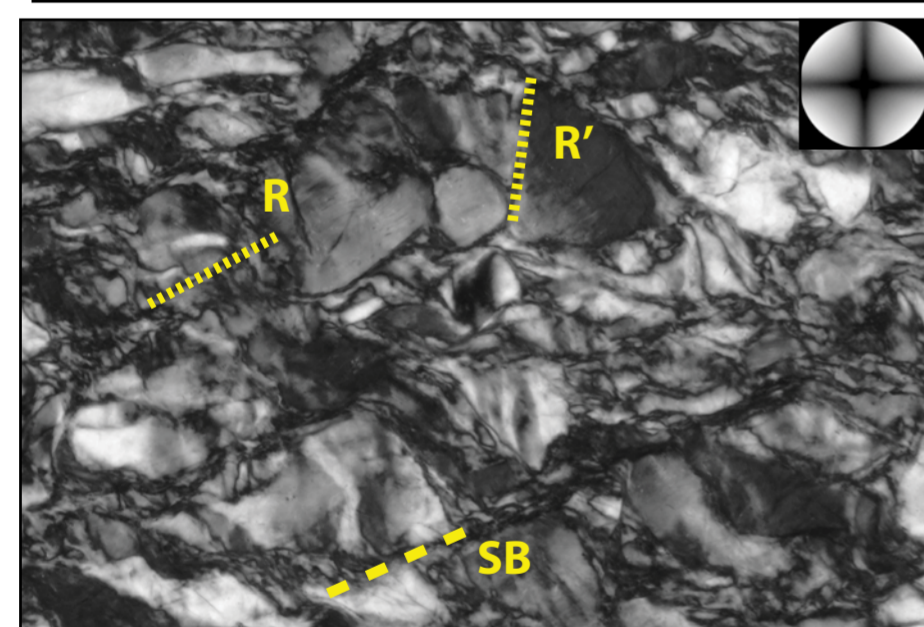
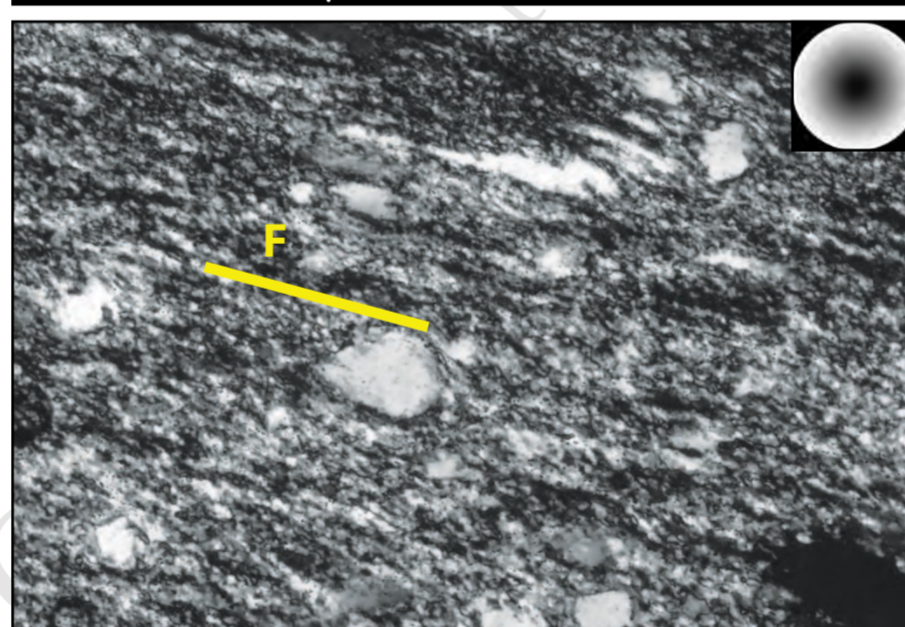
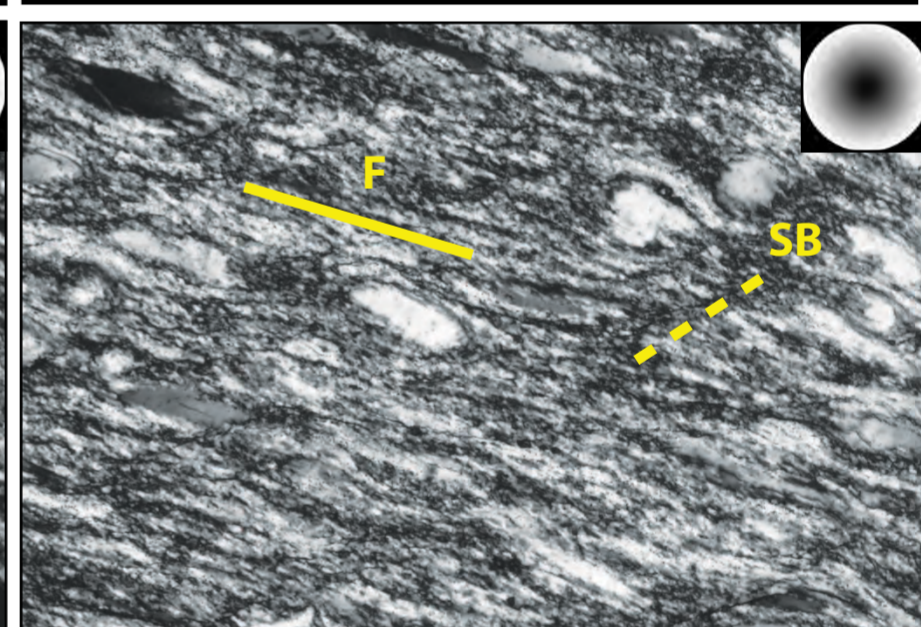
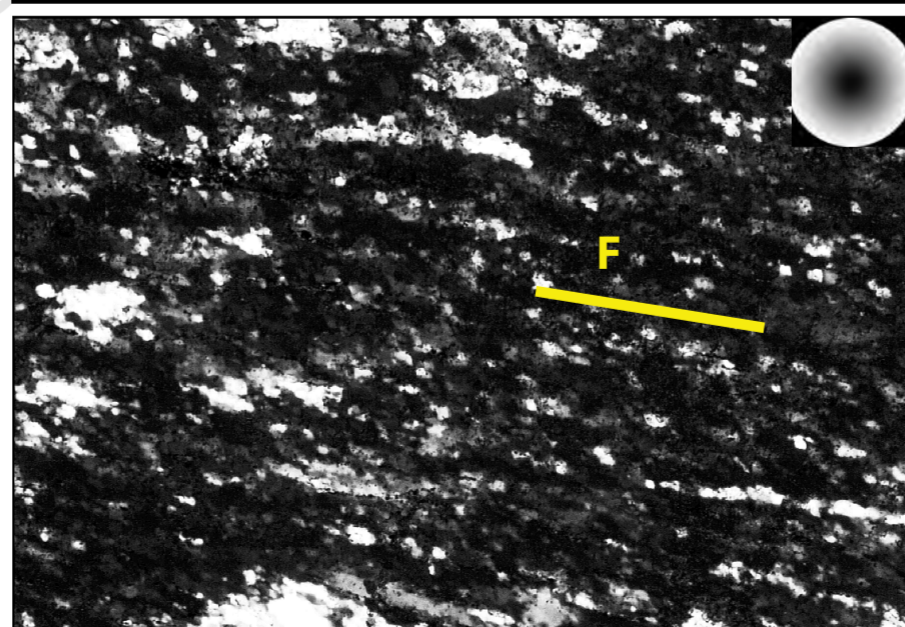
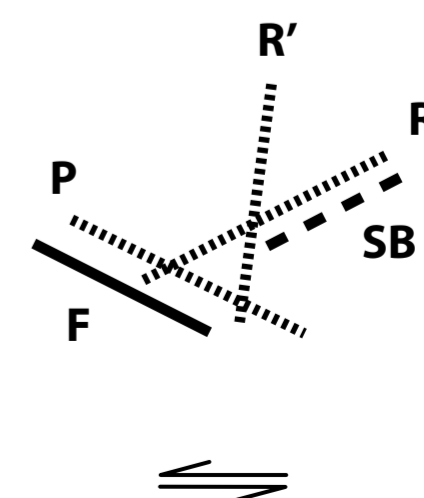
25 μm

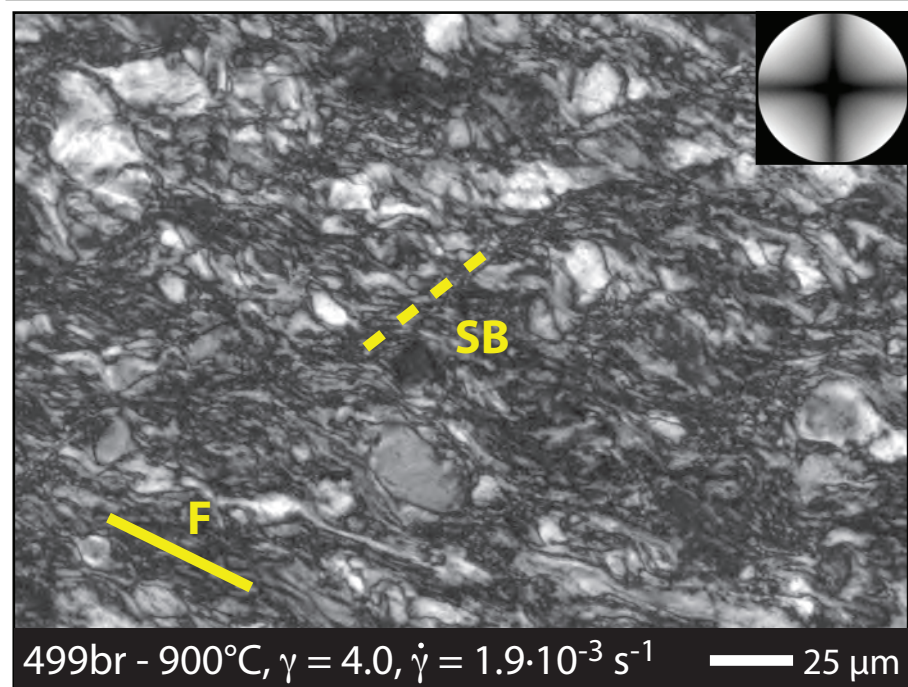
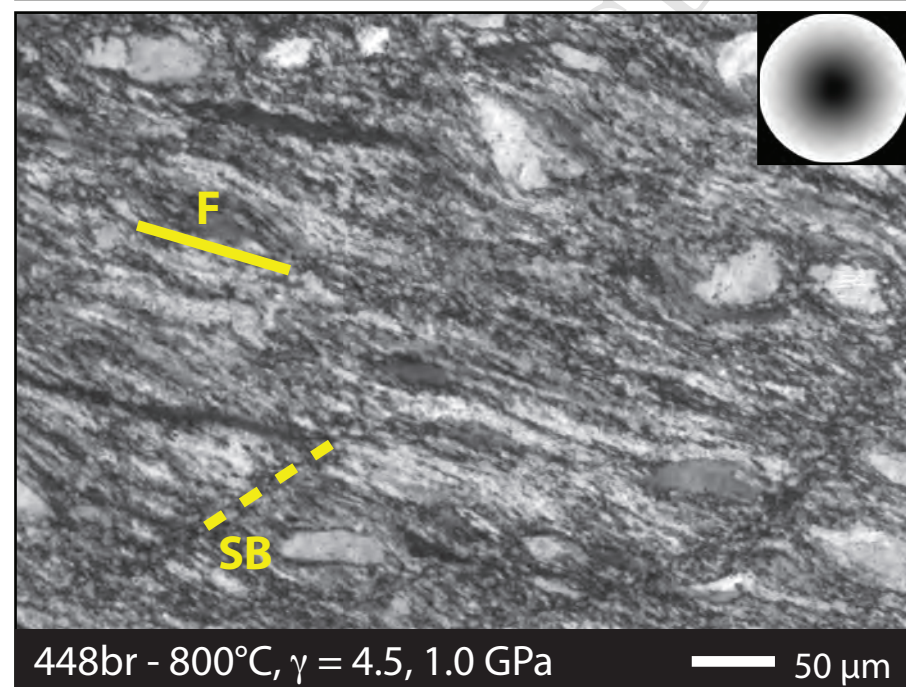
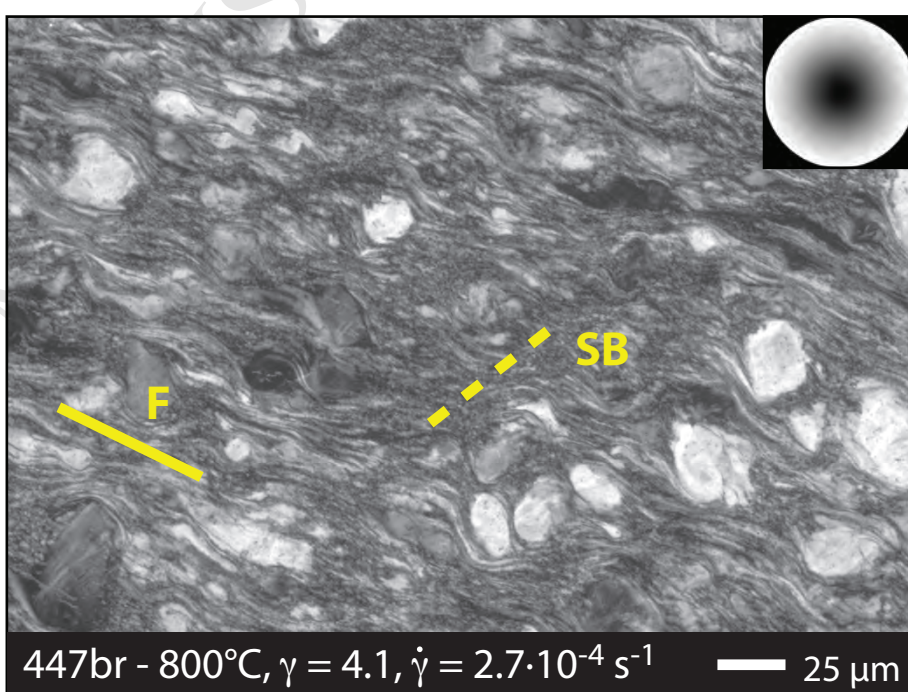
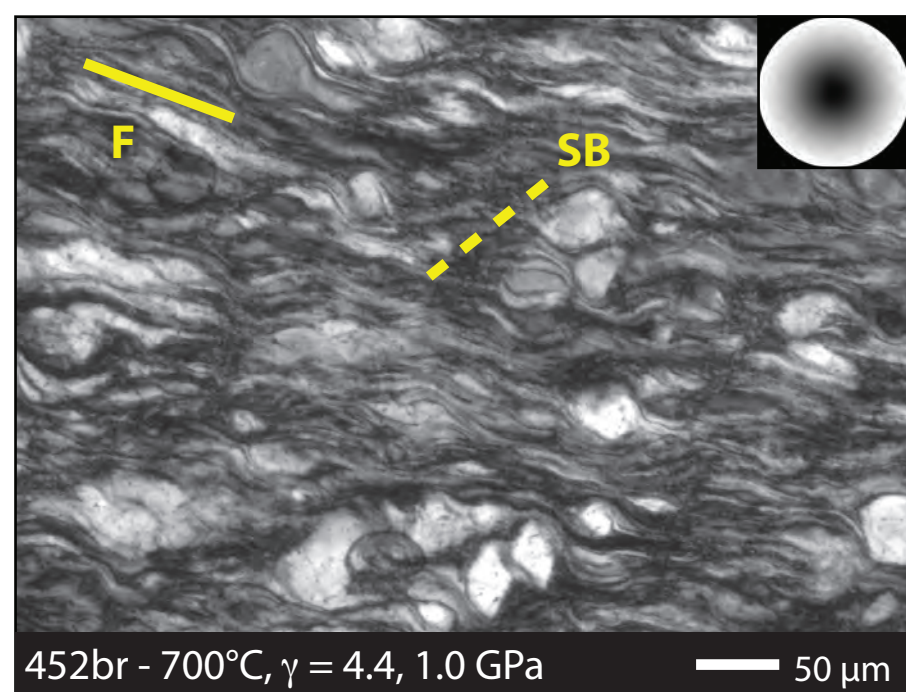
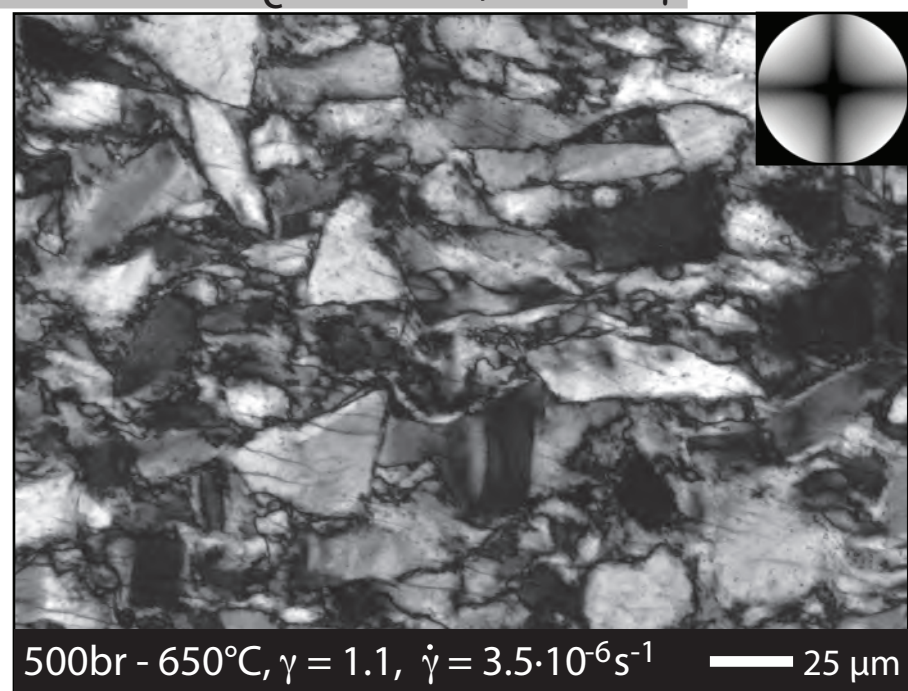
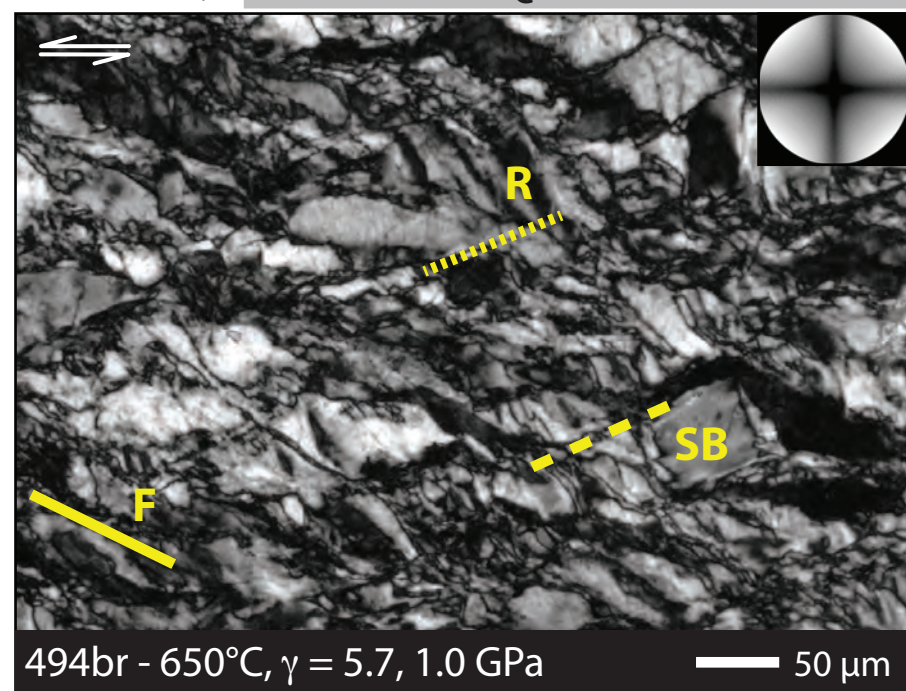
crushed

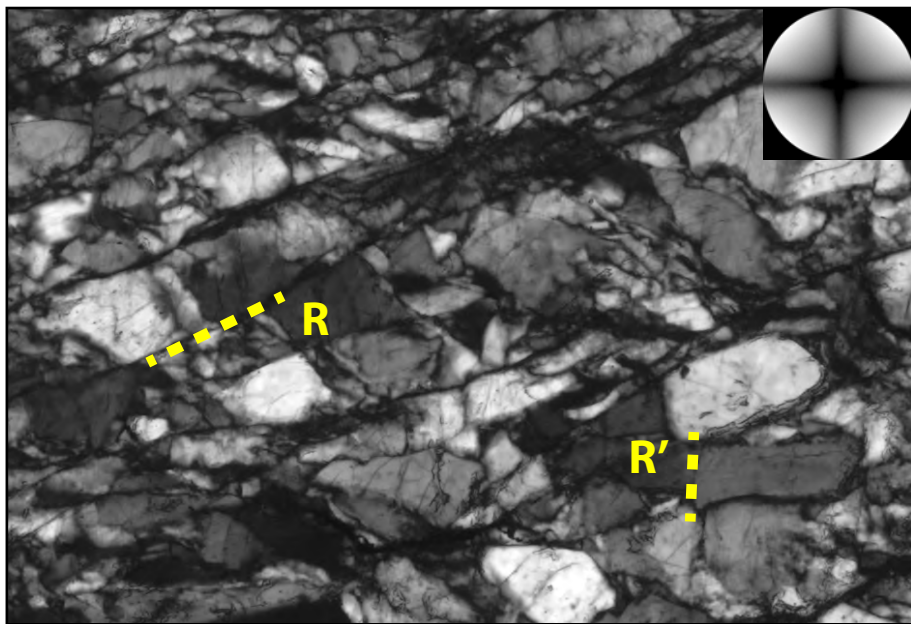
crushed

hot pressed

ACCEPTED MANUSCRIPT

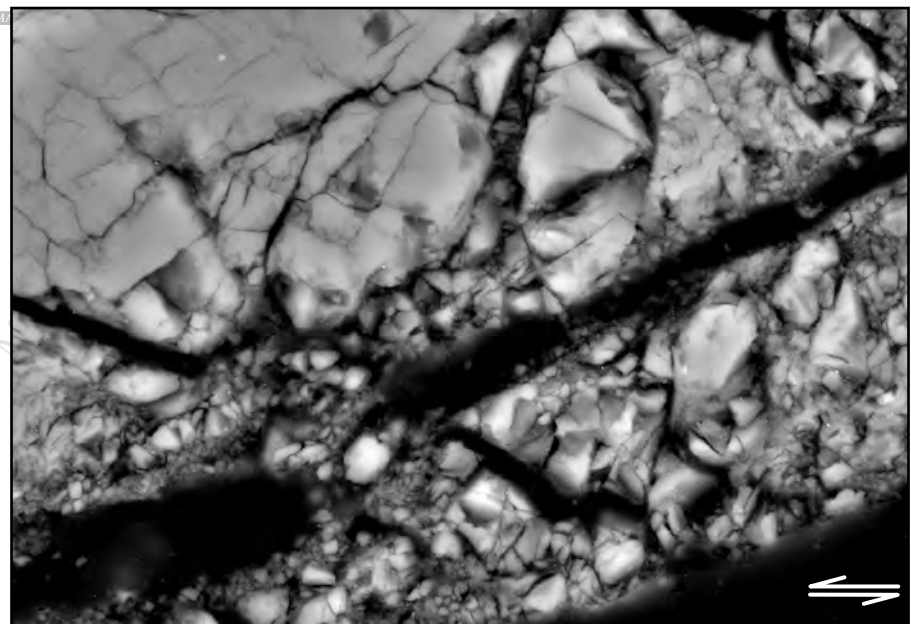
450br - 500°C, $\gamma = 3.2$ 50 μm 383br - 700°C, $\gamma = 4.9$ 50 μm 415br - 600°C, $\gamma = 3.0$ 50 μm 479br - 600°C, $\gamma = 3.9$ 50 μm 388br - 800°C, $\gamma = 4.8$ 50 μm 493br - 700°C, $\gamma = 4.9$ 50 μm 435br - 650°C, $\gamma = 3.6$ 50 μm 412br - 900°C, $\gamma = 2.9$ 50 μm 419br - 800°C, $\gamma = 4.2$ 50 μm 337br - 1000°C, $\gamma = 3.2$ 50 μm 





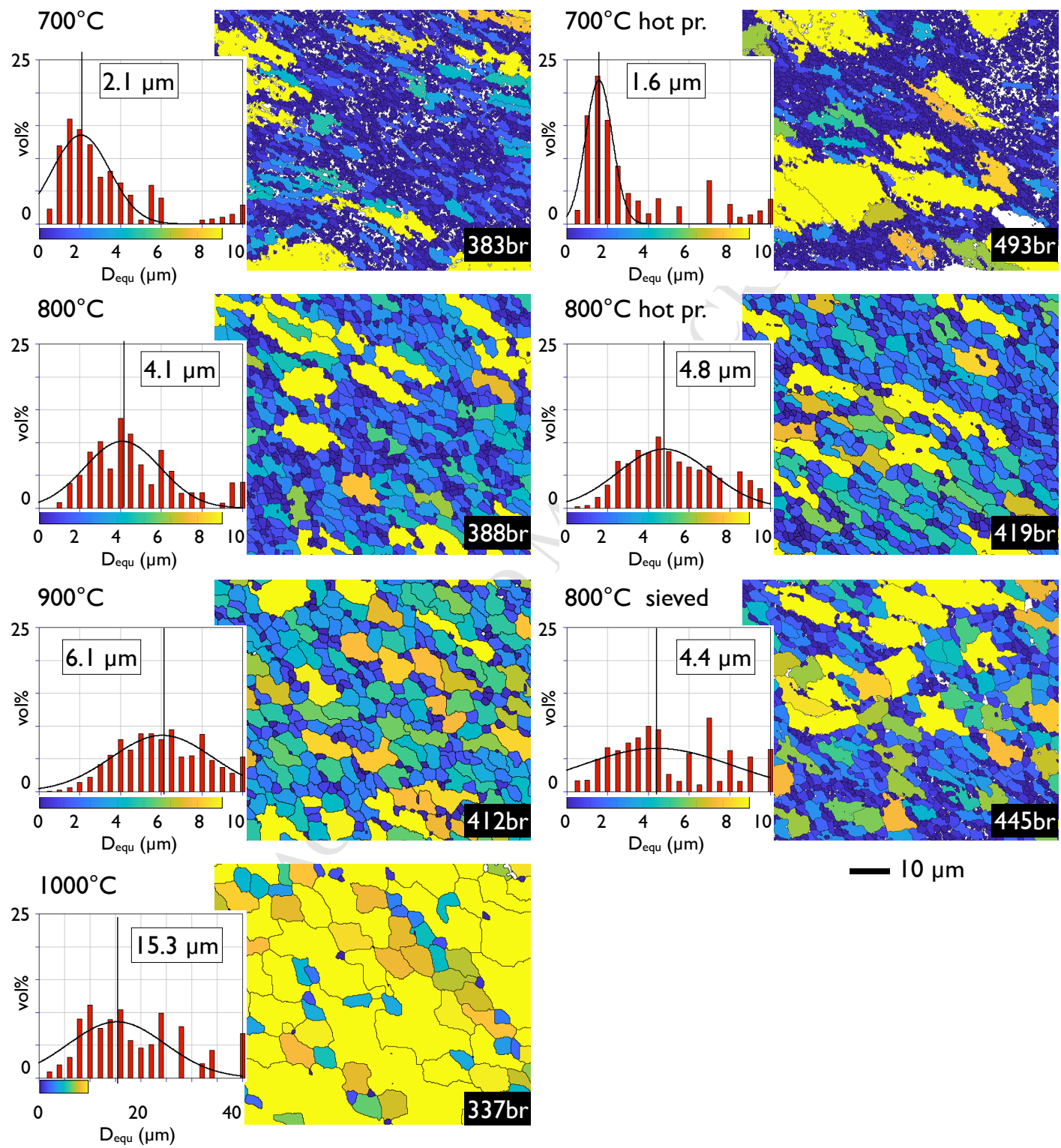
(a) 800°C , $\gamma = 3.2$

— 50 μm



(b) 800°C , $\gamma = 3.2$

— 5 μm



Highlights:

- (1) New large data set defines brittle to viscous transition in quartz
- (2) Low stress exponent of $n = 1.9 + 0.6$ between 800C and 1000C for viscous deformation
- (3) Viscous deformation by combination of dislocation and diffusion (solution precipitation) creep
- (4) Simultaneous diffusion and dislocation creep partition into different grain sizes, shown by CPO
- (5) Goetze criterion is confirmed as upper stress limit of viscous deformation